

Orbital origin of galvanomagnetic effect in Dirac and Weyl electron systems

Akiyoshi YAMADA

The University of Electro-Communications

Department of Engineering Science

A Dissertation submitted for
Doctor of Philosophy in Science

March 2022

Orbital origin of galvanomagnetic effect in Dirac and Weyl electron systems

Advisor: Associate Professor Yuki Fuseya

Secondary advisor: Associate Professor Takahiro Muranaka

Supervisory committee:

Associate Professor Yuki Fuseya

Associate Professor Takahiro Muranaka

Associate Professor Yasushi Ohfuti

Associate Professor Kazuyuki Matsubayashi

Associate Professor Masashi Tokunaga

©Copyright 2022

by

Akiyoshi Yamada

概要

固体中の電気伝導は、フェルミエネルギー近傍の電子によって担われている。特に、電子の有効質量は波数空間上におけるエネルギーの等値面（フェルミ面）の形状に依存しており、キャリア易動度の大きさや異方性を決定している。磁場が存在する場合、ボルツマン輸送に基づく半古典論的な観点から、有効質量は磁気抵抗効果やホール効果などの電流磁気効果における磁場依存性の係数として現れることが知られている。これにより、電流磁気効果はキャリアの易動度の特定に用いられてきたが、近年では Dirac・Weyl 電子系におけるトポロジカルに非自明な性質を観測する手段として注目が集まっている。

Dirac・Weyl 電子系は、波数空間に非自明な位相構造を持ち、Weyl 半金属では強磁場領域において特定のカイラリティを持つキャリアの励起（カイラル異常）が予言されている。電場と平行な磁場により抵抗率が低下する「負の縦磁気抵抗」や、ホール抵抗率が面内磁場の角度に依存する「プレーナーホール効果（PHE）」が、電子の非自明な性質を反映すると考えられており、Dirac・Weyl 型の分散が確かめられている複数の物質について、実際に観測されている。これらの効果が特に注目されている背景には、簡素な有効質量を仮定した従来の半古典論によって振る舞いを説明することが難しいという事実がある。

一方で、従来の半古典論では本来考慮されるべき物理的要請を反映していない場合がある。例えば、Dirac 電子系は一般に小さい有効質量を持つことにより、低磁場でもランダウ量子化を無視することはできない。また、近年フェルミ面の局所的構造が磁気抵抗の振る舞いを大幅に変調することが明らかになっており、異方性かつ複雑なフェルミ面をもつ Weyl 半金属においては、この効果を精緻に考慮する必要がある。本論文では、Dirac・Weyl 電子系に対し、ランダウ量子化またはフェルミ面の詳細構造を取り入れた半古典論により電流磁気効果の計算を行った。

我々はまず、Dirac 電子系半金属であるビスマスに注目した。ビスマス単結晶はこれまでに、10 T を超える磁場領域において「横磁気抵抗の異方性消失」や「PHE の周期性変化」が観測されており、その起源の解明が待たれていた。これに対して、我々は磁気抵抗の計算に際し、精緻に決定されたキャリアのランダウ準位からキャリア密度の磁場依存性を見積ることにより、定性的に実験と一致する結果をえた。さらに、Dirac 電子を有する半金属において、量子極限における横磁気抵抗の異方性消失という一般的な性質を見出すことができた。また、量子極限におけるキャリア密度の磁場依存性は、イオン化不純物による電荷の不均衡を緩和する役割を持つことが分かった。

次に、Weyl 電子系においてフェルミ面の局所構造を取り入れた磁気抵抗の計算を行った。Weyl 電子系はバンド間効果によって本質的に異方性を有しており、フェルミ面の構造も極めて異方的となる。今回、異方性のパラメータを変えながら磁気抵抗を計算したところ、リフシッツ転移後に磁気抵抗が負になるという振る舞いが見られた。Weyl 電子系は Weyl 点と呼ばれるエネルギーの縮退点を持ち、これらが有効質量の特異点となる。伝導度を磁場の 2 次まで展開（Jones-Zener 展開）したところ、縦磁気抵抗が有効質量の非対角成分に起源を持ち、この成分が Weyl 点付近で大きな負の値を取ることで抵抗率が負に転ずることがわかった。また、横磁気抵抗はフェルミ面上のガウス曲率に起因する成分とホール伝導度に起因する成分に分けられ、後者が支配的となることで負の横磁気抵抗が発現することがわかった。また、PHE の振幅の温度依存性を計算したところ、温度エネルギーがフェルミエネルギーと同程度となる領域で、谷やピークのような非単調性が現れることがわかった。このことは、PHE の温度依存性が Weyl 点のエネルギーを反映するという新しい視点を提供するものである。

Abstract

Recently, the galvanomagnetic effect is used for exploring non-trivial phenomena in topological materials including Weyl and Dirac electron systems after the observability of chiral anomaly and nontrivial Berry curvature was proposed. In these scenarios, the negative longitudinal magnetoresistance (MR) and planar Hall effect (PHE) with the period π arise from these anomalies. A mount of experiments followed these theoretical suggestions, and some materials exhibited such exotic galvanomagnetic phenomena. Although these quantum phenomena have been intensively examined, some semiclassical aspects in these materials are still to be discussed. First, Dirac and Weyl materials have generally small effective mass and modulation in carrier concentration due to the Landau quantization is not negligible even with a low field. Moreover, the Fermi surfaces in real topological materials are difficult to approximate with simple spheres or ellipsoids because the effective mass on the surface differs from point to point. In this thesis, we demonstrated the galvanomagnetic effect in Dirac and Weyl electron system based on the semiclassical theory with considering the Landau quantization and fine structure of Fermi surface.

First, we demonstrated MR and PHE in a Dirac electron system: bismuth. We applied the accurately calculated Landau levels in the carrier to the MR calculation. The cyclotron energy in bismuth becomes comparable with the Fermi energy even with a few Tesla of field. At such a field range, we found that the observed transverse MR and PHE in bismuth can be explained by the field-dependent carrier density. We also pointed a general characteristic in semimetals with Dirac electron: monotonic increment in carrier concentration and consequential vanishing of anisotropy in transverse MR.

We also discussed the case of Weyl electron by considering the fine structure of the Fermi surface. From a semiclassical point of view, the Weyl points in the Brillouin zone are regarded as singularities of effective mass. We found that the negative longitudinal MR can arise from the large and negative off-diagonal components of effective mass tensor near the singularities. Our theory also pointed that the transverse MR is contributed from two factors: Gaussian curvature on the Fermi surface and Hall conductivity. The transverse MR can be negative when the Hall conductivity dominates. We also found that the temperature dependence of PHE amplitude reflects the energy of Weyl points.

Contents

1	Introduction	3
2	Magnetotransport of charged carriers in solids	9
2.1	Boltzmann equation	9
2.1.1	Extended Mackey-Sybert model	10
2.1.2	Ellipsoidal approximation	13
2.2	Quantum theory	15
3	Dirac and Weyl electron in solids	23
3.1	$k \cdot p$ theory	24
3.1.1	The core concept of $k \cdot p$ theory	26
3.1.2	Dirac electron in solids	27
3.2	Luttinger-Kohn theory	29
3.2.1	$k \cdot p$ theory in the external magnetic field	30
3.2.2	Dirac electron in the magnetic field	34
3.2.3	Landé g -factor	35
3.2.4	Inter-band effect and adiabatic phase	36
3.3	Kane model	39
3.3.1	Weyl electron system	39
4	Magnetoresistance in Bismuth	43
4.1	Magnetoconductivity	44
4.2	Landau quantization in Bismuth carrier	46
4.2.1	Dirac electron in bismuth	46

4.2.2	Extended Dirac model	48
4.2.3	Hole in bismuth	49
4.3	Transverse magnetoresistance	50
4.4	Planar Hall effect	55
4.4.1	PHE and AMR in isotropic multi-carrier metals	58
4.4.2	Isotropic semimetals	58
4.4.3	PHE in Bismuth: compensated	60
4.4.4	PHE in Bismuth thin film: uncompensated	62
4.5	TMR far beyond the quantum limit	64
4.6	Field-dependent mobility	65
5	MR in Weyl electron systems	69
5.1	Fermi surface in Weyl electron systems	71
5.2	Magnetoresistance	72
5.2.1	The origin of negative MR	72
5.2.2	Off-diagonal effective mass	74
5.3	Planar Hall effect	77
5.3.1	Temperature dependence of PHE	78
6	Summary	85
A	PHE with spherical and ellipsoidal Fermi surfaces	87
A.1	PHE in isotropic two-carrier metals	87
A.2	Multiple ellipsoidal Fermi surfaces	88
A.3	n-valley systems	89
B	PHE in a system isotropic in x-y plane	93
	Acknowledgements	95
	Bibliography	104

Chapter 1

Introduction

Galvanomagnetic effect in condensed matter has been studied from the oldest years in solid-state physics. From the first discovery of the large magnetoresistance in pure bismuth by Kapitza in 1928 [1], a large amount of experimental and theoretical effort has been made for understanding the underlying mechanism in magneto-transport phenomena in materials. While the condition is simple, *i.e.* the electric transport in the presence of a magnetic field, the combination of electric and magnetic fields makes the situation quite complex and yields unexpected physics. For a long time, the magneto-transport phenomena have pioneered the frontier of solid-state physics. One example is the discovery of oscillatory magnetoresistance called *Shubnikov-de Haas effect* [2]. We can investigate the structure of the energy isosurface in the Brillouin zone (*Fermi surface*) by observing the angular dependence of this oscillation [3–5]. Because the fundamental of semiclassical transport based on Boltzmann’s theory is governed by the carriers near the Fermi energy, the information of the Fermi surface is inevitably essential for comprehending the carrier transport in solids. Nowadays, the study on the structure of the Fermi surface has been combined with the research of topological [6–8], organic [3–5], or superconducting [9, 10] materials and created one research field called *Fermiology*.

In the aspect of device applications, materials with a large magnetic response are promising for sensitive detectors of the magnetic field [11, 12]. High mobility and charge compensation in carriers are the general courses of large magnetoresistance

(MR) [13]. Recently, semimetals with special types of carriers: Dirac and Weyl electron, are attracting interest because of the light effective mass and resulting in large mobility [7, 14, 15]. These electrons are represented by the relativistic Hamiltonian with massive or mass-less particles. They typically have linear energy dispersion and some singularities called *Dirac cone* in the Brillouin zone.

Moreover, the expectations are running high for the topological aspects in Dirac and Weyl materials. Special structure of adiabatic parameter space underlies the physics of these materials [16]. Some quantum-mechanical origins of MR correlated with the topology have been repeatedly reported [17–23] and the interest in magneto-transport phenomena was renewed. Although phases in the wave function are implicit in free particles, the non-trivial structure of the parametric space accumulates this phase like the external magnetic field. This virtual magnetic field is called *Berry curvature* [24]. The Dirac cones have a side as the singularities of this curvature. In the presence of this curvature, the external magnetic field yields extraordinary magneto-transport phenomena. In Weyl electron systems with a twin of Dirac cone, the magnetic field parallel to the electric field causes excitation of a carrier with specific chirality (chiral anomaly) at high fields [17]. It is theoretically expected that such an anomaly or the Berry curvature yields negative longitudinal magnetoresistance [18–20, 23] and angle-dependent planar Hall effect (PHE) [21, 22]. Moreover, the Berry curvature is correlated with the electron scattering in crystals and the non-trivial curvature suppresses the amplitude of backscattering, and the lifetime of electron transport is elongated consequently [25]. A large number of experiments in the real materials with Dirac- and Weyl-type carriers have followed the theoretical suggestion [26–35]. Recently, these exotic galvanomagnetic effects are widely regarded as unique characteristics of topological materials.

Through the recent evolution of MR studies, many kinds of origins have been discovered both in the classical, semiclassical, and quantum framework. As the consequence, conflicts sometimes occur between different origins. For example, the semiclassical origin of PHE was experimentally implied in the Dirac electron systems in recent years [36–39]. Although negative longitudinal MR is also thought to be evidence of quantum anomaly, it is not a trivial question whether this phenomenon cannot be explained in the semiclassical framework. Moreover, we have still several

critical mysteries in the magneto-transport phenomena. There are roughly two problems: quantitative and qualitative problems. First, there is a lot of materials that exhibit sizable magnetoresistance [40–42] and other galvanomagnetic response [8, 43] which are remarkably larger than the theoretical estimations. Second, some materials show exotic behavior in magnetoresistance which conventional theory cannot give even a qualitative explanation. For example, bismuth, which is a typical Dirac electron system, exhibits changes in angular dependence of magnetoresistance [40, 44–46] even though this material does not have any spontaneous magnetic moment. Furthermore, there are the most long-standing problems: *Linear Magnetoresistance*. According to conventional theories, the magnetoresistance in metals exhibits parabolic or saturating behavior against the magnetic field. However, not a few materials indicate non-saturating and linear dependence on the field [47–49]. Although several phenomenological explanations or theoretical exposition in specific systems have been made [18, 50–52], a comprehensive understanding of this phenomenon has not been obtained yet.

Sometimes we face a fundamental question: how can we attribute the observed phenomena to their right origin? Even when we do not have explanations in conventional semiclassical theory, we cannot immediately affirm that observed MR has a quantum origin. It is because we do not know the limit of the semiclassical theory. We just know predictions from simplified models. In order to give a progress in the understanding of the origins, we must move on to the intermediate region of conventional semiclassical and quantum theories.

As mentioned above, there are several conflicts between observations and conventional semiclassical theories based on the Boltzmann equation. The semiclassical picture of a charged carrier accelerated by Lorentz force in solid is intuitive and indeed useful for analyzing the magneto-transport in simple metals at low fields. Carrier mobility and concentration have been obtained by analyzing magnetoresistance and Hall resistance in this framework [53]. On the other hand, the simple semiclassical theory fails to explain two typical cases: quantum mechanical phenomena and carrier conduction with complex energy dispersion.

The cause of the first difficulty is apparent. Carriers in solids naïvely has discrete energy levels due to the Landau quantization in the magnetic field. When the mag-

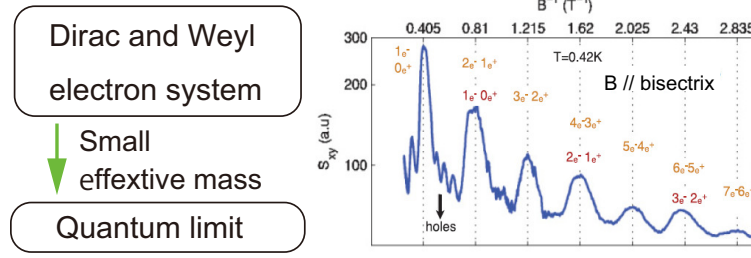


Figure 1.1: (left) Mass properties in the magneto-transport in Dirac and Weyl electron systems. (right) Quantum oscillation in the Nernst voltage in bismuth. [54]

netic field is such strong that the cyclotron energy is as large as the Fermi energy, the effect of Landau quantization cannot be neglected. The linear dispersion in Dirac and Weyl electrons generally makes the effective mass drastically small. Consequently, the cyclotron energy becomes comparable to the Fermi energy with moderately low fields (Fig. 1.1). Real Dirac or Weyl materials indicate clear quantum oscillation and the crossover to the *quantum limit* at low fields [54, 55]. *Quantum limit* means the state where the cyclotron energy exceeds the Fermi energy. The classical theory cannot simulate the quantum oscillation therefore it is powerless to the phenomena beyond the quantum limit.

In this thesis, we discuss the magnetoresistance in the Dirac electron system by considering the Landau quantization. Dirac electron exhibits special field dependence of Landau levels due to the strong band interaction through the strong spin-orbit coupling. Especially, the non-trivial characteristic courses the degeneration of total angular momentum resulting in stable lowest Landau level [56, 57]. We found that the stability causes a linear increment of carrier concentration in the quantum limit region. For electrons with anisotropic mass, this carrier density also depends on the direction of the field. We also found that this anisotropic carrier density is negatively correlated with the carrier mobility in the magnetoresistance, and we concluded that the semimetals with Dirac electrons generally exhibit the vanishing of anisotropy in transverse magnetoresistance. These characteristics successfully explain the angular dependence of transverse MR in bismuth around the quantum limit. We also calculated the angular dependence of PHE in bismuth. Surprisingly,

the observed angular dependence can be explained successfully by multiple carrier transport without assuming topological effects such as the chiral anomaly and Berry curvature. We pointed that the field-dependent carrier concentration in a specific electron system can be a factor to change the characteristics of the galvanomagnetic effect qualitatively.

The cause of another problem is not so fundamental but has been overlooked for a long time. The point is that the fine structure of the Fermi surface determines the qualitative and quantitative characteristics of magnetoresistance. In general metals, semiconductors, and semimetals, the Fermi surface is not a single sphere. Good metals (with large Fermi surface) including Cu, Li and Ca have almost spherical Fermi surface. However, some of the surfaces have several "holes" at the zone boundary due to the large Fermi energy. This little deviation from sphere is not negligible in magneto-transport. Some electron trajectories on the Fermi surface cannot be closed when the magnetic field is applied in specific directions, which leads to the enhancement of magnetoresistance and yields large anisotropy (Fig. 1.2a,b) [13, 58]. Fermi surfaces in some semiconductors are well approximated with multiple ellipsoids [59, 60]. This anisotropic structure yields off-diagonal components of the *effective mass tensors*, which result in the coupling between electron current and the magnetic field. Longitudinal magnetoresistance can arise from this coupling [61, 62]. In some multiple ellipsoidal electron systems, the longitudinal magnetoresistance is quite high and exceeds the transverse magnetoresistance [47, 62]. Furthermore, a cubic description for the Fermi surface successfully explained the behavior of magnetoresistance in a semiconductor SrTiO_3 with a dilute carrier [63, 64]. After all, we cannot neglect the effect from the local structure on the Fermi surfaces, wave-number-dependent effective mass in other words, in simulating magneto-transport in solids (Fig. 1.2). Especially, the Weyl electron, which we are interested in, is a typically anisotropic system with complex Fermi surface in low energy regions. Moreover, the structure of the Fermi surface is variable depending on the carrier concentration and intensity of band interaction. The surface becomes far from a sphere in the strong-interaction region.

In this thesis, we report the extended semiclassical approach to the Weyl electron systems based on the fine structure of the Fermi surface. From more than a half-

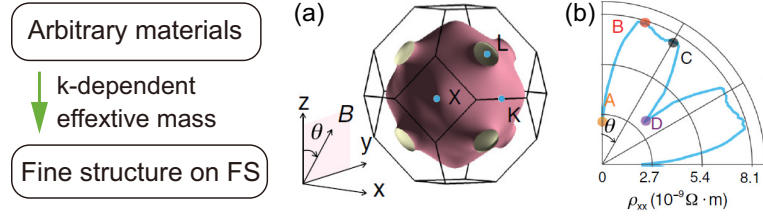


Figure 1.2: Mass property of mass in general materials. (a) Fermi surface and (b) calculated transverse MR in copper [58]

century ago, a method for calculating magnetoresistance in arbitrary Fermi surface is known and widely used [41,58,65]. This method attributes the MR to the periodic orbital motion on the wave space. Another method for calculating MR was built recently [63]. This new method is also applicable to arbitrary dispersion. Moreover, we can clearly find the origins of magnetoresistance in the terms of velocity and effective mass on the Fermi surface. We calculated the MR and PHE in Weyl electron without assuming Berry curvature or other topological effects. We find that the longitudinal and transverse magnetoresistance can turn negative due to the negative off-diagonal effective mass. The effective mass is singular at the Weyl point and the semiclassical MR behavior also reflects the nature of the Weyl electron. We also investigate the temperature dependence of PHE amplitude and show non-monotonic characteristics. We point that the positions of dip and peak structures are correlated with the energy of Weyl points measured from the Fermi energy. From this result, we also show that one can experimentally determine the energy of Weyl points by observing the temperature dependence of PHE amplitude.

This thesis consists of five chapters and an appendix. In *Chapter.2*, we introduce the semiclassical method for simulating MR applicable to arbitrary dispersion. We also show that the quantum magneto-transport theory can reproduce the field-dependence in the semiclassical theory and simulate the quantum oscillation. In *Chapter.3*, we show the Dirac and Weyl Hamiltonian in solid are derived from the $k \cdot p$ theory. We also show that the $k \cdot p$ theory is a powerful tool for simulating the energy levels in the magnetic field. In *Chapter.4* and *Chapter.5*, we show the details of our subjects, the condition of our calculation, the results, and discussions.

Chapter 2

Magnetotransport of charged carriers in solids

We introduce the semiclassical theory of magneto-transport phenomena of electrons in solids. In this theory, the transport coefficients are given by solving the Boltzmann equation with proper approximations. We review some useful extensions for calculating magnetoresistance (MR) in real materials. We also derive the magneto-conductivity tensor from the fully quantum theory: Kubo formula, and show that the results agree with the semiclassical one at low fields. Moreover, the quantum theory can simulate quantum oscillation at high fields.

2.1 Boltzmann equation

In the weak field region where the Landau quantization is not remarkable, the Boltzmann equation gives a good description of the electron transport in solids (especially good metals). The equation in the magnetic field is written as follows:

$$\frac{\partial f}{\partial t} - \frac{e}{\hbar} (\mathbf{E} + \mathbf{v} \times \mathbf{B}) \cdot \nabla_{\mathbf{k}} f + \mathbf{v} \cdot \nabla_{\mathbf{r}} f = \left(\frac{\partial f}{\partial t} \right)_{\text{collision}}, \quad (2.1)$$

where f is the distribution function and the vector \mathbf{E} , \mathbf{B} , \mathbf{v} are the electric field, magnetic field, and the velocity of the electron ($e > 0$) respectively. Our purpose is to obtain the conductivity σ , which is the correlation coefficient between the electric

current density and electric field. When the magnetic field is applied, this coefficient is represented with 3×3 tensor $\hat{\sigma}$. In solving the equation, we assume the so-called relaxation time approximation written in the following condition:

$$\left(\frac{\partial f}{\partial t}\right)_{\text{collision}} = \frac{f - f_0}{\tau}. \quad (2.2)$$

The constant τ is the relaxation time of the electron and f_0 is the distribution function in equilibrium. In the following, we assume the static condition: $\partial f / \partial t = 0$ and uniformity of the system: $\nabla_{\mathbf{r}} f = 0$.

2.1.1 Extended Mackey-Sybert model

Simplified semiclassical model which approximates the Fermi surface with sphere or ellipsoids cannot be applied to the general material with complex Fermi surfaces. However, these types of conventional models are often used in analyzing experimental MR. These models are quite simplified and exotic behavior originating from the electron orbitals is often overlooked, or one may misunderstands the origin of observed MR. The magneto-transport phenomena in Dirac and Weyl electron systems are especially attracting interest from the quantum viewpoint. On the other hand, these systems generally have complex Fermi surfaces and the band structures cannot be described by parabolic curves. More precisely, the effective mass depends on wave number in the Brillouin zone, which possibly yields non-trivial MR from the viewpoint of semiclassical transport. In order to simulate the MR accurately in such special systems, it is necessary to consider the fine structures of the Fermi surfaces.

From early years, a method by Shockley and Chambers for calculating MR in arbitrary dispersion is known [65,66] and applied to various materials [41,58,67,68]. This method simulates MR by calculating the velocity correlation in the wave space. Recently, a new method applicable to arbitrary energy dispersion was built. This method considers the inverse effective mass on the Fermi surface given by the second derivative of energy [63]. We can attribute the simulated MR to the local structure with the aid of this method. Magnetoconductivity is calculated with the following

formula:

$$\begin{aligned}\sigma_{\lambda,\mu} &= -e \left\langle v_\lambda \left\{ \mathbf{v} \cdot \left[\frac{1}{e\tau} - \hat{B} \cdot \hat{\alpha}_{\mathbf{k}} \right]^{-1} \right\}_\mu \right\rangle, \\ \mathbf{v}_{\mathbf{k}} &= \nabla_{\mathbf{k}} \epsilon / \hbar, \quad (\hat{\alpha}_{\mathbf{k}})_{\lambda,\mu} = \frac{\partial^2 \epsilon}{\hbar^2 \partial k_\lambda \partial k_\mu},\end{aligned}\tag{2.3}$$

where $\langle \dots \rangle = \int d\mathbf{k} / 4\pi^3 \dots \frac{df}{d\epsilon}$ and $f(\epsilon)$ is the Fermi distribution function. \mathbf{k} denotes the wavenumber. $\hat{\alpha}_{\mathbf{k}}$ is the local inverse mass tensor, and $(\hat{B})_{ij} = -\epsilon_{ijk} B_k$ is the magnetic field tensor introduced by Mackey and Sybert [69]. This formula was derived by extending a formula by them. Here, we show the detail of derivation. We start with the Boltzmann equation with the relaxation time approximation.

$$-e(\mathbf{E} + \mathbf{v} \times \mathbf{B}) \cdot \nabla_{\mathbf{p}} f = \frac{f - f_0}{\tau}\tag{2.4}$$

General treatment of this equation is putting [70]

$$f - f_0 = -\phi(\mathbf{k}) \frac{\partial f_0}{\partial \epsilon}.\tag{2.5}$$

Following Sondheimer and Willson [71], the factor ϕ is written as,

$$\phi(\mathbf{k}) = \mathbf{G} \cdot \mathbf{v}.\tag{2.6}$$

The derivative with the momentum is written as

$$\begin{aligned}\nabla_{\mathbf{p}} f &= \nabla_{\mathbf{p}} \left(f_0 - \mathbf{G} \cdot \mathbf{v} \frac{\partial f_0}{\partial \epsilon} \right) \\ &= (\nabla_{\mathbf{p}} \epsilon) \frac{\partial f_0}{\partial \epsilon} - \nabla_{\mathbf{p}} \left(\mathbf{G} \cdot \mathbf{v} \frac{\partial f_0}{\partial \epsilon} \right) \\ &= \mathbf{v} \frac{\partial f_0}{\partial \epsilon} - ((\nabla_{\mathbf{p}} \mathbf{G}) \cdot \mathbf{v} + \mathbf{G} \cdot (\nabla_{\mathbf{p}} \mathbf{v})) \frac{\partial f_0}{\partial \epsilon} - (\mathbf{G} \cdot \mathbf{v}) \mathbf{v} \frac{\partial^2 f_0}{\partial \epsilon^2}.\end{aligned}\tag{2.7}$$

We can show that the vector $(\nabla_{\mathbf{p}}\mathbf{G}) \cdot \mathbf{v}$ is parallel with the velocity \mathbf{v} as follows:

$$\begin{aligned}
\nabla_{\mathbf{p}}\mathbf{G} \cdot \mathbf{v} &= \begin{pmatrix} \nabla_{p_x}G_x & \nabla_{p_x}G_y & \nabla_{p_x}G_z \\ \nabla_{p_y}G_x & \nabla_{p_y}G_y & \nabla_{p_y}G_z \\ \nabla_{p_z}G_x & \nabla_{p_z}G_y & \nabla_{p_z}G_z \end{pmatrix} \begin{pmatrix} v_x \\ v_y \\ v_z \end{pmatrix} \\
&= \begin{pmatrix} \nabla_{p_x}G_x v_x + \nabla_{p_x}G_y v_y + \nabla_{p_x}G_z v_z \\ \nabla_{p_y}G_x v_x + \nabla_{p_y}G_y v_y + \nabla_{p_y}G_z v_z \\ \nabla_{p_z}G_x v_x + \nabla_{p_z}G_y v_y + \nabla_{p_z}G_z v_z \end{pmatrix} \\
&= (\operatorname{div}\mathbf{G})\mathbf{v} + (\mathbf{v} \times \nabla_{\mathbf{p}}) \times \mathbf{G} \\
&= (\operatorname{div}\mathbf{G})\mathbf{v} + \left(\mathbf{v} \times \mathbf{v} \frac{\partial}{\partial \epsilon} \right) \times \mathbf{G} = (\operatorname{div}\mathbf{G})\mathbf{v}
\end{aligned}$$

Substituting it into eq.(2.4) and applying $(\mathbf{v} \times \mathbf{B}) \cdot \mathbf{v} = 0$, the second term is written as

$$e(\mathbf{E} + \mathbf{v} \times \mathbf{B}) \cdot \nabla_{\mathbf{p}}f = e\mathbf{E} \cdot \nabla_{\mathbf{p}}f - e(\mathbf{v} \times \mathbf{B})(\mathbf{G} \cdot (\nabla_{\mathbf{p}}\mathbf{v})) \frac{\partial f_0}{\partial \epsilon}. \quad (2.8)$$

Moreover, $\phi(\mathbf{k})$ is proportional to the electric field [70], and we neglect the terms higher order terms than E^2 and get

$$e\mathbf{E} \cdot \nabla_{\mathbf{p}}f \sim e\mathbf{v} \cdot \mathbf{E} \frac{\partial f_0}{\partial \epsilon}. \quad (2.9)$$

Finally, Equation 2.4 in our case is given as follows:

$$-e\mathbf{v} \cdot \mathbf{E} \frac{\partial f_0}{\partial \epsilon} + e(\mathbf{v} \times \mathbf{B})(\mathbf{G} \cdot (\nabla_{\mathbf{p}}\mathbf{v})) \frac{\partial f_0}{\partial \epsilon} - \frac{1}{\tau}(\mathbf{G} \cdot \mathbf{v}) \frac{\partial f_0}{\partial \epsilon} = 0,$$

and by replacing $\mathbf{v} \times \mathbf{B}$ and $\mathbf{G} \cdot (\nabla_{\mathbf{p}}\mathbf{v})$ with $\mathbf{v} \cdot \hat{B}$ and $\hat{\alpha} \cdot \mathbf{G}$, we get

$$-e\mathbf{v} \cdot \mathbf{E} \frac{\partial f_0}{\partial \epsilon} + e\mathbf{v} \cdot \hat{B} \cdot \hat{\alpha} \cdot \mathbf{G} \frac{\partial f_0}{\partial \epsilon} - \frac{1}{\tau}(\mathbf{G} \cdot \mathbf{v}) \frac{\partial f_0}{\partial \epsilon} = 0. \quad (2.10)$$

Eliminating $\frac{\partial f_0}{\partial \epsilon}$, we obtain

$$\mathbf{G} = \left[\hat{B} \cdot \hat{\alpha} - \frac{1}{e\tau} \right]^{-1} \mathbf{E}. \quad (2.11)$$

The electric conductivity is calculated as follows:

$$\begin{aligned}\mathbf{J} &= -\frac{2e}{(2\pi)^3} \int d^3k \mathbf{v} \left(-\mathbf{G}\mathbf{v} \frac{\partial f_0}{\partial \epsilon} \right) \\ &= \frac{2e}{(2\pi)^3} \int d^3k \mathbf{v} \left(\mathbf{v} \cdot \left[\hat{B} \cdot \hat{\alpha} - \frac{1}{e\tau} \right]^{-1} \right) \frac{\partial f_0}{\partial \epsilon} \cdot \mathbf{E}.\end{aligned}\quad (2.12)$$

Finally, a conductivity tensor is obtained.

$$\sigma_{ij} = \frac{2e}{(2\pi)^3} \int d^3k v_i \left(\mathbf{v} \cdot \left[\hat{B} \cdot \hat{\alpha} - \frac{1}{e\tau} \right]^{-1} \right)_j \frac{\partial f_0}{\partial \epsilon} \quad (2.13)$$

The resistivity tensor $\hat{\rho}$ is given by the inversion of the conductivity tensor.

$$\hat{\rho} = \hat{\sigma}^{-1} \quad (2.14)$$

2.1.2 Ellipsoidal approximation

In semiconductors or semimetals, the carriers in band edge are often approximated with a free particle with anisotropic mass. In other words, the bands are approximated with parabolic dispersion and Fermi surfaces are identified with ellipsoids as follows:

$$\epsilon(\mathbf{p}) = \frac{1}{2} \sum_i \alpha_{ii} p_i^2 = \frac{\mathbf{p} \cdot \hat{\alpha} \cdot \mathbf{p}}{2}. \quad (2.15)$$

$\hat{\alpha}$ is a constant diagonal tensor. After the momentum transformation: $\mathbf{w} = \hat{\alpha}^{1/2} \mathbf{p}$, the Fermi surface becomes spherical in w space. The derivative of \mathbf{p} can be expressed by the derivative of energy as follows:

$$\begin{aligned}d\mathbf{p} &= (\det \hat{\alpha})^{-1/2} d\mathbf{w} = (\det \hat{\alpha})^{-1/2} dS(\epsilon) d\epsilon / |\nabla_w \epsilon| \\ &= (\det \hat{\alpha})^{-1/2} dS(\epsilon) d\epsilon / w,\end{aligned}$$

where $S(\epsilon)$ is an element of the area on the spherical Fermi surface. The integration in Eq. 2.13 can be done analytically as follows:

$$\begin{aligned}\hat{\sigma} &= \frac{2e(\det\hat{\alpha})^{-1/2}}{(2\pi\hbar)^3w_F} \int \hat{\alpha}^{1/2}\mathbf{w}\hat{Q}\hat{\alpha}^{-1/2}\mathbf{w}dS(E_F), \\ \sigma_{ij} &= \frac{2e(\det\hat{\alpha})^{-1/2}}{(2\pi\hbar)^3w_F} \sum_l \alpha_i^{-1/2}\alpha_l^{-1/2}Q_{jl} \int w_jw_l dS(E_F), \\ \hat{Q} &= \left[\hat{\mu}^{-1} - \hat{B}\right]^{-1}, \quad \hat{\mu} = e\tau\hat{\alpha}.\end{aligned}$$

We assumed the low field limit and used a relation $-\partial f(\epsilon)/\partial\epsilon = \delta(\epsilon - E_F)$. The result of integration with S is given as

$$\int w_jw_l dS(E_F) = \frac{4\pi w_F^4}{3}\delta_{jl}, \quad (2.16)$$

and the conductivity tensor is given as the following form:

$$\hat{\sigma} = en\left(\hat{\mu}^{-1} \pm \hat{B}\right)^{-1}, \quad (2.17)$$

$$n = \frac{8\pi w_F^3}{3(2\pi\hbar)^3}\sqrt{(\det\hat{\alpha})^{-1}}, \quad (2.18)$$

where n is the carrier concentration. The sign \pm is corresponding to the charge sign of the carrier. Conductivity of tilted ellipsoids can be calculated by rotating the mobility tensor $\hat{\mu}$ as $\hat{R}^{-1}(\theta)\hat{\mu}\hat{R}(\theta)$, where $R(\theta)$ is a rotation matrix in three dimensional space. In the systems which can be described by multiple ellipsoidal Fermi surfaces, we can calculate the total conductivity tensor by summing up all the conductivity tensors of each ellipsoid.

$$\hat{\sigma} = \sum_i \hat{\sigma}^{(i)} \quad (2.19)$$

i is the index of different ellipsoids. We note that this approximation is appropriate only when the band structure can be approximated with parabolic curves. We will point in *Chap. 5* that some cases of the seemingly ellipsoidal Fermi surfaces cannot be discussed in this framework.

2.2 Quantum theory

The semiclassical theory does not consider the Landau quantization of carriers. For example, we cannot simulate the quantum oscillation in the transport coefficient in the semiclassical framework. Hence, we cannot describe the magneto-transport phenomena in a quite high field near and beyond the quantum limit. Typical metals have large Fermi energy and the cyclotron energy is relatively small, and we cannot approach the quantum limit with an available magnetic field. In this case, it is not necessary to care about the effect of Landau quantization and the semiclassical theory is useful. In contrast, semimetals or dilute semiconductors own small Fermi energy due to the small carrier concentration. Moreover, semimetals belonging to Dirac and Weyl electron systems have quite small effective carrier mass resulting in large cyclotron energy with moderately low magnetic field. In these materials, we can approach the quantum limit with a moderately low field and cannot neglect the effect of Landau quantization.

We will introduce an example of quantum treatment of magnetoresistance in free electron in solids with isotropic and anisotropic mass. We will show that the magneto-conductivity tensor has the same field-dependence as the semiclassical theory except that the carrier density exhibits oscillation at high field due to the Landau quantization. We calculate the components of the conductivity tensor by the Kubo formula [72] as shown below:

$$\sigma_{ij} = -\frac{1}{i} \left. \frac{\partial \Phi_{ij}}{\partial \omega} \right|_{\omega=0}, \quad (2.20)$$

$$\Phi_{ij} = \frac{2e^2}{\beta V} \sum_{n, \mathbf{k}} \text{Tr} [v_i \mathcal{G} v_j \mathcal{G}], \quad (2.21)$$

where Φ is the current-correlation function, v_i is the velocity operator, and $\mathcal{G} = (i\epsilon_n - \mathcal{H})^{-1}$ is the Green's function. \mathcal{H} is the Hamiltonian of free electron in magnetic field. $\beta = 1/k_B T$ and n is the index of the Matsubara frequency. V is the volume of the system. In the magnetic field, the velocity operator can be rewritten with $\pi_i/m = (p_i - eA_i)/m$. Taking the trace over the Landau indices l, l' , the correlation

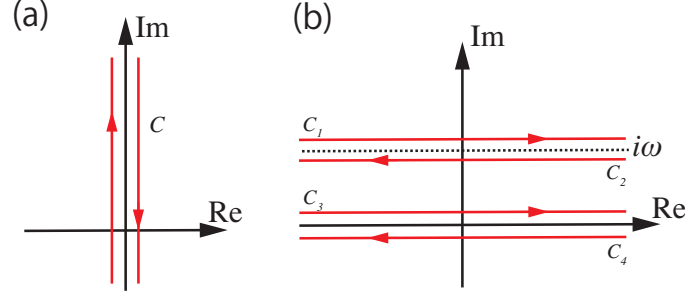


Figure 2.1: Pass integration of the correlation functions along the (a) imaginary axis and (b) real axis.

function is written in the following form:

$$\Phi_{ij}(i\omega) = \frac{2e^2}{Vm^2} \sum_{l,l'} \langle l|\pi_i|l'\rangle \langle l'|\pi_j|l\rangle F_{l'l}(i\omega),$$

$$F_{l'l}(i\omega) = \frac{1}{\beta} \sum_{n,k} g_{l'}(k, i\epsilon_n) g_l(k, i\epsilon_n - i\omega),$$

where $g_l = (i\epsilon_n - E_l)^{-1}$ and $E_l \left(= (l + \frac{1}{2})\hbar\omega_c + \frac{\hbar^2 k_z^2}{2m} \right)$ is the l th Landau level. $\omega_c = eB/m$ is cyclotron frequency, where B denotes the magnetic field. With the magnetic field along the z axis, the π operators in the plane of x - y plane can be written with ladder operators ($\pi_x = \sqrt{\hbar eB/2}(a^+ + a^-)$, $\pi_y = i\sqrt{\hbar eB/2}(-a^+ + a^-)$). a^+ and a^- are raising and lowering operators respectively. With the help of this treatment, we can conduct the summation over l' and get the following form:

$$\Phi_{xx}(i\omega) = \frac{e^3 \hbar B}{Vm^2} \sum_l [lF_{l-1,l} + (l+1)F_{l+1,l}], \quad (2.22)$$

$$\Phi_{xy}(i\omega) = -i \frac{e^3 \hbar B}{Vm^2} \sum_l [lF_{l-1,l} - (l+1)F_{l+1,l}]. \quad (2.23)$$

Next, we conduct the summation of Matsubara frequency n . By multiplying the Fermi distribution function, we can replace the summation with the pass integration along the imaginary axis in the complex plane (C in Fig. 2.1a). Furthermore, the pass of integral is transformed to four separated ones parallel to the real axis as

shown in Fig. 2.1b in order to avoid crossing the singularities of Green's functions ($i\epsilon_n = 0$, $i\epsilon_n = i\omega$). After an analytic continuation: $i\omega \rightarrow \hbar\omega + i\Gamma$ ($\Gamma = \hbar/2\tau$), $F_{\nu,l}$ can be written in the following form:

$$F_{\nu,l} = -\frac{1}{2\pi i} \sum_{\mathbf{k}} \int_{-\infty}^{\infty} dx n_F(x) [G_{\nu}^R(x + \hbar\omega)G_l^R(x) - G_{\nu}^R(x + \hbar\omega)G_l^A(x) \\ + G_{\nu}^R(x)G_l^A(x - \hbar\omega) - G_{\nu}^A(x)G_l^A(x - \hbar\omega)],$$

where n_F , G^A (G^R), and τ are the Fermi distribution function, advanced (retarded) Green's function, and electron lifetime due to the impurity scattering. The second and third terms including $G^A G^R$ and $G^R G^A$ are called the "Fermi surface" terms and refer to the contribution from the electrons at the Fermi energy. The other terms correspond to the contributions from lower energies and called "Fermi sea" terms. We are interested in the conduction contributed from the Fermi surface, hence we neglect the other terms in the correlation function and define the function $F_{\nu,l}^{\text{surf}}$ as shown below:

$$F_{\nu,l}^{\text{surf}} = \frac{1}{2\pi i} \sum_{\mathbf{k}} \int_{-\infty}^{\infty} dx n_F(x) [G_{\nu}^R(x + \hbar\omega)G_l^A(x) - G_{\nu}^R(x)G_l^A(x - \hbar\omega)] \\ = \frac{-1}{2\pi i} \sum_{\mathbf{k}} \int_{-\infty}^{\infty} dx [n_F(x + \hbar\omega) - n_F(x)] G_{\nu}^R(x + \hbar\omega)G_l^A(x) \\ \sim \frac{\hbar\omega}{2\pi i} \sum_{\mathbf{k}} \int_{-\infty}^{\infty} dx \left(-\frac{dn_F(x)}{dx} \right) G_{\nu}^R(x + \hbar\omega)G_l^A(x) \\ = \frac{\hbar\omega}{2\pi i} \sum_{\mathbf{k}} G_{\nu}^R(\mu + \hbar\omega)G_l^A(\mu),$$

where μ is the chemical potential. We discarded the higher expansion with ω because it vanishes by taking $\omega \rightarrow 0$ later. Substituting to the Eq. 2.22 and 2.23, the correlation functions are written in the following forms:

$$\Phi_{xx}(\omega) = \frac{e^3 \hbar^2 B \omega}{2\pi i V m^2} \sum_{\mathbf{k},l} (l+1) [G_{l+1}^R(\mu + \hbar\omega)G_l^A(\mu) + G_l^R(\mu + \hbar\omega)G_{l+1}^A(\mu)], \\ \Phi_{xy}(\omega) = -\frac{e^3 \hbar^2 B \omega}{2\pi i V m^2} \sum_{\mathbf{k},l} (l+1) [G_{l+1}^R(\mu + \hbar\omega)G_l^A(\mu) - G_l^R(\mu + \hbar\omega)G_{l+1}^A(\mu)].$$

According to the Eq. 2.20, each component of conductivity tensor is given in the following form:

$$\sigma_{xx} = \frac{e^3 \hbar^2 B N_L}{(2\pi)^2 m^2} \sum_l (l+1) \int_{-\infty}^{\infty} dk_z \left[\frac{1}{\hbar \omega_c - 2i\Gamma} \left(\frac{1}{\mu - E_{l+1} + i\Gamma} - \frac{1}{\mu - E_l - i\Gamma} \right) + c.c. \right],$$

$$\sigma_{xy} = -i \frac{e^3 \hbar^2 B N_L}{(2\pi)^2 m^2} \sum_l (l+1) \int_{-\infty}^{\infty} dk_z \left[\frac{1}{\hbar \omega_c - 2i\Gamma} \left(\frac{1}{\mu - E_{l+1} + i\Gamma} - \frac{1}{\mu - E_l - i\Gamma} \right) - c.c. \right].$$

We replaced the integration in k_x, k_y direction with the Landau degeneracy $N_L = eB/2\pi\hbar$ [15]. The integration of $G^{R,A}(\mu)$ with k_z is calculated as

$$\int_{-\infty}^{\infty} \frac{dk_z}{2\pi} \frac{1}{\mu - (l+1/2)\hbar\omega_c - \hbar^2 k_z^2 / 2m_z \pm i\Gamma}$$

$$= \mp i \frac{\sqrt{2m}}{2\hbar \sqrt{\mu - (l+1/2)\hbar\omega_c \pm i\Gamma}}.$$

Substituting this result, we get the final forms of σ_{xx} and σ_{xy} .

$$\sigma_{xx} = \frac{e^2 \tau}{m} \frac{1}{(\omega_c \tau)^2 + 1} \left(\frac{\sqrt{2m\mu}}{\hbar} \right)^3 \frac{(\gamma \omega_c \tau)^2}{2\pi^2} \sum_l \{ -\omega_c \tau \text{Im}[K_l] + (2l+1) \text{Re}[K_l] \}$$

$$\sigma_{xy} = -\frac{e^2 \tau}{m} \frac{1}{(\omega_c \tau)^2 + 1} \left(\frac{\sqrt{2m\mu}}{\hbar} \right)^3 \frac{(\gamma \omega_c \tau)^2}{2\pi^2} \sum_l \{ (2l+1) \omega_c \tau \text{Re}[K_l] + 2 \text{Im}[K_l] \}$$

$$K_l = \frac{1}{\sqrt{1 - (2l+1)\omega_c \tau \gamma + i\gamma}}, \quad \gamma = \frac{\Gamma}{\mu}$$

When $\Gamma \ll \mu$, they can be written as follows:

$$\sigma_{xx} = e\mu_e N(B) \frac{1}{(\omega_c \tau)^2 + 1}, \quad (2.24)$$

$$\sigma_{xy} = -e\mu_e N(B) \frac{\omega_c \tau}{(\omega_c \tau)^2 + 1}, \quad (2.25)$$

$$\mu_e = \frac{e\tau}{m},$$

$$N(B) = \left(\frac{\sqrt{2m\mu}}{\hbar} \right)^3 \left(\frac{\gamma \omega_c \tau}{\pi} \right)^2 \sum_l \left(l + \frac{1}{2} \right) \text{Re}[K_l].$$

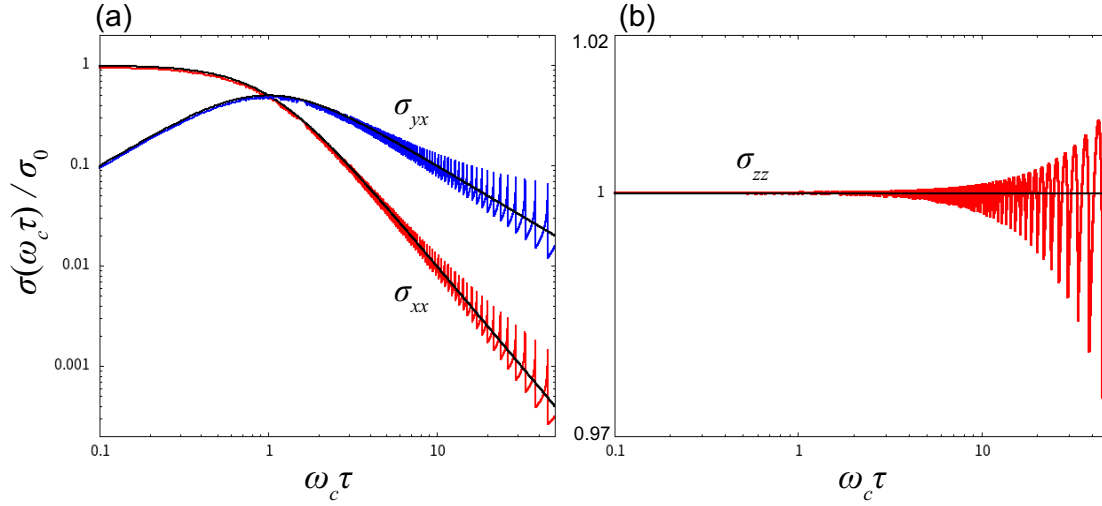


Figure 2.2: Field dependence of (a) σ_{xx} (red), σ_{yx} (blue), and (b) σ_{zz} (red) calculated from Kubo formula ($\Gamma/\mu = 0.002$). Black lines show the result from semiclassical theory. $\sigma_0 = e^2\tau n_e/m$ and $n_e = k_F^3/3\pi^2$

One can find that σ_{yx} is given by $-\sigma_{xy}$ because $\Phi_{yx} = -\Phi_{xy}$ due to the selection rule. These results are corresponding to an expansion of the Drude model to high magnetic field by considering the field-dependence carrier concentration. They are matched to the zero-field conductivity at $B \rightarrow 0$ limit and reproduce the field dependence of Boltzmann theory as shown in Fig. 2.2a. They can also simulate the quantum oscillation at high fields.

In three dimensional systems, the conductivity tensor has further five components. In the direction along the magnetic field (z axis), the velocity operator does not have transition components and the Fermi surface terms in correlation function can be written as follows:

$$\Phi_{zz}(i\omega) = \frac{2e^2}{\beta V m^2} \sum_{l,n,\mathbf{k}} p_z^2 g_l(k, i\epsilon_n) g_l(k, i\epsilon_n - i\omega)$$

$$\xrightarrow{\text{Fermi surface}} \frac{e^2 \hbar \omega}{\pi i V m^2} \sum_{\mathbf{k}, l} p_z^2 G_l^R(\mu + \hbar\omega) G_l^A(\mu).$$

Hence, the conductivity in z direction is obtained as follows:

$$\begin{aligned}
\sigma_{zz} &= \frac{e^2 \hbar}{\pi V m^2} \sum_{\mathbf{k}, l} \frac{p_z^2}{(\mu - E_l + i\Gamma)(\mu - E_l - i\Gamma)} \\
&= \frac{e^2 N_L}{2\pi^2 m^2} \sum_l \int_{-\infty}^{\infty} dp_z \frac{p_z^2}{(\mu - E_l + i\Gamma)(\mu - E_l - i\Gamma)} \\
&= \frac{e^2 N_L (\sqrt{2m})^3}{2\pi m^2 \Gamma} \sum_l \sqrt{\mu - (l + 1/2)\hbar\omega_c + i\Gamma} \\
&= e\mu_e N'(B), \tag{2.26} \\
N'(B) &= \left(\frac{\sqrt{2m\mu}}{\hbar} \right)^3 \frac{\gamma\omega_c\tau}{\pi^2} \sum_l \sqrt{1 - (2l + 1)\omega_c\tau\gamma + i\gamma}.
\end{aligned}$$

This value agrees with semiclassical theory at low fields and exhibits oscillation at high fields as shown in Fig. 2.2b. The other components (σ_{xz} and σ_{yz}) are zero because π_x and π_y are off-diagonal and π_z is diagonal. One can find the following relation:

$$\langle l | \pi_{x,y} | l' \rangle \langle l' | \pi_z | l \rangle = (C\delta_{l'-1,l} + C'\delta_{l'+1,l})\delta_{l',l} = 0. \tag{2.27}$$

Finally, we obtain the total conductivity tensor.

$$\hat{\sigma} = \begin{pmatrix} \sigma_{xx} & \sigma_{xy} & 0 \\ \sigma_{yx} & \sigma_{yy} & 0 \\ 0 & 0 & \sigma_{zz} \end{pmatrix} = e\mu_e \begin{pmatrix} \frac{N(B)}{(\omega_c\tau)^2 + 1} & -\frac{N(B)\omega_c\tau}{(\omega_c\tau)^2 + 1} & 0 \\ \frac{N(B)\omega_c\tau}{(\omega_c\tau)^2 + 1} & \frac{N(B)}{(\omega_c\tau)^2 + 1} & 0 \\ 0 & 0 & N'(B) \end{pmatrix} \tag{2.28}$$

σ_{xx} at high field limit and σ_{zz} take the same form as the results by Abrikosov [50]. Moreover, we can extend these results to the anisotropic electron by defining the effective mass in x, y, z direction independently in the framework of parabolic-dispersion approximation. In this case, the Hamiltonian of the ground state is

$$\mathcal{H} = \sum_{i=x,y,z} \frac{\pi_i^2}{2m_i}. \tag{2.29}$$

After the same calculations, we obtain the conductivity tensor as follows:

$$\hat{\sigma} = e \begin{pmatrix} \frac{\mu_x N(B)}{\mu_x \mu_y B^2 + 1} & -\frac{\mu_x \mu_y B N(B)}{\mu_x \mu_y B^2 + 1} & 0 \\ \frac{\mu_x \mu_y B N(B)}{\mu_x \mu_y B^2 + 1} & \frac{\mu_y N(B)}{\mu_x \mu_y B^2 + 1} & 0 \\ 0 & 0 & \mu_z N'(B) \end{pmatrix}, \quad (2.30)$$

$$N(B) = \frac{(\sqrt{2\mu})^3 \sqrt{m_x m_y m_z}}{\hbar^3} \left(\frac{\gamma \omega_c \tau}{\pi} \right)^2 \sum_l \left(l + \frac{1}{2} \right) \text{Re}[K_l],$$

$$N'(B) = \frac{(\sqrt{2\mu})^3 \sqrt{m_x m_y m_z}}{\hbar^3} \frac{\gamma \omega_c \tau}{\pi^2} \sum_l \sqrt{1 - (2l + 1) \omega_c \tau \gamma + i\gamma},$$

$$\mu_x = \frac{e\tau m_c}{m_x^2}, \quad \mu_y = \frac{e\tau m_c}{m_y^2}, \quad \mu_z = \frac{e\tau}{m_z}, \quad \omega_c = \frac{eB}{m_c}, \quad m_c = \sqrt{m_x m_y}.$$

This result formally agrees with the semiclassical theory for anisotropic electron [45].

In summary, it is shown that the magneto-conductivity with Landau quantization is given by replacing the constant carrier concentration in the semiclassical theory with field-dependent (oscillating) carrier density $N(B)$, $N'(B)$. For Dirac electron systems, previous theoretical research also showed that the quantum theory agrees with the semiclassical one at low fields and that the oscillation is superimposed at high fields [73].

Chapter 3

Dirac and Weyl electron in solids

Dirac electron in solids is characterized by the 4×4 Dirac Hamiltonian, which is known as the relativistic representation of Fermions in quantum physics [74]. Its linear dispersion yields a small effective mass [15, 57] resulting in high mobility. Strong spin-orbit coupling is the essential constitution of this system and consequential strong band interaction changes the fundamental features of electromagnetic properties [75–77]. Moreover, in topological aspects, various exotic magneto-transport characteristics are expected due to the non-trivial Berry curvature in the Dirac electron system [16]. It appears in solids such as an anomaly in quantum oscillation [78], negative MR [20], or sizable planar Hall effect with period π [21].

Weyl electron is also a non-trivial electron in solids, which is described with a mass-less Dirac Hamiltonian (Weyl Hamiltonian). Contrary to the Dirac electron, the Weyl electron in solids naturally includes some broken symmetry [16] and the system is categorized into some classes according to the symmetry. When there are two degenerating points in the Brillouin zone, this is so-called *Weyl-semimetal* [79]. When the degenerating point draws a continuous line, this class is *nodal line semimetal* [16, 79]. The Weyl semimetals contain a twin of Dirac cones, which are a divergence and convergence point of Berry curvature respectively [16].

Our purpose is to calculate the magneto-transport properties of these special types of electron systems on the basis of semiclassical theory. Especially, we are curious about the Landau quantization of the energy band and the fine structure of

Fermi surfaces. $k \cdot p$ theory is a powerful tool for obtaining elaborate energy dispersions near the symmetry points and the quantized band structures in the magnetic field. In this chapter, we introduce the concepts, various models, and beneficial consequences of this theory.

3.1 $k \cdot p$ theory

$k \cdot p$ theory

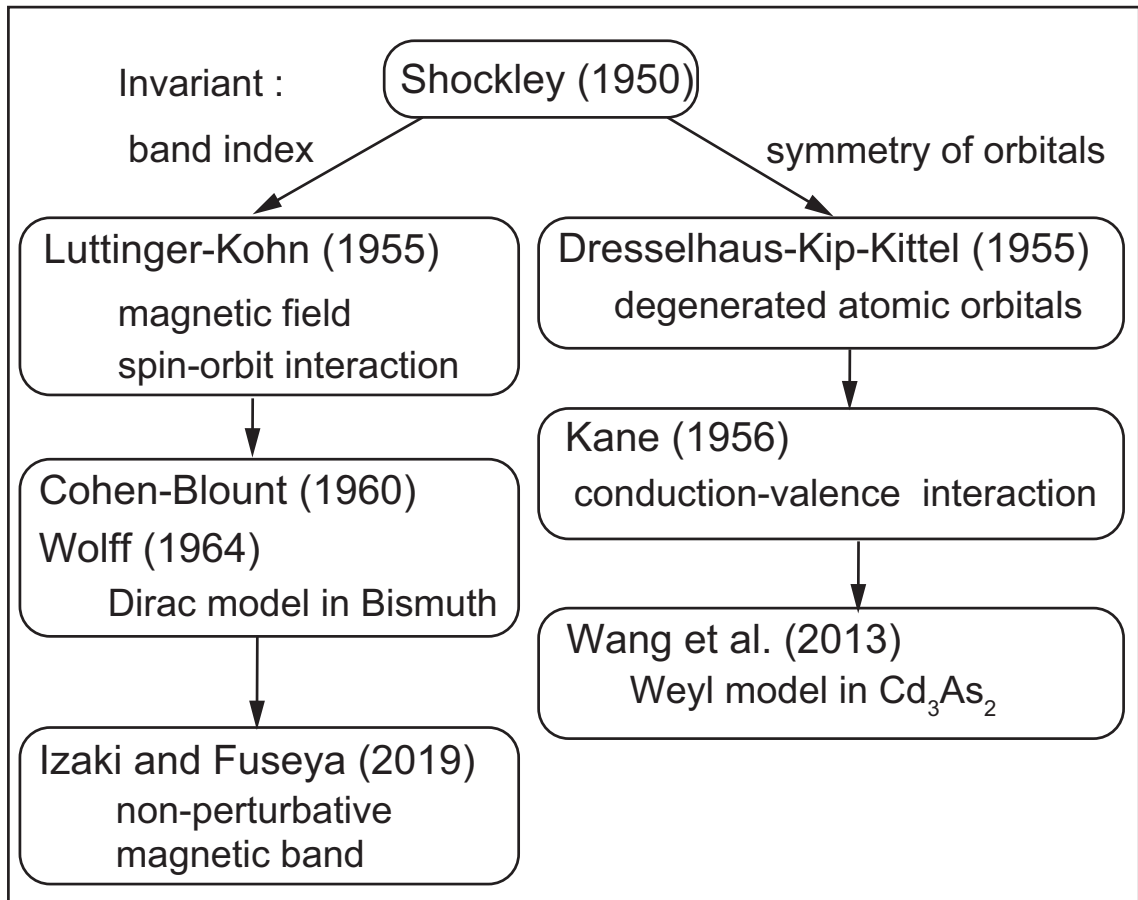


Figure 3.1: History and correlation of $k \cdot p$ models.

Electric carrier transport in semimetals and semiconductors are governed by the edge of the energy band because the structure determines the sign and scale of the effective mass of the carrier. Generally, the effective mass in crystal differs from bare electron mass due to the finite band interaction. The $k \cdot p$ theory can demonstrate the band interaction by selecting the Bloch wave function as a basis. Although the main concept is simple, we can apply this theory to variable cases by basis transformations.

The history and relations of several versions of theories are summarized in Fig. 3.1. The first insight was given by Shockley in 1950 [80]. The idea is to expand the eigenfunctions of electrons with plane waves. He renormalized the inter-band effect into the electron mass and successfully demonstrated the anisotropy of energy bands in semiconductors. Years later, the theory was improved and written in more general and useful forms by several researchers: Dresselhaus-Kip-Kittel (DKK) [81] and Luttinger-Kohn (LK) [82]. The concept of DKK theory was exploring the k -dependent band splitting in the valence band in semiconductors. They applied the perturbation theory to degenerated p -orbitals and pointed that the band interaction results in the band splitting. They also showed that the k -dependence is all quadratic without spin-orbit coupling.

Kane extended the DKK theory by considering interactions between valence and conduction bands, which make the band calculation available in narrow gap semiconductors [83, 84]. Now this theory is an essential tool for analyzing the band structure in topological materials with the inversion of valence and conduction bands [85–87]. DKK and Kane suggested the spin-orbit coupling yields linear dispersion. Recently, it was theoretically shown that the effective Hamiltonian at the Γ point of Cd_3As_2 can be described by the Weyl Hamiltonian due to the energy inversion of s - and p -orbitals and strong band interaction with the help of Kane model [87].

Luttinger and Kohn developed a discussion of perturbation which breaks the translational symmetry in systems including the magnetic field or impurity [82]. Especially, the gauge-invariant treatment of magnetic fields made an overwhelming impact on the following studies. With the help of this theory, we can easily obtain electron energy in the magnetic field. Following this, Cohen and Blount found that the energy band in bismuth is described by an isolated 2-band model [56]. Wolff

showed this 2-band system interacted by spin-orbit coupling can be written with Dirac Hamiltonian [57]. He also gave the Landau levels of an electron in bismuth. We want to note that DKK, Kane, and LK theory focus on the different types of invariants in the system: symmetry of orbits and band index respectively.

Recently, a non-perturbative treatment of magnetic fields in solids was established [88]. By substituting the non-commutative momentum operator in the magnetic field with the creation and annihilation operator of the harmonic oscillator, we can calculate the Landau levels of arbitrary tight-binding Hamiltonian with the help of matrix mechanics. This model was applied to a real material with Dirac electron and successfully simulate the field-dependence of effective g -factor.

3.1.1 The core concept of $k \cdot p$ theory

First, we introduce the general doctrine of $k \cdot p$ theory. The main purpose is obtaining the representation of perturbed Hamiltonian on the basis of unperturbed Bloch state. We begin with the Schrödinger equation and Bloch state shown as follows.

$$H\psi = \left[\frac{\mathbf{p}^2}{2m_e} + V(r) \right] \psi = E\psi \quad (3.1)$$

$$\psi = e^{i\mathbf{k}\cdot\mathbf{r}} u_{n,\mathbf{k}}(\mathbf{r}) \quad (3.2)$$

$V(r)$ is the potential of the crystal. Substituting the wave function, the equation can be rewritten as

$$\left[\frac{p^2}{2m} + \frac{\hbar}{m} \mathbf{k} \cdot \mathbf{p} + \frac{\hbar^2 \mathbf{k}^2}{2m} + V(\mathbf{r}) \right] u_{nk}(\mathbf{r}) = E u_{nk}(\mathbf{r}). \quad (3.3)$$

Using the Eq. 3.1, we obtain the following equation:

$$\left[H + \frac{\hbar}{m} \mathbf{k} \cdot \mathbf{p} + \frac{\hbar^2 \mathbf{k}^2}{2m} \right] u_{nk}(\mathbf{r}) = E u_{nk}(\mathbf{r}). \quad (3.4)$$

If we assume that \mathbf{k} is in the vicinity of the origin of the coordinate, the second and third terms of the left-hand side can be treated perturbatively. Now, we focus on the n -th band and the energy eigenvalue is calculated as

$$\epsilon_n(\mathbf{k}) = \epsilon_n(0) + \frac{\hbar^2 \mathbf{k}^2}{2m} + \frac{\hbar^2}{m^2} \sum_{j \neq n} \frac{|\langle n | \mathbf{k} \cdot \mathbf{p} | j \rangle|^2}{\epsilon_n(0) - \epsilon_j(0)}. \quad (3.5)$$

The inter-band effect is reflected through the transition amplitude of the \mathbf{p} operator. Defining the effective mass by the second derivative of energy with wave number, it is written as

$$\frac{1}{m^*} = \left[\frac{1}{\hbar^2} \frac{d^2 \epsilon_n(\mathbf{k})}{dk^2} \right] = \frac{1}{m} + \frac{2}{m^2} \sum_{j \neq n} \frac{|\langle n | \mathbf{p} | j \rangle|^2}{\epsilon_n(0) - \epsilon_j(0)}. \quad (3.6)$$

We can see that the inter-band effect results in the modulation of inverse effective mass. This is the reason this theory is often called *effective mass approximation*.

3.1.2 Dirac electron in solids

Dirac electron in three dimensional solid is characterized by the linear dispersion with crossing or anti-crossing point. It typically consists of 2-bands correlated through spin-orbit coupling. The inter-band effect especially changes fundamental physics, especially of the magnetic responses [75–77]. In the strong limit of the interaction in a 2-band system, the $k \cdot p$ Hamiltonian is identical to the Dirac Hamiltonian. Here, we show the derivation of the Hamiltonian according to the application to Bismuth electron [56, 57]. We begin with the electron in crystal with spin-orbit interaction as shown below.

$$\hat{H} = \frac{p^2}{2m} + V + \frac{\lambda^2}{8} \nabla^2 V + \frac{\lambda}{2mc} \mathbf{p} \cdot (\mathbf{s} \times \nabla V) \quad (3.7)$$

The λ is the Compton wavelength, c is the speed of light, and V is the crystal potential. We assume the two energy bands and the eigenfunctions are Bloch wave functions with Kramers indices.

$$|\phi_{n,s}(\mathbf{r})\rangle = e^{-i\mathbf{k}\mathbf{r}} |u_{n,s}(\mathbf{r})\rangle \quad n = 1, 2 \quad s = 1, 2 \quad (3.8)$$

According to the $\mathbf{k} \cdot \mathbf{p}$ method with two energy bands, we can obtain the components of the Hamiltonian with the basis of $|u_{n,s}\rangle$ as shown below.

$$\langle u_{n,s} | \hat{H} | u_{n',s'} \rangle = \left[E_{n,s} + \frac{\hbar^2 \mathbf{k}^2}{2m} \right] \delta_{n,n'} \delta_{s,s'} + \hbar \mathbf{k} \cdot \langle u_{n,s} | \mathbf{v} | u_{n',s'} \rangle + O(k^2) \quad (3.9)$$

$\mathbf{v} = \nabla_p \hat{H}$ is the velocity operator. Since the Kramers pair is related with the time-reversal operation $\hat{U} = i\sigma_y C$ (σ_y is one of the Pauli matrices and C is the conjugation

operator), we can obtain the relation between the k -linear components.

$$\langle u_{1,1} | \mathbf{v} | u_{2,1} \rangle = \langle u_{2,2} | \mathbf{v} | u_{1,2} \rangle \equiv \mathbf{t} \quad (3.10)$$

$$\langle u_{1,1} | \mathbf{v} | u_{2,2} \rangle = -\langle u_{2,1} | \mathbf{v} | u_{1,2} \rangle \equiv \mathbf{u} \quad (3.11)$$

When we assumed that the velocity at the band edge to be zero ($\langle u_{i,j} | \mathbf{v} | u_{i,j} \rangle = 0$), The 4×4 Hamiltonian is written as follows.

$$H_{\mathbf{k}\cdot\mathbf{p}} = \begin{bmatrix} \Delta & 0 & \hbar\mathbf{k} \cdot \mathbf{t} & \hbar\mathbf{k} \cdot \mathbf{u} \\ 0 & \Delta & -\hbar\mathbf{k} \cdot \mathbf{u}^* & \hbar\mathbf{k} \cdot \mathbf{t}^* \\ \hbar\mathbf{k} \cdot \mathbf{t}^* & -\hbar\mathbf{k} \cdot \mathbf{u} & -\Delta & 0 \\ \hbar\mathbf{k} \cdot \mathbf{u}^* & \hbar\mathbf{k} \cdot \mathbf{t} & 0 & -\Delta \end{bmatrix} + \frac{\hbar^2 \mathbf{k}^2}{2m} \quad (3.12)$$

Δ is the half gap between two bands. We can reduce the real part of \mathbf{t} by a unitary transformation S written as

$$S = \begin{pmatrix} S_1 & 0 \\ 0 & S_1^+ \end{pmatrix}, \quad S_1 = \left[1 + i \sum_{i=1}^3 (a_i \sigma_i) \right] / D, \quad D = \left[1 + \sum_{i=1}^3 (a_i)^2 \right]^{1/2},$$

and choosing the coefficient a_i to satisfy the following equation:

$$\left[1 - \sum_{i=1}^3 a_i^2 \right] \left(\frac{\text{Re}[\mathbf{t}] \cdot \mathbf{k}}{D^2} \right) - 2 \sum_{i=1}^3 a_i \left(\frac{\mathbf{K}_i \cdot \mathbf{k}}{D^2} \right) = 0,$$

where $\mathbf{K}_i = \{i = 1 : \text{Im}[\mathbf{u}], \quad 2 : \text{Re}[\mathbf{u}], \quad 3 : \text{Im}[\mathbf{t}]\}$. σ_i is the Pauli matrix and \mathbf{K}_i is corresponding to the intensity of band interaction including anisotropy. After this transformation, we obtain the final representation of the Hamiltonian.

$$H_{\text{Woff}} = SHS^{-1} = \Delta\beta + \frac{\hbar^2 \mathbf{k}^2}{2m} I + i\hbar\mathbf{k} \cdot \left[\sum_{i=1}^3 \mathbf{K}_i \beta \alpha_i \right] \quad (3.13)$$

$$\alpha_i = \begin{pmatrix} 0 & \sigma_i \\ \sigma_i & 0 \end{pmatrix} \quad \beta = \begin{pmatrix} I & 0 \\ 0 & -I \end{pmatrix}$$

This Hamiltonian is identical with a summation of free particle Hamiltonian and the Dirac Hamiltonian whose mass gap is corresponding to the bandgap. When we

consider the isotropic case, the intensity of band interaction is scaled by the following value.

$$\Gamma = \langle u_{1,1} | v | u_{2,2} \rangle \quad (3.14)$$

The major origin of this inter-band effect is spin-orbit coupling. The energy eigenvalue is given as

$$E(k) = \frac{\hbar^2 k^2}{2m} \pm \sqrt{\Delta^2 + \Gamma^2 (\hbar k)^2}. \quad (3.15)$$

We can see the dispersion becomes non-parabolic (linear) when the inter-band component is enough larger than the characteristic scale of energy Δ as shown in Fig. 3.2.

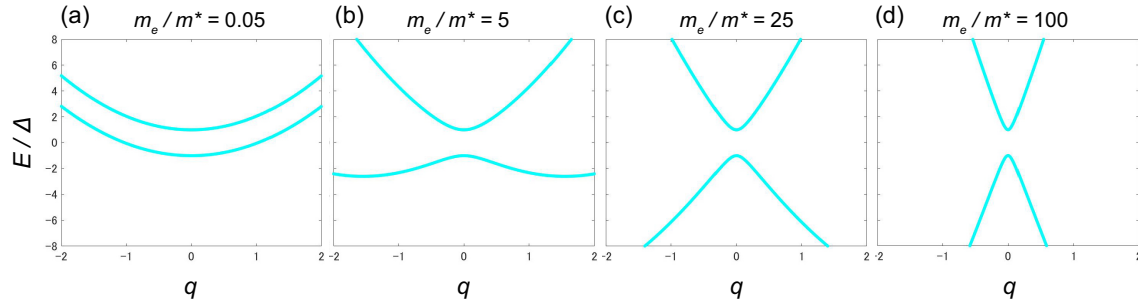


Figure 3.2: Two energy band interacting through the spin-orbit coupling. The energy and the wave number are normalized as $E/\Delta = q^2 + \sqrt{1 + 2(m_e/m^*)q^2}$ and $q^2 = \hbar^2 k^2 / 2m_e \Delta$. The ratio of masses corresponds to the intensity of band interaction.

3.2 Luttinger-Kohn theory

Luttinger and Kohn extended the $k \cdot p$ theory in 1955 and obtained a generalized representation of the Wannier equation [82]. This theory improved the applicability up to arbitrary symmetric points in the Brillouin zone and the cases with the external magnetic field or impurities, which break the symmetry of the system. After an

elegant transformation of the basis, we can easily simulate the energy bands in these perturbations.

The core of this theory is renormalizing the k -dependence of the basis of Bloch state $u_{n,k}$ into the plane wave components and selecting new basis as the following form:

$$\chi_{nk} = e^{i\mathbf{k}\cdot\mathbf{r}} u_{n0}. \quad (3.16)$$

This can be proved to be an orthonormal basis [82].

$$\langle \chi_{nk} | \chi_{n'k'} \rangle = \delta(\mathbf{k}' - \mathbf{k}) \delta_{nn'} \quad (3.17)$$

This simple formulation makes this theory tremendously useful. In the following sentences, we denote the wave function χ_{nk} with $|nk\rangle$.

3.2.1 $k \cdot p$ theory in the external magnetic field

We are especially interested in the band structure in the magnetic field. However, the external field breaks the symmetry of the system and makes it difficult to naïvely apply the Bloch theorem. The LK's representation gives a key to solving the conflict and shows the way to find the energy eigenvalues in the field by replacing the basis as shown above. The final conclusion is that the characteristic equation in the field can be re-written by replacing the momentum operator \mathbf{p} with the magnetic momentum $\boldsymbol{\pi} = \mathbf{p} + e\mathbf{A}$. All we should do is to find the solution of the Wannier equation with the $\boldsymbol{\pi}$ operator. We show the proof below [82, 89].

We assume the following vector potential.

$$A_x = -By, \quad A_y = 0, \quad A_z = 0, \quad (3.18)$$

which is corresponding to the magnetic field along the z -axis. Expanding the kinetic energy term, the Hamiltonian is written as

$$\begin{aligned} H &= H_0 + H_{kp} \\ &= H_0 + \frac{s}{m} y p_x + \frac{s^2}{2m} y^2 \quad (s = eB). \end{aligned} \quad (3.19)$$

H_0 is a non-perturbed Hamiltonian including kinetic energy, the periodic potential of crystal, and spin-orbit coupling. The matrix elements of perturbed Hamiltonian H_{kp} are calculated as follows:

$$\begin{aligned}
\langle n\mathbf{k} | y p_x | n'\mathbf{k}' \rangle &= \int e^{i(\mathbf{k}'-\mathbf{k})\cdot\mathbf{r}} u_{n0}^* y (\hbar k_x - i\hbar\nabla_x) u_{n'0} d\mathbf{r} \\
&= i \frac{\partial}{\partial k_y} \int e^{i(\mathbf{k}'-\mathbf{k})\cdot\mathbf{r}} u_{n0}^* (\hbar k_x - i\hbar\nabla_x) u_{n'0} d\mathbf{r} \\
&= (\hbar k_x \delta_{nn'} + p_{nn'}^x) \frac{1}{i} \frac{\partial \delta(\mathbf{k} - \mathbf{k}')}{\partial k_y'}, \tag{3.20}
\end{aligned}$$

$$p_{nn'}^\alpha = \frac{(2\pi)^3}{\Omega} \int_{\text{cell}} u_{n0}^* (-i\hbar\nabla_\alpha) u_{n'0} d\mathbf{r}, \tag{3.21}$$

$$\begin{aligned}
\langle n\mathbf{k} | y^2 | n'\mathbf{k}' \rangle &= \int y^2 e^{i(\mathbf{k}'-\mathbf{k})\cdot\mathbf{r}} u_{n0}^* u_{n'0} d\mathbf{r} \\
&= \left(\frac{1}{i} \frac{\partial}{\partial k_y'} \right)^2 \int e^{i(\mathbf{k}'-\mathbf{k})\cdot\mathbf{r}} u_{n0}^* u_{n'0} d\mathbf{r} \\
&= -\delta_{nn'} \frac{\partial^2 \delta(\mathbf{k} - \mathbf{k}')}{\partial k_y'^2}, \tag{3.22}
\end{aligned}$$

where Ω is the volume of the unit cell. Therefore, components of the total Hamiltonian is written as

$$\begin{aligned}
\langle n\mathbf{k} | H | n'\mathbf{k}' \rangle &= \left[\left(\epsilon_n(0) + \frac{\hbar^2 k^2}{2m} \right) \delta(\mathbf{k} - \mathbf{k}') + \frac{s\hbar^2 k_x}{m} \frac{1}{i} \frac{\partial \delta(\mathbf{k} - \mathbf{k}')}{\partial k_y'} - \frac{s^2 \hbar^2}{2m} \frac{\partial^2 \delta(\mathbf{k} - \mathbf{k}')}{\partial k_y'^2} \right] \delta_{nn'} \\
&\quad + \frac{1}{m} \left[\hbar \mathbf{k} \cdot \mathbf{p}_{nn'} \delta(\mathbf{k} - \mathbf{k}') + i s \hbar p_{nn'}^x \frac{\partial \delta(\mathbf{k} - \mathbf{k}')}{k_y'} \right]. \tag{3.23}
\end{aligned}$$

ϵ_n is the energy eigenvalue of the non-perturbed Hamiltonian. We can see the components are separated into intra-band and inter-band terms. In order to delete the inter-band terms, we conduct a unitary transformation noted with $e^{S'}$. First, we

expand the transformed Hamiltonian.

$$\begin{aligned} e^{-S'} H e^{+S'} &= H + [H, S'] + \frac{1}{2} [[H, S'], S'] + \dots \\ &= H^{(0)} + H_a + H_b + H' \\ &\quad + [H^{(0)}, S'] + [H_a, S'] + [H', S'] + \frac{1}{2} [[H^{(0)}, S'], S'] + \dots \end{aligned}$$

$$\langle n\mathbf{k} | H_a | n'\mathbf{k}' \rangle = -\frac{s\hbar^2 k_x}{m} \frac{1}{i} \frac{\partial \delta(\mathbf{k} - \mathbf{k}')}{\partial k_y'} \delta_{nn'} \quad (3.24)$$

$$\langle n\mathbf{k} | H_b | n'\mathbf{k}' \rangle = -\frac{s^2 \hbar^2}{2m} \frac{\partial^2 \delta(\mathbf{k} - \mathbf{k}')}{\partial k_y'^2} \delta_{nn'} \quad (3.25)$$

$$\langle n\mathbf{k} | H' | n'\mathbf{k}' \rangle = \frac{1}{m} \left[\hbar \mathbf{k} \cdot \mathbf{p}_{nn'} \delta(\mathbf{k} - \mathbf{k}') + i s \hbar p_{nn'}^x \frac{\partial \delta(\mathbf{k} - \mathbf{k}')}{\partial k_y'} \right] \quad (3.26)$$

After an ingenious choice of S' as

$$H' + [H^{(0)}, S'] = 0, \quad (3.27)$$

the expanded Hamiltonian is written in a simple form as follows.

$$e^{-S'} H e^{S'} \equiv H_{\text{exp}} = H^{(0)} + H_a + H_b + [H_a, S'] + \frac{1}{2} [H', S'] + \dots \quad (3.28)$$

Moreover, from the relation in Eq. 3.27, we can calculate the matrix elements of S' as follows.

$$\begin{aligned} \langle n\mathbf{k} | S' | n'\mathbf{k}' \rangle &= \begin{cases} -\langle n\mathbf{k} | H' | n'\mathbf{k}' \rangle / \hbar \omega_{n,n'} & (n \neq n') \\ 0 & (n = n') \end{cases} \\ \hbar \omega_{n,n'} &= E_n - E_{n'} \end{aligned} \quad (3.29)$$

From this relation and Eq. 3.26, one can see the scale of S' is $\sim k p_{nn'} / m \omega_{nn'}$. The order of physical quantities are typically $\hbar k \sim \sqrt{s}$, $p_{nn'} \sim \hbar/a$, $\omega_{nn'} \sim \hbar^2 / m a^2$, where a is the lattice constant. Hence, the amplitude of S' is about $(a/l_m)^2$. The l_m is the magnetic length given by $\sqrt{\hbar/eB}$ and has a scale of μm in a typical field. Then we can neglect the higher-order terms in Eq. 3.28. Since H_a is diagonal (Eq. 3.24) and S' is off-diagonal (Eq. 3.29) in the energy index, we get

$$\langle n\mathbf{k} | [H_a, S'] | n\mathbf{k}' \rangle = 0. \quad (3.30)$$

Next, $\langle n\mathbf{k} | [H', S'] | n\mathbf{k}' \rangle$ term is calculated as

$$\begin{aligned} \frac{1}{2} \langle n\mathbf{k} | [H', S'] | n\mathbf{k}' \rangle &= \frac{1}{m^2} \sum_{n' \neq n} \frac{1}{\omega_{nn'}} \left[k_\alpha k_\beta p_{nn'}^\alpha p_{n'n}^\beta \delta(\mathbf{k} - \mathbf{k}') \right. \\ &\quad \left. + s(k_\alpha + k'_\alpha) p_{nn'}^\alpha p_{n'n}^x \frac{1}{i} \frac{\partial \delta(\mathbf{k}' - \mathbf{k})}{\partial k'_y} - s^2 p_{nn'}^x p_{nn'}^x \frac{\partial^2 \delta(\mathbf{k} - \mathbf{k}')}{\partial k_y'^2} \right]. \end{aligned}$$

Applying the definition of effective mass shown in Eq. 3.6, the summation is renormalized in the mass and we get

$$\begin{aligned} \frac{1}{2} \langle n\mathbf{k} | [H', S'] | n\mathbf{k}' \rangle &= -\frac{1}{2m} \left\{ k_\alpha k_\beta \left[\delta_{\alpha\beta} - m \left(\frac{\partial^2 \epsilon_n(\mathbf{k})}{\partial k_\alpha \partial k_\beta} \right)_0 \right] \delta(\mathbf{k} - \mathbf{k}') \right. \\ &\quad \left. + s \left[(k_x + k'_x) - m(k_\alpha + k'_\alpha) \left(\frac{\partial^2 \epsilon_n(\mathbf{k})}{\partial k_\alpha \partial k_x} \right)_0 \right] \frac{1}{i} \frac{\partial \delta(\mathbf{k}' - \mathbf{k})}{\partial k_y'} \right. \\ &\quad \left. - s^2 \left[1 - m \left(\frac{\partial^2 \epsilon_n(\mathbf{k})}{\partial k_x^2} \right)_0 \right] \frac{\partial^2 \delta(\mathbf{k}' - \mathbf{k})}{\partial k_y'^2} \right\}. \end{aligned}$$

$(\dots)_0$ means $(\dots)_{\mathbf{k}=0}$. Using the following relation:

$$\begin{aligned} (k_x - k'_x) \partial \delta(\mathbf{k} - \mathbf{k}') / \partial k_y' &= 0, \\ (k_y - k'_y) \partial \delta(\mathbf{k} - \mathbf{k}') / \partial k_y' &= \delta(\mathbf{k} - \mathbf{k}'), \end{aligned}$$

we obtained the components of the full Hamiltonian as follows.

$$\begin{aligned} \langle n\mathbf{k} | \bar{H} | n\mathbf{k}' \rangle &= \epsilon_n(\mathbf{k}) \delta(\mathbf{k} - \mathbf{k}') + s k_\alpha \left(\frac{\partial^2 \epsilon_n(\mathbf{k})}{\partial k_\alpha \partial k_x} \right)_0 \frac{1}{i} \frac{\partial \delta(\mathbf{k} - \mathbf{k}')}{\partial k_y'} \\ &\quad + \frac{is}{2} \left(\frac{\partial^2 \epsilon_n(\mathbf{k})}{\partial k_x \partial k_y} \right)_0 \delta(\mathbf{k} - \mathbf{k}') - \frac{1}{2} s^2 \left(\frac{\partial^2 \epsilon_n(\mathbf{k})}{\partial k_x^2} \right)_0 \frac{\partial^2 \delta(\mathbf{k} - \mathbf{k}')}{\partial k_y'^2} \end{aligned}$$

The Schrödinger equation corresponding to this Hamiltonian is written in the following form:

$$\left\{ \epsilon_n(\mathbf{k}) + is \left[k_\alpha \left(\frac{\partial^2 \epsilon_n(\mathbf{k})}{\partial k_\alpha \partial k_x} \right)_0 \frac{\partial}{\partial k_y} + \frac{1}{2} \left(\frac{\partial^2 \epsilon_n(\mathbf{k})}{\partial k_x \partial k_y} \right)_0 \right] - \frac{s^2}{2} \left(\frac{\partial^2 \epsilon_n(\mathbf{k})}{\partial k_x^2} \right)_0 \frac{\partial^2}{\partial k_y^2} \right\} B_n(\mathbf{k}) = \epsilon B_n(\mathbf{k}).$$

After the Fourier transformation, we obtain the final form of the equation as follows:

$$\left[\epsilon_n \left(\frac{\nabla}{i} \right) + \frac{s}{2} \left(\frac{\partial^2 \epsilon_n(\mathbf{k})}{\partial k_\alpha \partial k_x} \right)_0 \left(y \frac{\nabla_\alpha}{i} + \frac{\nabla_\alpha}{i} y \right) + \frac{s^2}{2} \left(\frac{\partial^2 \epsilon_n(\mathbf{k})}{\partial k_x^2} \right)_0 y^2 \right] F_n(\mathbf{r}) = \epsilon F_n(\mathbf{r}), \quad (3.31)$$

where $F_n(\mathbf{r}) = \int d\mathbf{k} e^{i\mathbf{k}\cdot\mathbf{r}} B_n(\mathbf{k})$. Comparing with the Schrödinger equation without the magnetic fields in the framework of $k \cdot p$ method given as

$$\left[E_n(\mathbf{0}) + \frac{k_i k_j}{2} \left(\frac{\partial^2 E_n(\mathbf{k})}{\partial k_i \partial k_j} \right)_0 \right] F_n(\mathbf{r}) = \epsilon F_n(\mathbf{r}), \quad (3.32)$$

the Hamiltonian in Eq. 3.31 can be obtained by replacing the momentum \mathbf{p} with the magnetic momentum $\boldsymbol{\pi} = \mathbf{p} + e\mathbf{A}$.

3.2.2 Dirac electron in the magnetic field

With the help of L-K theory, the Hamiltonian of Dirac electron in the magnetic field can be written in the following form:

$$H = \begin{pmatrix} \Delta & i\Gamma \boldsymbol{\pi} \cdot \boldsymbol{\sigma} \\ -i\Gamma \boldsymbol{\pi} \cdot \boldsymbol{\sigma} & -\Delta \end{pmatrix}. \quad (3.33)$$

The square of this Hamiltonian can be block-diagonalized as,

$$\begin{aligned} H^2 &= \begin{pmatrix} \Delta^2 + \Gamma^2(\boldsymbol{\pi} \cdot \boldsymbol{\sigma})(\boldsymbol{\pi} \cdot \boldsymbol{\sigma}) & 0 \\ 0 & \Delta^2 + \Gamma^2(\boldsymbol{\pi} \cdot \boldsymbol{\sigma})(\boldsymbol{\pi} \cdot \boldsymbol{\sigma}) \end{pmatrix}, \\ (\boldsymbol{\pi} \cdot \boldsymbol{\sigma})(\boldsymbol{\pi} \cdot \boldsymbol{\sigma}) &= \begin{pmatrix} \hbar^2 k_z^2 + 2\pi_- \pi_+ & 0 \\ 0 & \hbar^2 k_z^2 + 2\pi_+ \pi_- \end{pmatrix}, \end{aligned}$$

where π_{\pm} are the ladder operators of Landau levels. The products of these operators can be calculated as follows:

$$\begin{aligned} 2\pi_+ \pi_- &= \pi_x^2 + \pi_y^2 + i(\boldsymbol{\pi} \times \boldsymbol{\pi})_z \\ &= (2l + 1)e\hbar B + e\hbar B, \\ 2\pi_- \pi_+ &= \pi_x^2 + \pi_y^2 - i(\boldsymbol{\pi} \times \boldsymbol{\pi})_z \\ &= (2l + 1)e\hbar B - e\hbar B. \end{aligned} \quad (3.34)$$

l is the index of Landau levels. Finally, we get the quantized energy of the Dirac electron in the magnetic field by solving the equation $H^2\psi = E^2\psi$.

$$E_{l,s} = \pm \sqrt{\Delta^2 + 2\Gamma^2 \left[\left(l + \frac{s}{2} + \frac{1}{2} \right) e\hbar B + \frac{\hbar^2 k_z^2}{2} \right]} \quad (3.35)$$

We can see that the states with the same total angular momentum $j = l + s/2 + 1/2$ degenerate. In a 2-band model with a strong interaction ($\Delta \ll E_F$), the effective mass is given as

$$\frac{1}{m^*} \sim \frac{\Gamma^2}{\Delta},$$

hence the Landau level is rewritten as the following form:

$$E_{l,s} = \pm \sqrt{\Delta^2 + 2\Delta \left[\left(l + \frac{s}{2} + \frac{1}{2} \right) \hbar\omega_c + \frac{\hbar^2 k_z^2}{2m_z} \right]}. \quad (3.36)$$

3.2.3 Landé g -factor

We have reviewed a concept of $k \cdot p$ theory. The main feature is the modulation of effective mass by the band interactions. When we take the spin-orbit interaction and magnetic field into account, another respect of band interaction appears as the modulation of Zeeman splitting. The g -factor of a bare electron is 2. On the other hand, it largely deviates from this value for electrons in some materials [54, 90, 91]. Roth [92] first discussed this effect by perturbatively treating the magnetic field (Lödin partitioning [93]). We can expand the additional Zeeman split of degenerated bands ΔE with the commutators of wave vector as shown below.

$$\begin{aligned} \Delta E = \frac{1}{m_0^2} \sum_{E_l \neq E_n} \left\{ \left[\frac{\langle n | p_x | l \rangle \langle l | p_y | n \rangle - \langle n | p_y | l \rangle \langle l | p_x | n \rangle}{E_n - E_l} \right] [p_x, p_y] \right. \\ + \left[\frac{\langle n | p_z | l \rangle \langle l | p_x | n \rangle - \langle n | p_x | l \rangle \langle l | p_z | n \rangle}{E_n - E_l} \right] [p_z, p_x] \\ \left. + \left[\frac{\langle n | p_y | l \rangle \langle l | p_z | n \rangle - \langle n | p_z | l \rangle \langle l | p_y | n \rangle}{E_n - E_l} \right] [p_y, p_z] \right\} \end{aligned} \quad (3.37)$$

When the magnetic field is applied along with the z -direction, only one commutator $[\pi_x, \pi_y]$ remains and we obtain

$$\begin{aligned} \Delta E &= -ie \frac{\hbar}{m_0^2} B_z \sum_{E_l \neq E_n} \frac{\langle n | \pi_x | l \rangle \langle l | \pi_y | n \rangle - \langle n | \pi_y | l \rangle \langle l | \pi_x | n \rangle}{E_n - E_l} \\ &\equiv \frac{\Delta g \mu_B s B_z}{2}. \end{aligned} \quad (3.38)$$

The effective g -factor $g_{\text{eff}} = g_0 + \Delta g$ is clearly modulated by the band interactions. Carriers in bismuth crystals are the typical example. As mentioned before, the electron in bismuth is well approximated with the Dirac electron [56,57]. Two energy band is correlated with spin-orbit coupling so strongly that the Zeeman split has the same value with the cyclotron energy, which corresponds to the energy degeneration shown in the Eq. 3.36. It is experimentally confirmed that the enhancement of effective g -factor in bismuth electron is isotropic [54]. On the other hand, the case of the hole is different. The Zeeman split is almost twice as large as the cyclotron energy in the trigonal axis [54,94–97], while it is negligibly small in binary and bisectrix directions. Recently, the origin of these mysterious characteristics was unveiled [98] by explicitly calculating the inter-band effect from the tight-binding model. Although the gap between the T_{45} (hole carrier) and Γ_6 bands are nearly 1 eV, the spin-orbit coupling in bismuth has a comparable scale (~ 1.8 eV [90]) and make these bands coupled.

3.2.4 Inter-band effect and adiabatic phase

The recent viewpoint of topological materials has renewed the interest in the band interaction in the magnetic field. It was figured out that the Landau quantization of the energy band reflects the information of the Berry phase [78]. Berry phase is a phase in wave function in parametric space. While this phase is implicit in the Schrödinger equation of free particle, it arises with non-trivial phenomena in some multi-band systems. In the case of electrons in crystals, the adiabatic parameter is the wave number \mathbf{k} . The phase is stimulated to the electron wave when the electron wave travels through the Brillouin zone, which is reminiscent of the Aharonov Bohm effect in the external magnetic field. We can regard this phase in the wave space as an effect of a virtual magnetic field. We call this intrinsic magnetic field *Berry curvature*. Some types of crystals possess topologically protected *Dirac cone*, which is the crossing point of linear bands in the Brillouin zone. This singularity in the band structure can be a diverging point of Berry curvature, which is identical to a magnetic monopole [16]. For example, insulators with non-trivial \mathbb{Z}_2 index is called *topological insulator* and it has a conducting state with the Dirac cone on its

surface [99]. Another example is the Weyl electron system. This system has some types of breaking of spatial symmetry, which results in a twin of Dirac cones (Weyl point) or line of degeneration (nodal line) in k -space [16].

We can extract the information of Berry phase out of the quantum oscillation. Mikitik *et al.* proposed that phase of the oscillation includes the Berry phase directly [78]. The cross-sectional area of l -th Landau tube in the Brillouin zone is given by [100]

$$S(B) = \frac{2\pi eB}{\hbar}(l + \gamma) \quad (3.39)$$

in the framework of semiclassical electron trajectory in k -space. When this area becomes maximized, the oscillation in electron-transport coefficients is observed. The additional constant γ is corresponding to the phase shift of the oscillation and is equal to 1/2 when there is no inter-band effect: free electron. They showed that the phase in a n -th Bloch band can be written as [101]

$$\gamma_n = \frac{1}{2} - \frac{1}{2\pi} \oint \Omega_n d\mathbf{k}. \quad (3.40)$$

$$\Omega_n(\mathbf{k}) = i \int d\mathbf{r} u_{\mathbf{k},n}^* \nabla_k u_{\mathbf{k},n}. \quad (3.41)$$

$\Omega_n(\mathbf{k})$ is the Berry phase in the k -space. When the contour of electron trajectory includes the level-crossing point, which is corresponding to the Dirac cone mentioned above, the Berry-phase term becomes non-zero. $\gamma = 1$ is realized in Dirac electrons.

The relation between the Berry phase and quantum oscillation can be translated in terms of effective g -factor. In the case of free electrons with light mass in solids, the levels of the Kramers pair are almost degenerated due to the relatively small Zeeman splitting (Fig. 3.3a). On the other hand, in the strong limit of 2-band interaction: Dirac electron, the degenerated energies are shifted due to strong spin-orbit coupling. In the Dirac electron, the degenerated pair has the same total angular momentum in the z direction (Fig. 3.3b). The peaks of quantum oscillation are corresponding to the crossing point of the bottoms of Landau levels and Fermi energy. Hence, the position of peak is given in the following relation:

$$(n + 1/2)\hbar\omega_c = E_F, \quad (\text{Free electron}) \quad (3.42)$$

$$\sqrt{\Delta^2 + 2\Delta j\hbar\omega_c} = E_F, \quad (\text{Dirac electron}) \quad (3.43)$$

where $j = l + s/2 + 1/2$. When we plot the index corresponding to the peaks of quantum oscillation as a function of inverse-field ($1/B$), the points are distributed in a co-linear line. Moreover, the line has an intercept at $1/2$ in the case of a free electron and crosses the origin in Dirac electron (Fig. 3.3c). This map is called *fan diagram*, and we can determine the additional phase of an electron from the intercept of lines [6,54,102–105]. In more complicated multi-band systems ($n > 3$), the intercepts deviate from integer or half-integer. The degree of shift is measured with the ratio of the Zeeman split to the cyclotron energy called *Zeeman cyclotron ratio* (denoted with M [77]). Recently, the $k \cdot p$ theory was extended beyond the framework of Lödin partitioning and we can treat the magnetic field non-perturbatively in band calculation with the help of matrix mechanics [88]. This method pointed out that the ratio M in PbTe, which has been approximated with the Dirac electron system, has field dependence due to additional inter-band effects from outside of 2-band.

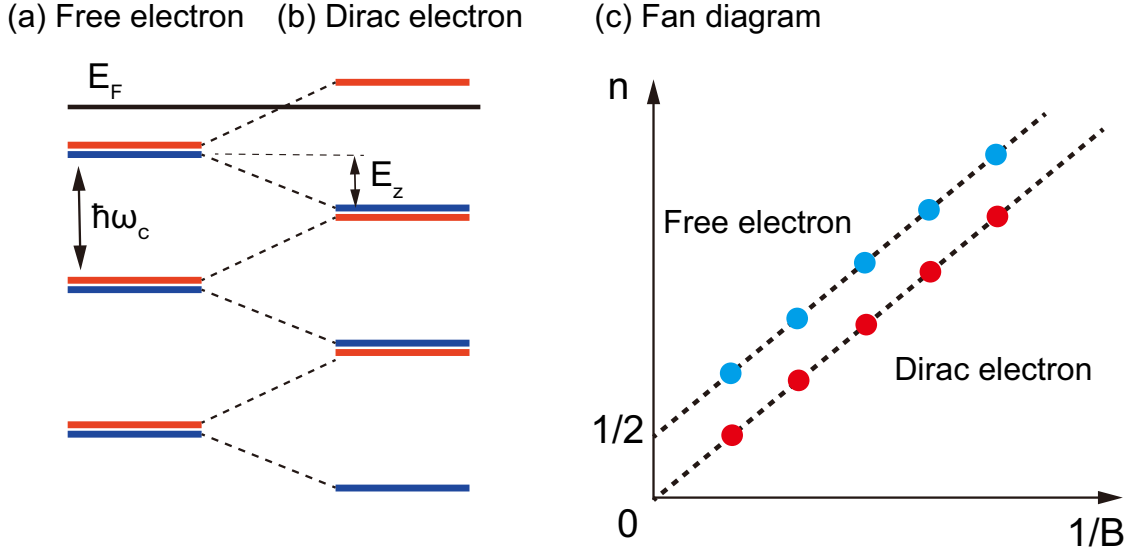


Figure 3.3: Band edge of Landau levels in (a) Free electron and (b) Dirac electron. (c) Fan diagram of free and Dirac electron.

We can also find the relationship between the effective g -factor from the inter-band effect and the Berry curvature. The Berry curvature in the Brillouin zone is

given by [24, 106]

$$\mathbf{B}_n(\mathbf{k}) = \text{Im} \sum_{E_m \neq E_n} \frac{\langle n(\mathbf{k}) | \mathbf{v} | m(\mathbf{k}) \rangle \times \langle m(\mathbf{k}) | \mathbf{v} | n(\mathbf{k}) \rangle}{(E_m(\mathbf{k}) - E_n(\mathbf{k}))^2}. \quad (3.44)$$

This is clearly correlated with the effective g -factor in Eq. 3.38. We can say that the band proximity enhances the local Berry curvature in the Brillouin zone. Moreover, in the strongly correlated 2-band system, they are perfectly proportional to each other.

3.3 Kane model

Kane extended the DKK model by considering the interaction between valence and conduction band in narrow-gap semiconductor InSb [83]. The main concept is selecting the basis of atomic orbitals at the symmetry points as DKK theory. This method successfully explains the non-parabolic band structure in the narrow gap materials [84] and topological materials [85–87]. By considering the inversion of s, p -orbitals, and spin-orbit coupling, we can demonstrate the exotic band structures in Weyl electron systems.

3.3.1 Weyl electron system

The energy dispersion of Weyl electron indicates the linear k -dependence in specific directions and parabolic dependence in other directions [16, 107, 108]. Contrary to the Dirac electron, *Weyl semimetals* own a twin of degenerated points called *Weyl points*. This system fundamentally has broken symmetry in some direction. To take the anisotropy into account, we have to begin with the Kane model, which is based on the orbital symmetry of bands.

In the Kane model, the Hamiltonian up to the second order with k is given in the following form [109]:

$$\langle X | H_{\text{Kane}} | Y \rangle = E_X \delta_{X,Y} + \frac{\hbar}{m} \mathbf{k} \cdot \langle X | \mathbf{P} | Y \rangle + \frac{\hbar^2}{m^2} \sum_x \frac{\langle X | \mathbf{k} \cdot \mathbf{P} | x \rangle \langle x | \mathbf{k} \cdot \mathbf{P} | Y \rangle}{E_X - E_x}, \quad (3.45)$$

where X, Y are the indices of orbits ($X, Y = s, p \dots$). In isotropic case with basis ($|s\rangle, -i|Z\rangle, -i|Y\rangle, -i|Z\rangle$), the inter-band term (off-diagonal) is calculated as

$$\frac{\hbar}{m} \langle s | \mathbf{k} \cdot \mathbf{P} | p_i \rangle = -i \frac{\hbar}{m} k_i \langle s | P_i | i \rangle \equiv A k_i. \quad (3.46)$$

Then, the Hamiltonian can be expressed as the following form:

$$H_{\text{Kane}} = \epsilon_0(k) + \begin{pmatrix} M(k) & A k_x & A k_y & A k_z \\ A^* k_x & -M(k) & 0 & 0 \\ A^* k_y & 0 & -M(k) & 0 \\ A^* k_z & 0 & 0 & -M(k) \end{pmatrix}, \quad (3.47)$$

$$M(k) = \Delta + \frac{\hbar^2}{m^2} \sum_{i=x,y,z} k_i^2 \frac{|\langle s | \mathbf{P} | p_i \rangle|^2}{E_s - E_p}. \quad (3.48)$$

Δ is the half band gap between the s - and p -bands. The eigenvalues are given as

$$E = \epsilon_0(k) \pm \sqrt{M(k)^2 + A^2 k^2}. \quad (3.49)$$

$\epsilon_0(k)$ is the parabolic dispersion of bare electron. Without the inter-band interaction, the energy dispersions are just a pair of parallel parabolic curves as shown in Fig. 3.4a. With the second perturbation $M(k)$, the curvature of the bands are modulated and the p -band becomes hole-like (Fig. 3.4b). If the order of these bands is inverted at $k = 0$ ($\Delta < 0$), these arcs get over-wrapped as shown in Fig. 3.4c. The degeneracy at $E = 0$ is broken as long as the inter-band interaction A is non-zero. In order to obtain the Weyl-type dispersion with two degenerated points in a specific direction, we have to consider the spin degrees of freedom and spatial asymmetry.

We demonstrate a derivation of Weyl Hamiltonian in accordance with the down-folded 8×8 Hamiltonian for the Γ point of Cd_3As_2 by Wang *et al.* [87]. For simplicity, we assume four s and p orbitals with spin ($|s, \uparrow\rangle, |p, \uparrow\rangle, |s, \downarrow\rangle, |p, \downarrow\rangle$). Especially, $|p, \uparrow \downarrow\rangle$ can be written as $|p_x\rangle \pm i|p_y\rangle$, and the s - p interaction is given by,

$$H_{\text{inter}} = \frac{\hbar}{m} \langle s \uparrow | \mathbf{k} \cdot \mathbf{P} | p \uparrow \rangle = \frac{\hbar}{m} \langle s \uparrow | \mathbf{k} \cdot \mathbf{P} \{ |p_x\rangle + i |p_y\rangle \} \equiv A k_+. \quad (3.50)$$

$$k_{\pm} = kx \pm iky$$

The 4×4 Hamiltonian is given as follows.

$$H_{\text{Cd}_3\text{As}_2}^{\Gamma} = \epsilon_0(k) + \begin{pmatrix} M(k) & Ak_+ & 0 & 0 \\ Ak_- & -M(k) & 0 & 0 \\ 0 & 0 & M(k) & -Ak_- \\ 0 & 0 & -Ak_+ & -M(k) \end{pmatrix} \quad (3.51)$$

This Hamiltonian is block-diagonalized, and we can decouple the 2×2 Hamiltonian out of it. The decoupled part can be written as

$$H_{2 \times 2} = M(k)\sigma_z + A(k_x\sigma_x + k_y\sigma_y), \quad (3.52)$$

where σ_i is the Pauli matrix. The eigenvalues are,

$$E = \epsilon_0(k) \pm \sqrt{M(k)^2 + A^2k_+k_-}. \quad (3.53)$$

In this case, the degeneracy in the k_z direction cannot be broken with finite A (Fig. 3.4d), and the dispersion in other directions asymptotically becomes Dirac-like when the band-interaction becomes larger (Fig. 3.4e,f).

To summarize, the Weyl dispersion is originated from the band inversion of s, p -bands at a band edge, the symmetry breaking, and large band interaction.

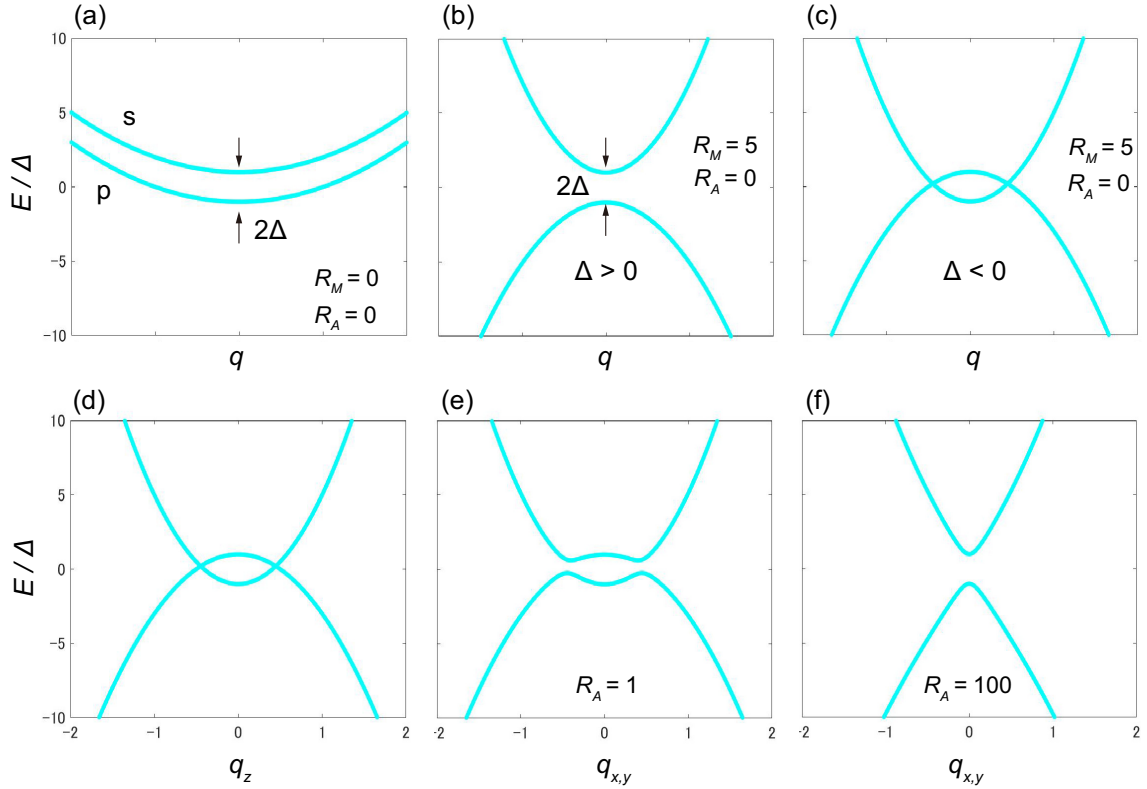


Figure 3.4: Energy dispersion of (a) free electron and (b-f) 2-band Kane model for interacting s and p orbitals. The energy and the wave number are normalized as $E/|\Delta| = q^2 + \sqrt{(\text{sign}(\Delta) + R_M q^2)^2 + R_A q'^2}$, where $q^2 = \hbar^2 k^2 / 2m_e |\Delta|$. $q'^2 = q^2$ for (b,c) and $q'^2 = q_x^2 + q_y^2$ for (d-f).

Chapter 4

Magnetoresistance in Bismuth

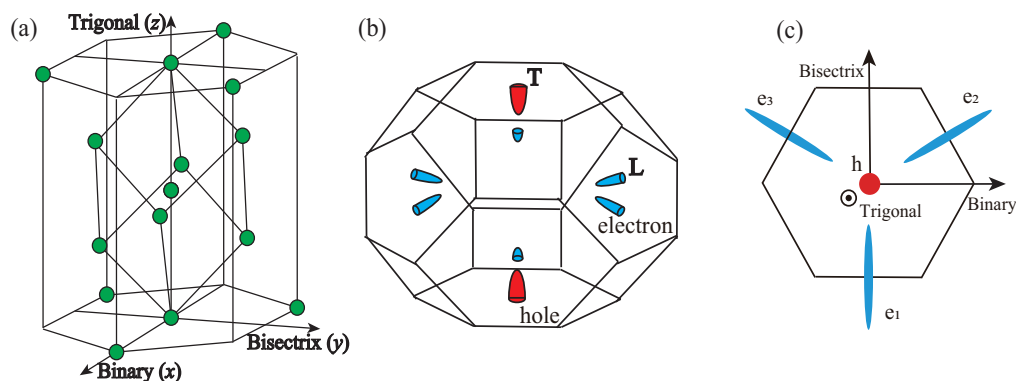


Figure 4.1: (a) Unit cell of bismuth crystal. (b) The first Brillouin zone and carrier pockets and (c) the view from T point.

Bismuth is one of the oldest materials in the history of solid-state physics. Novel phenomena have been discovered through the exploration of the properties of this material. The diamagnetism [110, 111], Nernst effect [112], huge magnetoresistance [1], Shubnikov-de Haas effect [2], and de Haas-van Alphen effect [113] were observed first in bismuth crystal. The tremendous contribution is not a coincidence. One remarkable character of bismuth is a huge magnetic response due to the existence of Dirac electrons [15, 75]. Moreover, the small carrier mass makes the quantum oscillation observable in a moderately low field. In the magneto-transport aspect,

bismuth is a semimetal with dilute electron- and hole-carriers compensating each other resulting in huge magnetoresistance.

Recently, the experimental studies observed angular-dependent magnetic response comprehensively and found new mysteries. Bismuth has binary (x), bisectrix (y), and trigonal (z) axis. While the transverse magnetoresistance is expected to show six-fold rotational symmetry with the rotating field in the x - y plane, the observations indicated the suppression of the anisotropy [40, 44, 45] or symmetry breaking [44, 45, 114] at the quantum limit ($\gtrsim 10$ T). Moreover, an extremely large field exceeding 40 T yields an unexpected drop in MR [40]. These characteristics cannot be explained by conventional semiclassical transport theory. The point is that these anomalies arise around the quantum limit. In this range, the effect of Landau quantization is not negligible.

In calculating MR, we took the Landau quantization into account through the field-dependent carrier concentrations. Bismuth is one of the most suitable systems for our purpose because the anisotropic masses and effective g -factors of electron and hole are precisely determined by previous researches [45, 54, 94] and we can calculate the field dependence of Landau levels of carriers without ambiguity in all directions of the magnetic field. Moreover, the Fermi surfaces in bismuth are all ellipsoidal and we can apply the multiple anisotropic carrier model [44, 45, 115] (ellipsoidal model) to describe the magnetoresistivity.

4.1 Magnetoconductivity

Bismuth single crystal contains three small electron pockets at L points and one hole pocket at T point in the Brillouin zone (Fig. 4.1b,c). Approximating these carrier pockets with ellipsoids, we can calculate the magnetoconductivity tensor by the method shown in the *Sec.* 2.1.2. Moreover, the magnetoconductivity with Landau quantization can be given by replacing the constant carrier density with the summation of the density of state in all the Landau levels below the Fermi energy. The magneto-conductivity tensor $\hat{\sigma}$ in bismuth is calculated as follows:

$$\hat{\sigma} = \sum_i eN_{ei}(B) \left(\hat{\mu}_{ei}^{-1} - \hat{B} \right)^{-1} + eN_h(B) \left(\hat{\mu}_h^{-1} + \hat{B} \right)^{-1}. \quad (4.1)$$

The indices of summation are the number of electron pockets. Due to the symmetry around the trigonal axis, the mobility tensors of three electrons can be given by rotating one of them by $\pm 2\pi/3$. The carrier density of electron N_{ei} , hole N_h , and the Fermi energy are determined by the charge neutrality condition of the carriers in the magnetic field:

$$\sum_i N_{ei}(B) = N_h(B). \quad (4.2)$$

The carrier density in the field is calculated by summing up the density of states in each Landau level. One Landau level has field-dependent degeneracy in x - y plane (B/z), which is called Landau degeneracy $N_L = eB/2\pi\hbar$. The carrier density in one carrier pocket at $T = 0$ K is calculated as follows:

$$\begin{aligned} N(B) &= \sum_l \int_{-\infty}^{\infty} dE f_F(E) D_l(E - E_{l,k_z}) \\ &= \frac{N_L(B)}{\pi} \sum_l \int_{-\infty}^{\infty} dE f_F(E) \int_{\text{B.Z.}} dk_z \delta(E - E_{l,k_z}) \\ &= \frac{eB}{2\pi^2\hbar} \sum_l \int_{E_l(k_z=0)}^{E_F} dE \int_{\text{B.Z.}} dk_z \frac{2\delta(k_z - k_{z,E_l})}{\left| \frac{\partial E_{l,k_z}}{\partial k_z} \right|_{k_z=k_{z,E_l}}} \\ &= \frac{eB}{\pi^2\hbar} \sum_l \int_{E_l(k_z=0)}^{E_F} dE \frac{1}{\left| \frac{\partial E_{l,k_z}}{\partial k_z} \right|_{k_z=k_{z,E_l}}} \\ &= \frac{eB}{\pi^2\hbar} \sum_l \int_0^{k_{F,l}} dk_z \\ &= \frac{eB}{\pi^2\hbar} \sum_l k_{F,l}(B), \end{aligned} \quad (4.3)$$

where $D_l(E)$, $f_F(E)$, and k_F are the density of states, Fermi distribution function, and Fermi wave number respectively. It is shown that the carrier density in the field is given by summing up the Fermi wave numbers in each Landau level.

4.2 Landau quantization in Bismuth carrier

The Landau quantization in the electrons and hole in bismuth strongly depends on the orientation of the magnetic field due to the anisotropy of the effective mass and the effective g -factor. Moreover, the cyclotron energy of the electrons exceeds the Fermi energy (quantum limit) with a moderately low field ($\lesssim 10$ T) because the effective mass is as small as one-thousandth of the bare electron mass in some directions. The effective Hamiltonian of the bismuth electron is equivalent to the Dirac Hamiltonian. These features originate from the strong interaction of isolated two-bands with spin-orbit coupling. The feature of the Dirac electron is the lowest Landau level (LLL) stable against the field. On the other hand, the real LLL in bismuth exhibits field dependence due to the finite inter-band effect [116], and recent magneto-transport experiments in more than 50 T imply that carrier evaporation is induced by this field dependence [40].

4.2.1 Dirac electron in bismuth

Small electron pockets located at the L points in the Brillouin zone (Fig. 4.1b,c). The conduction band at these points is proximate to the valence band with a small gap and isolated from the other bands (Fig. 4.2). The proximity yields a strong inter-band effect and this 2-band system can be well described with Dirac Hamiltonian [56, 57] as shown below (*Sec.3.1.2*).

$$\begin{aligned} \hat{H}_{\text{Wolff}} &= \Delta\beta + i\hbar\mathbf{k} \cdot \left[\sum_i \mathbf{W}_i \beta \alpha_i \right] \\ \alpha_i &= \begin{pmatrix} 0 & \sigma_i \\ \sigma_i & 0 \end{pmatrix} \quad \beta = \begin{pmatrix} I & 0 \\ 0 & -I \end{pmatrix} \end{aligned} \quad (4.4)$$

Δ is a half gap and σ_i is the Pauli matrix. The constant vector \mathbf{W}_i is corresponding to the intensity of band interaction and determines the anisotropy of the masses of electrons. We can easily obtain the quantized energy levels in the magnetic field by substituting $\boldsymbol{\pi} = \hbar\mathbf{k} + e\mathbf{A}$ with the momentum $\hbar\mathbf{k}$ as shown in *Sec.3.2.2* (\mathbf{A} is the vector potential). This operator satisfies a commutation relation ($\boldsymbol{\pi} \times \boldsymbol{\pi} = ie\mathbf{B}$). If

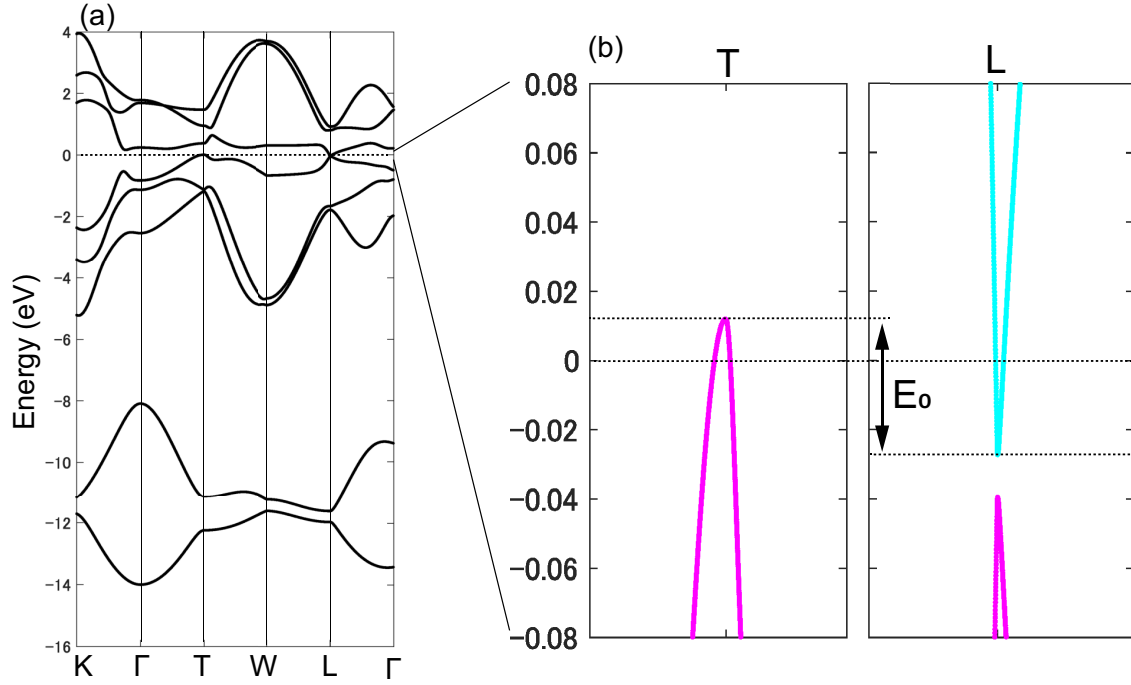


Figure 4.2: (a) Band structure of bismuth crystal calculated by the tight binding model [117]. (b) Energy dispersion round the T and L points in the vicinity of the Fermi energy.

the magnetic field is applied along the z axis, the l -th Landau level of this electron with spin ($s = \pm 1$) is given as

$$E_{l,s}(k_z) = \sqrt{\Delta^2 + 2\Delta [(l + s/2 + 1/2)\hbar\omega_c + \hbar^2 k_z^2 / 2m_z]}. \quad (4.5)$$

The lowest Landau level (LLL) ($l = 0, s = -1$) is stable against the field since the scale of Zeeman splitting is equivalent to the cyclotron energy $\hbar\omega_c$. The electrons in bismuth have strong anisotropy in the effective mass. The cyclotron energy, cyclotron mass, and mass along the field are defined as follows:

$$\hbar\omega_c = \frac{eB}{m_c}, \quad m_c = \sqrt{\frac{\det \hat{m}}{m_z}}, \quad m_z = \mathbf{b} \cdot \hat{m} \cdot \mathbf{b}. \quad (4.6)$$

\hat{m} is 3×3 effective mass tensor and \mathbf{b} is the normalized magnetic field. The effective mass tensors in two of the three electron pockets are given by $\pm 2\pi/3$ rotation of

one tensor ($\hat{m}_{e2,3} = R^{-1}(\pm 2\pi/3) \cdot \hat{m}_{e1} \cdot R(\pm 2\pi/3)$) as we conducted in the mobility tensor.

4.2.2 Extended Dirac model

As shown above, Landau levels with the same total angular momentum $j = l + s/2$ degenerate, and the LLL in the Dirac electron is not shifted by the magnetic field in the Dirac model. On the other hand, finite interaction between the Dirac 2-band and outside bands causes splitting in the degenerated pair in real bismuth crystal [116, 118]. This effect can be described by an additional g -factor denoted with g' [45, 54, 88] and the Landau levels are given as follows:

$$E_{l,s}(k_z) = \sqrt{\Delta^2 + 2\Delta [(l + s/2 + 1/2)\hbar\omega_c + \hbar^2 k_z^2 / 2m_z]} + \frac{sg'\mu_B B}{2}, \quad (4.7)$$

where μ_B is the Bohr magneton. The field dependence of Landau levels is shown in Fig. 4.3. The extension is corresponding to first order perturbation and the edge of the LLL linearly depends on the field. The sign of g' is positive with the field along the bisectrix axis and negative in the binary and trigonal axis. This means the LLLs of the conduction and valence bands cross at a high field in the binary and trigonal axis.

Furthermore, Vecchi *et al.* suggested non-negligible B^2 dependence in LLL [116]. This parabolic term originates from the interaction between LLLs of conduction and valence bands and exhibits anti-crossing behavior when these levels approach each other. Recently, the observation of extra Shubnikov-de Haas oscillation [40, 119] suggested the evacuation of carrier pockets in bismuth. These results imply that the parabolic field-dependence affects the electron transport at more than 40 T. According to the previous research [40, 45, 116], the field dependence of LLL is given in the following form:

$$E_{0,-1}(k_z) = \pm \sqrt{\left(\frac{\hbar^2 k_z^2}{2m_z} - \frac{\tilde{g}'\mu_B B}{2}\right)^2 + (2V\mu_B B)^2}, \quad (4.8)$$

where \tilde{g}' is the modified g' factor [$\tilde{g}' = g'(1 + 2V'|g'|\mu_B B/\Delta)$] and V, V' are parameters related to the interactions between conduction and valence bands. With this

model, the field dependence of the Landau levels and Fermi level are as shown in Fig. 4.4. After the anti-crossing, the LLL of the electron increases drastically and exceeds the Fermi energy. Therefore, one (two) of the three electron pockets are perfectly evacuated at 60 T (40 T) with the field along the binary (bisectrix) axis.

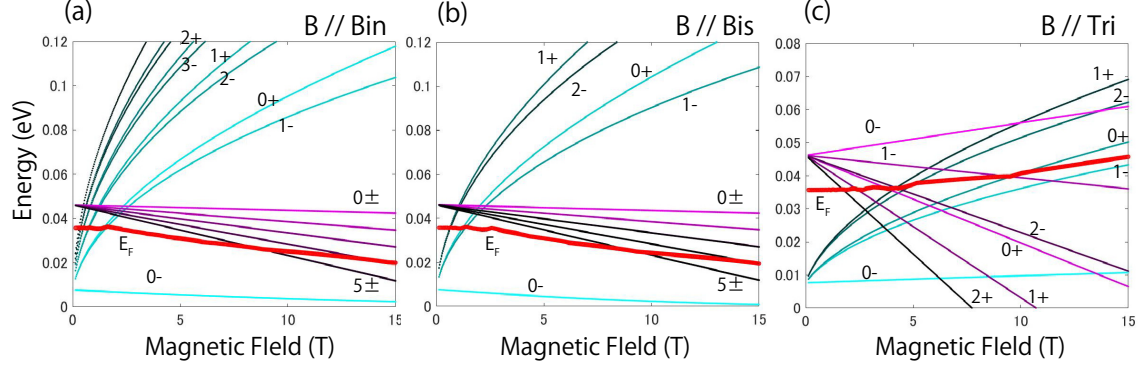


Figure 4.3: Field dependence of the edge of Landau levels and the Fermi level with the field along the (a) binary, (b) bisectrix, and (c) trigonal axis. Cyan and magenta lines indicate the electron and hole levels respectively. Red line indicates the Fermi energy.

4.2.3 Hole in bismuth

The hole pocket in bismuth locates at the T point (Fig. 4.1) and can be well approximated with an anisotropic free particle [94]. The Landau levels of a hole are given by,

$$E_0 + \Delta - E_{n,\sigma}(k_z) = \left(n + \frac{1}{2}\right) \hbar\Omega + G \frac{\sigma \mu_B B}{2} + \frac{\hbar^2 k_z^2}{2M_z}, \quad (4.9)$$

where E_0 is the hybridization energy of conduction band at the L and valence band at T point (Fig. 4.2). Ω, G, M_z are the cyclotron frequency, the effective g -factor, and the effective mass along the field, respectively. The field dependence is shown in Fig. 4.3. The parameters we used for calculating the Landau levels in electron and hole are shown in Table 4.1. One can see that the g -factor in hole carrier is extremely enhanced in the trigonal axis. Recently, it was proved that the bands at the T point

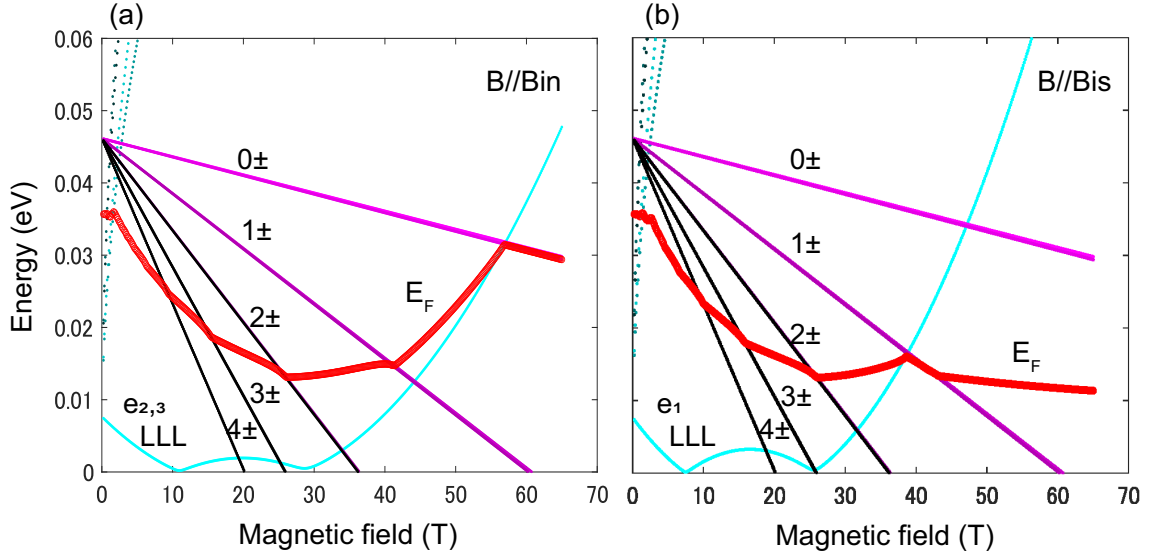


Figure 4.4: Field-dependent Landau levels and Fermi level up to 65 T considering the second-order perturbation of LLL interaction [40, 45]. Cyan and magenta lines indicate the electron and hole levels respectively. Red line indicates the Fermi energy.

are not well isolated from each other, and interaction from other bands far above the Fermi energy remains large, which yields a large and anisotropic spin splitting [98].

4.3 Transverse magnetoresistance

We discuss the angular dependence of transverse magnetoresistance (TMR) in bismuth. TMR is induced by the field perpendicular to the current and the angular dependence generally reflects the anisotropy of the carrier mobility. A recent experiment on bismuth pointed out that the angular dependence shows the vanishing of anisotropy or symmetry breaking at low temperature (Fig. 4.5b) [40, 44, 45, 114], which cannot be explained by conventional semiclassical transport theory. These phenomena arise around the quantum limit, which suggests a limitation of the conventional theory and a necessity of the extension.

According to the experimental setup, we rotated the field in the binary(x)-

Table 4.1: Parameters of effective model [40, 45]. The values of mass m, M are normalized by the mass of bare electron.

electron				
i	xx	yy	zz	yz
m_i	0.00124	0.257	0.00585	-0.0277
g'_i	-3.63	45.6	-7.92	9.20
V_i	0.15	0.15	0.15	0.00
V'_i	-0.0688	-0.0438	-0.0625	0.00

hole			
i	xx	yy	zz
M_i	0.0698	0.0698	0.743
G_i	0.791	0.791	62.6

band gap and hybridization energy

$$2\Delta \quad 15.3 \text{ meV}$$

$$E_0 \quad 38.5 \text{ meV}$$

bisectrix(y) plane with the current along the trigonal(z) axis (Fig. 4.5a) and demonstrated the angle-dependent TMR by calculating (z, z) component of the resistivity tensor ($\hat{\rho} = \hat{\sigma}^{-1}$, where $\hat{\sigma}$ is given by Eq. 4.1). We conducted the calculation at 0.5, 5, 10 T. The electron and hole mobility we used here are shown in Table 4.2. Figure 4.6a-c shows the results of our calculation. Here we plotted the value of magneto-conductance $\sigma_{zz} = \rho_{zz}^{-1}$ to compare with the experiments. We can see the C_6 symmetric star-shaped angular dependence at 0.5 T which reflects the anisotropy of carrier mobility. On the other hand, the anisotropy is suppressed by increasing the field and the angular dependence becomes almost isotropic at 10 T. This behavior qualitatively agrees with the experiments (Fig. 4.5b), and especially, the field range in which the anisotropy vanishes is consistent.

Moreover, the field-dependent evolution in TMR is corresponding to the field dependence of the carrier density at a high field (Fig. 4.6d-f). The carrier densities

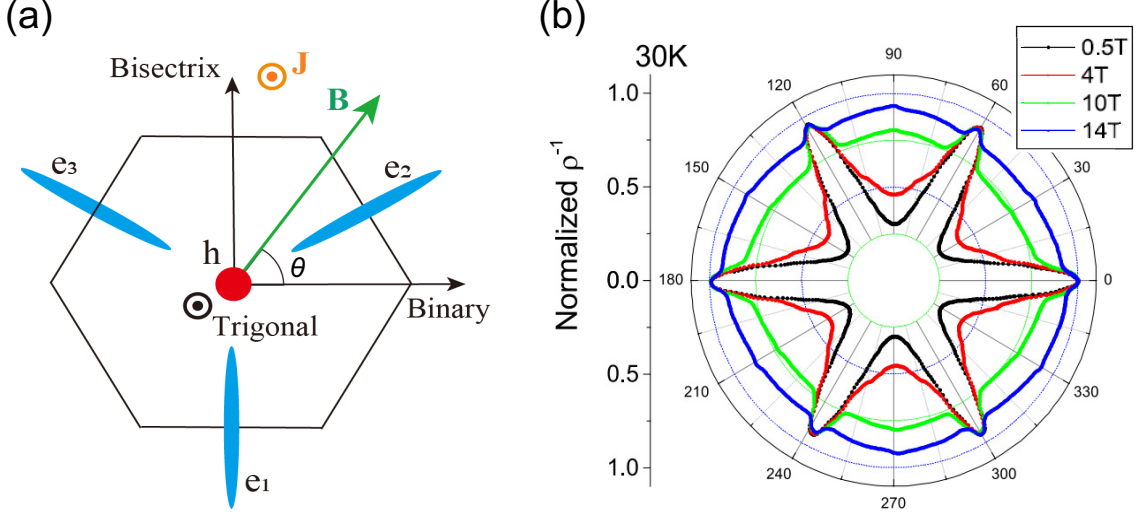


Figure 4.5: (a) Schematic image of TMR in bismuth with rotating field. (b) TMR observed in previous experiments [44, 45].

Table 4.2: Mobility of electron and hole (10^6 cm²/Vs) in bismuth at 4.3 K [115]

i	xx	yy	zz	yz
μ_{ei}	110	3	67	-7.1
μ_{hi}	22	22	3.5	0.0

of electron pockets are isotropic at 0.5 T. At the high fields, carrier densities of the electrons grow in specific directions, which is corresponding to the lowest mobility. The transverse component in the conductivity tensor σ_{zz} of electron pocket e_1 is given in the following form.

$$\begin{aligned} \sigma_{zz} &= \frac{e\mu_{zz}N_{e1}(B)}{B^2(\mu_{xx}\mu_{zz}\cos^2\theta + \mu_{yy}\mu_{zz}\sin^2\theta - \mu_{yz}^2\cos^2\theta) - 1} \\ &\sim \frac{eN_{e1}(B)}{B^2(\mu_{xx}\cos^2\theta + \mu_{yy}\sin^2\theta)} \quad (\mu B \gg 1, \quad \mu_{\text{diag}} \gg \mu_{yz}) \end{aligned} \quad (4.10)$$

One can see that the contribution from the carrier density and mobility are inversely correlated and the denominator is corresponding to the mobility distant by $\pi/2$ from

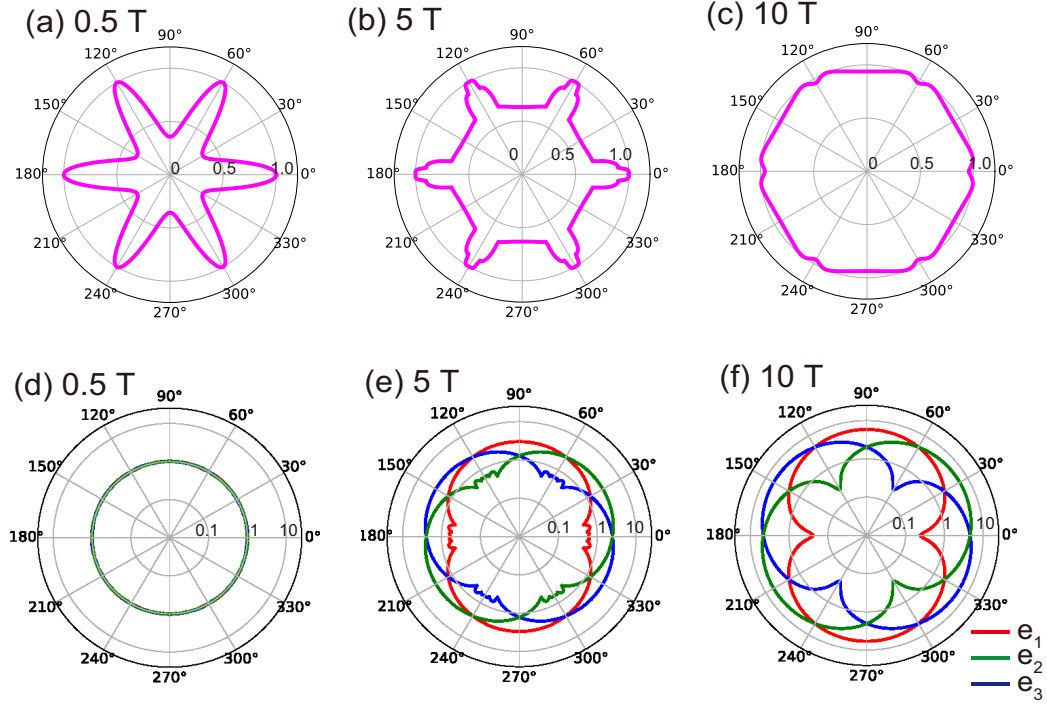


Figure 4.6: Angular dependence of transverse magneto-conductivity ρ_{zz}^{-1} (upper panels) and electron carrier density (lower panels) at (a,d) 0.5 T (b,e) 5 T (c,f) 10 T.

the field. The carrier density grows in the bisectrix axis, which is corresponding to minimum mobility. Hence their contributions cancel each other at high fields. When $B = 10$ T, the anisotropy in the carrier density $N_{\text{Bis}}/N_{\text{Bin}} \sim 21$ is comparable to that of mobility $\mu_{\text{Bin}}/\mu_{\text{Bis}} \sim 37$, which is the origin of isotropic TMR at this field range.

Next, we discuss the origin of the increment in the carrier density in the quantum limit. Considering the charge neutrality, carrier density in semimetals can be modulated in the quantum limit [94]. The essence is the field dependence of the lowest Landau level (LLL). Fig. 4.7a shows the field dependence of the Landau levels in free electrons and Dirac electrons. The LLL in Dirac electron is stable against the field because the spin splitting in the Dirac electron is the same as the cyclotron energy as mentioned in the *Sec.* 4.2.1. After achieving the quantum limit, the Fermi wave

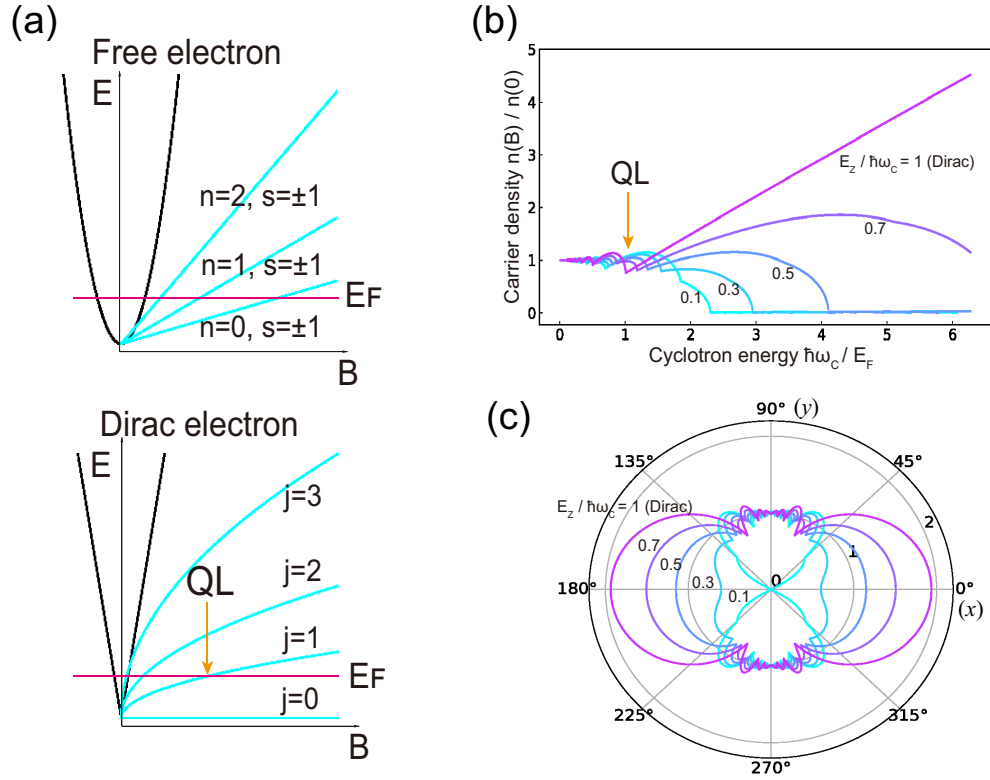


Figure 4.7: (a) Field dependence of Landau levels in free electrons and Dirac electrons. (b) Field dependence of carrier density in two-carrier semimetals. (c) Angular dependence of carrier density in a semimetal with anisotropic Dirac electron.

number is invariant against the field and the density of state increase by the Landau degeneracy $N_L = \frac{eB}{h}$ (Length scale is normalized). According to the Eq. 4.3, the carrier density linearly increases due to the Landau degeneracy.

We demonstrated the field-dependent carrier density in a simple semimetal whose Landau levels are given in the following forms.

$$\epsilon_{n,s} = \left(n + \frac{1}{2} + \frac{s}{2} M_{ZC}^e \right) \hbar\omega_C + \frac{\hbar^2 k_z^2}{2m_z} \quad (\text{electron}) \quad (4.11)$$

$$E_{n,s} = E_{\text{Hyb}} - \left(n + \frac{1}{2} + \frac{s}{2} M_{ZC}^h \right) \hbar\Omega_C - \frac{\hbar^2 k_z^2}{2m_z} \quad (\text{hole}) \quad (4.12)$$

M_{ZC} called *Zeeman-cyclotron ratio* is the ratio of the Zeeman energy to the cyclotron

energy [98], which takes 1 in the Dirac electron and 0 in the free electron. In the calculation, this ratio is varied from 0.1 to 1 in electron and fixed to 10^{-4} in the hole. The mass of the electron is set 1000 times smaller than the hole to realize the quantum limit at lower fields. We calculated the carrier density by the charge neutrality condition. In Fig. 4.7b, we can see drastic changes in carrier density after the quantum limit. The field dependence is clearly correlated to M_{ZC} values and the case $M = 1$ (Dirac electron) shows a linear dependence.

We also plotted the angular dependence of carrier density in anisotropic electrons. We considered an isotropic free hole and ellipsoidal Dirac electron. The electron mass along the y direction is fixed 1/10 times smaller than the x direction. The result is shown in Fig. 4.7c. The angular dependence becomes anisotropic as the field is increased and the direction of growth is perpendicular to the direction of the lightest mass. From Eq. 4.10, we obtained an important suggestion that the anisotropy of TMR in a semimetal with Dirac-type carriers is suppressed by the carrier density at the quantum limit.

In conclusion, semimetals with Dirac-type carriers exhibit anisotropic growth of carrier density in the direction of maximum cyclotron energy, resulting in the suppression of the anisotropy of transverse magnetoresistance at the quantum limit. Dilute Dirac electron systems, such as bismuth, generally have a small mass. In other words, the cyclotron energy is enough large and the quantum limit can be achieved with a moderately low field. Hence it is possible that the same phenomenon is observed in other semimetals with anisotropic Dirac electrons.

4.4 Planar Hall effect

The second mystery in recent research in bismuth is the field dependence of the planar Hall effect (PHE) and anisotropic MR (AMR). When we rotate the magnetic field in the plane of the Hall bar, the angular dependence of longitudinal and Hall resistivity is expected in some materials (Fig. 4.8). The oldest history of these effects dates back to its discovery in 1954 by Goldberg [120]. In the semiclassical viewpoint, this phenomenon arises from the anisotropy of the system. From an early age, this phenomenon has been observed in many varieties of materials including

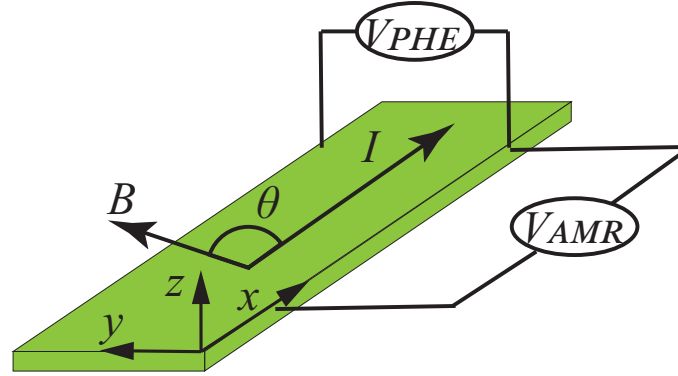


Figure 4.8: Configuration of PHE and AMR measurement.

semiconductors with cubic symmetry [120–123] and ferromagnetic materials [124]. Recently, the quantum-mechanical origins of PHE were repeatedly reported in Dirac and Weyl electron systems. When the magnetic field is applied parallel to the electric field, chiral symmetry in the system is broken resulting in the excitation of electrons with specific chirality (*Chiral anomaly*) [17]. This anomaly increases the chiral carrier concentration and modulates the resistivity. Some theories suggest a negative magnetoresistance [18, 20] and PHE with period π [21, 22]. Hence, one of the largest interests in MR study in materials today is the observation of chiral anomaly [27–35, 125]. Indeed, these phenomena are observed in real materials and regarded as evidence of non-trivial Berry curvature or chiral anomaly. On the other hand, PHE is not a special phenomenon for general electron systems as referred to the history of this effect. Very recent experiments suggested a possibility of the trivial (orbital) origin of the PHE [36–39]. Trivial PHE is explained in the framework of semiclassical transport theory. The problem today is how we distinguish the origin of PHE, while it is not easy. One honest way to analyze the observed PHE is to discuss whether the results can be explained by semiclassical models.

In bismuth, a recent experiment suggested some unexpected effect that causes the field- and angle-dependence in PHE and AMR [35]. They carefully analyzed the observation with multiple ellipsoidal models and this model successfully agreed with the angle dependence at low field. However, the PHE and AMR at the high field

cannot have been explained. The angle-dependence at low field contains the main sine and cosine curve with the period π and the second harmonic wave (Fig. 4.9b). Increasing the field, the second harmonic component is suppressed and the amplitude of the main curve is enhanced (Fig. 4.9c). This enhancement is consistent with the expected from the chiral anomaly [21, 22], which is the reason they suggested some strange effect in the PHE of bismuth.

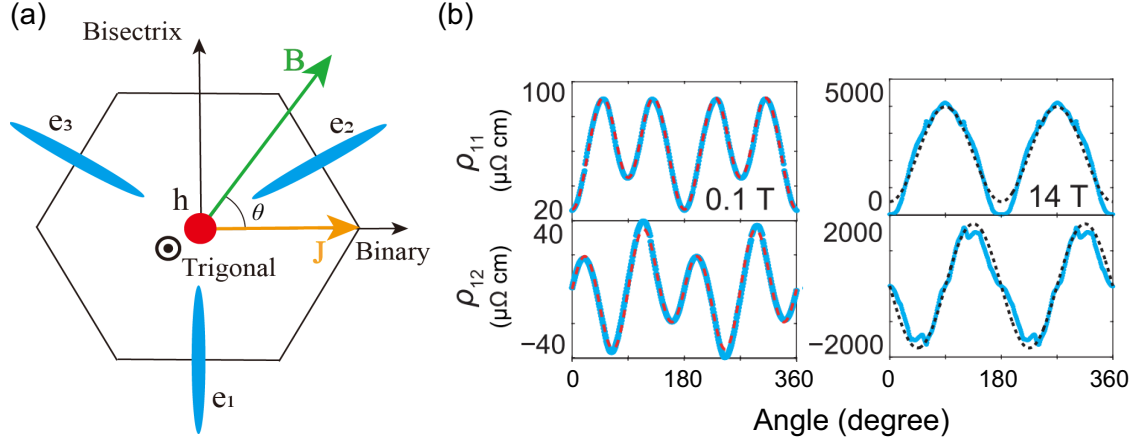


Figure 4.9: (a) Configuration of PHE and AMR in bismuth. (b) Experimental results for PHE and AMR [35]. Upper panels show the angular dependence of AMR and lower panels are the PHE.

Figure 4.9a shows the configurations of our calculation for PHE and AMR in bismuth, which is consistent with the experiment [35]. Rotating the magnetic field in the plane of Hall bar, the PHE is calculated by the Hall resistivity ρ_{xy} and the AMR is the longitudinal resistivity ρ_{xx} with the current along the x direction. In this section, we first want to show that the PHE and AMR with the period π naturally arise in general multiple carrier system. Bismuth is a typical multiple carrier system and the angular dependence becomes more complicated due to its anisotropy. Moreover, the thickness-dependent carrier mobility and field-dependent carrier concentration can qualitatively modulate the PHE and AMR signals. In the case of bismuth thin film, the charge neutrality in carriers is violated so remarkably that we cannot neglect it in our calculation. Our results well agree with the experiments, and we found that

the angular dependence can be changeable due to the value of mobility, the strength of the field, and the compensation condition of the charge. Moreover, we found that the carrier density in Dirac electrons increases after achieving the quantum limit resulting in charge compensation of the carriers.

4.4.1 PHE and AMR in isotropic multi-carrier metals

In this section, we show that the PHE and AMR can be originated from multiple carrier transport. First, we note that single carrier systems do not exhibit the angular dependence in PHE and AMR in the semiclassical framework ($\rho_{PHE} = 0$, $\rho_{AMR} = \rho_0$). The situation critically changes just by adding another carrier with different mobility. With the aid of the multiple carrier method in Eq. 2.19, we can easily derive the angular dependence in isotropic 2-carrier systems. We rotated the field in the x - y plane and this effect was demonstrated by calculating the (x, y) and (x, x) components of resistivity tensor respectively. The result is shown below.

$$\rho_{PHE} = \rho_{xy} = -\Delta\rho_{\text{diff}} \sin\theta \cos\theta, \quad (4.13)$$

$$\rho_{AMR} = \rho_{xx} = \rho_{\perp} - \Delta\rho_{\text{diff}} \cos^2\theta. \quad (4.14)$$

$$\Delta\rho_{\text{diff}} = \rho_{\perp} - \rho_{\parallel} = \frac{1}{en} \frac{(\mu_1 - \mu_2)^2 \mu_1 \mu_2 B^2}{(\mu_1 + \mu_2)(4(\mu_1 \mu_2 B)^2 + (\mu_1 + \mu_2)^2)}$$

θ is the angle of the magnetic field measured from the x axis and n is the carrier density. $\rho_{\parallel} = \rho_{11}|_{\theta=\pi/2}$ and $\rho_{\perp} = \rho_{11}|_{\theta=0}$ are corresponding to the longitudinal MR (LMR) and TMR respectively. The angular dependences are simple sine and cosine curves with a period π . This functional form is the same as what is expected from the chiral anomaly [21, 22]. We can see three specific properties about the amplitude $\Delta\rho_{\text{diff}}$. First, it vanishes when these two carriers are equivalent $\mu_1 = \mu_2$. Second, it saturates at a high field limit. Third, the value is greater with smaller mobility (Fig. 4.10a).

4.4.2 Isotropic semimetals

When the charge of carriers is compensated, the semimetals with an isotropic electron and an isotropic hole give the PHE and AMR in the same form as Eq. 4.13,

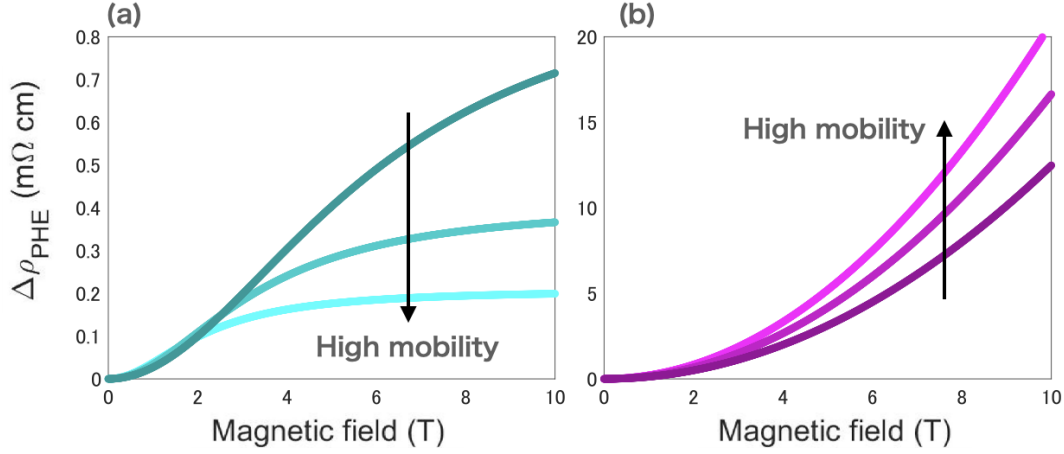


Figure 4.10: Field dependence of the PHE amplitude in (a) isotropic 2-carrier metals and (b) compensated 2-carrier semimetals with isotropic electron and hole. One of the mobility μ_1 is varied in 1.0, 0.8, 0.6 T^{-1} and the ratio of two mobilities is fixed to 0.5. The carrier density n is 10^{18} cm^{-3} .

4.14. The amplitude of this angular dependence is given as follows:

$$\Delta\rho_{\text{diff}} = \rho_{\perp} - \rho_{\parallel} = \frac{1}{en} \frac{\mu_1 \mu_2 B^2}{\mu_1 + \mu_2} \quad (4.15)$$

μ_1, μ_2 are the mobilities of the electron and hole respectively. The amplitude does not be zero even when the two carriers have the same mobility. Moreover, the amplitude increases with the B^2 characteristic and does not saturate. This is the consequence of charge neutrality because of the TMR in compensated semimetal parabolic and non-saturating field dependence. The most contrasting feature is that the amplitude of PHE increases with increasing mobility is as shown in Fig. 4.10b. When the charge neutrality is violated, the amplitude is

$$\Delta\rho_{\text{diff}} = \frac{\mu_1 \mu_2 n_1 n_2 (\mu_1 + \mu_2)^2 B^2}{e (n_1 \mu_1 + n_2 \mu_2) (\mu_1^2 \mu_2^2 (n_1 - n_2)^2 B^2 + (n_1 \mu_1 + n_2 \mu_2)^2)}. \quad (4.16)$$

n_1, n_2 are the carrier densities of electron and hole. In this case, this amplitude saturates at a high field and becomes greater with lower mobility like the metals.

The detail of calculation in 2-carrier model is shown in *Appendix A*. We further

showed that the angle-dependence in PHE and AMR holds in isotropic n -carrier metals ($n \geq 2$) and semimetals.

4.4.3 PHE in Bismuth: compensated

Here, we discuss the case of bismuth. This system is a multiple carrier system, hence we can expect that both PHE and AMR have angular dependence. Due to the anisotropy, its functional form becomes more complicated. According to the setup in the experiment, the magnetic field was rotated in the x - y plane, and PHE and AMR were calculated as the (x, y) and (x, x) components of resistivity tensor respectively. The carrier concentration in the field was calculated by the charge neutrality condition in Eq. 4.2.

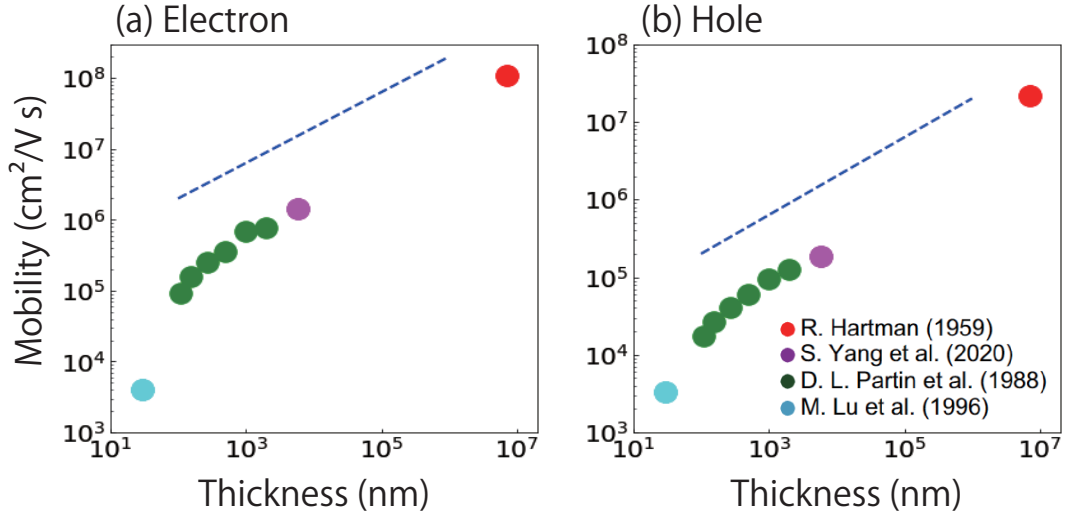


Figure 4.11: Thickness dependence of (a) electron and (b) hole mobility in bismuth [35, 115, 126, 127]. The data from *Hartman* and *Yang et al.* are the maximum components in the mobility tensor. Broken lines indicate \sqrt{t} dependence.

We demonstrate the PHE and AMR in bismuth with bulk and film mobility. The carrier mobility in bismuth strongly depends on the size of the crystals. We plotted the thickness (t) dependence of the mobility of electron and hole in Fig. 4.11. We

can see the mobility increase with the thickness, and the thickness dependence is almost \sqrt{t} in the thicker range ($t \gtrsim 1\mu\text{m}$). Since the mean free path in bismuth is quite long ($l \sim 0.3\text{mm}$) [15], the effective mean free path in the crystals is determined by the size of the crystal when the size is smaller than the path. In this size range, the carrier lifetime increases with increasing the film thickness and the thickness dependence of mobility may come up.

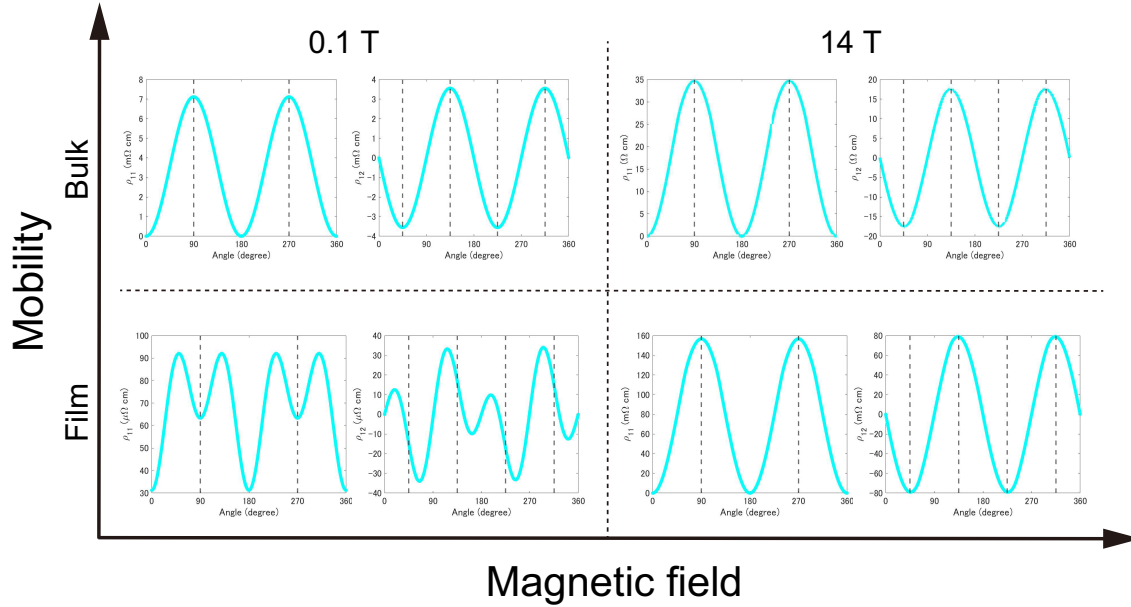


Figure 4.12: Field- and mobility-dependence of PHE and AMR in bismuth.

Our calculation was conducted with four different conditions: film in the low field, film in the high field, bulk in the low field, and bulk in the high field. The mobility in bulk and film were from the low-temperature experiments by R. Hartman [115] and from S.-Y. Yang [35] respectively. Fig. 4.12 shows the results. The angular dependence with a period shorter than π is present in the case with low field and low mobility, and this component vanishes with high field or higher mobility. The angular dependence is identical to the cases of isotropic metals and semimetals as shown in Eq. 4.13 when μ or B is large. These values are always present in coupled in the magnetoresistivity tensor, hence the behavior of PHE and AMR can be changed by

the value of μB . We can say that general materials with a large mean free path and large mobility can exhibit different angular periodicity depending on the thicknesses or field.

4.4.4 PHE in Bismuth thin film: uncompensated

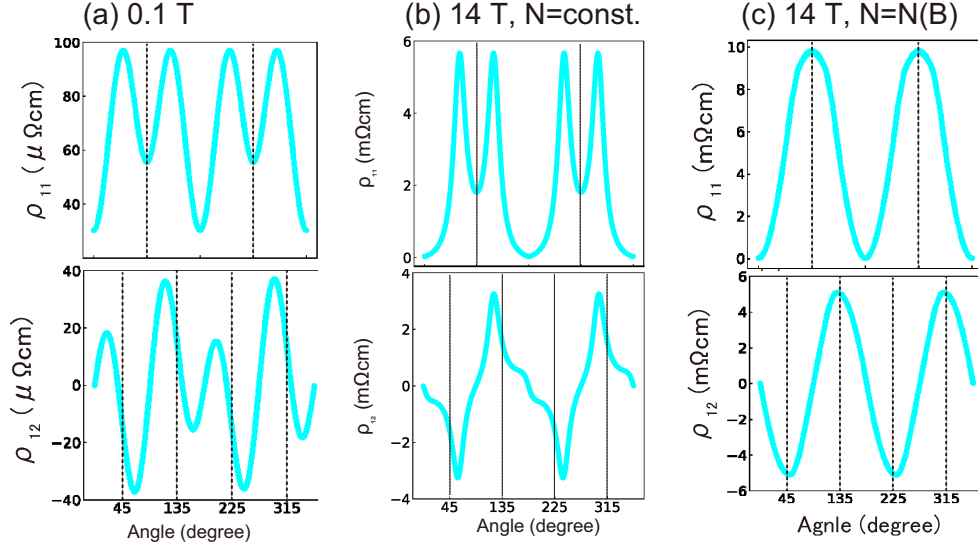


Figure 4.13: PHE and AMR in bismuth thin film. (a) low field and high field with (b) constant carrier density and (c) field-dependent density.

We also discuss the case that the charge neutrality is violated. In real bismuth thin film ($5.3 \mu\text{m}$), the charge deviation between electron and hole is remarkably large [35]. According to the experimental condition, the deviation of electron density and hole density at zero fields are fixed to be 26.5 % of the electron density. If we do not consider the field-dependent carrier density, the angular dependence of PHE and AMR does not change qualitatively and the amplitude saturates at high field (Fig. 4.13b). Especially, the shorter-period component remains even at high fields. This field-dependent characteristic does not agree with the experiment, which indicates the vanishing of shorter components and perfect sine- and cosine-like angular dependence at high field. If the charge of carrier is compensated, this qualitative shift at high

field is natural as we have seen in Fig. 4.12. It is implied that the key to this change is the degree of violation of charge neutrality.

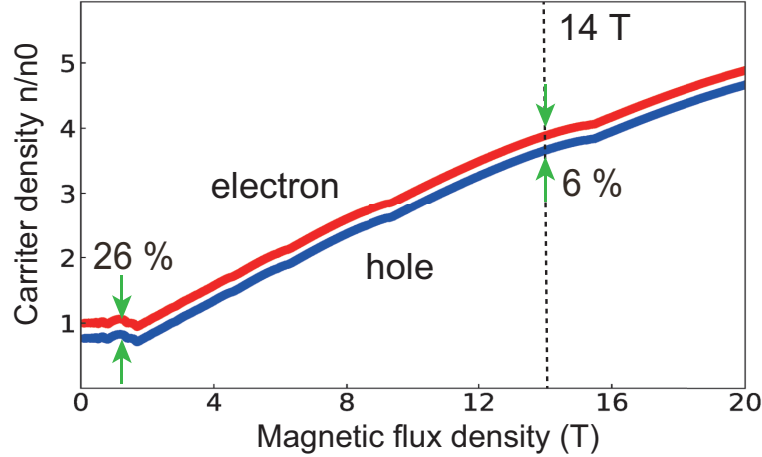


Figure 4.14: Field-dependence of electron and hole density with the field along with Binary direction.

Next, we assume the field-dependent carrier densities with charge imbalance. It is also assumed that the imbalance is originated from charged impurity and the difference between two carrier densities is constant with any fields ($N_e(B) - N_h(B) = N_e(0) - N_h(0)$). In this case, the periodic characteristics changes at a high field (Fig. 4.13c). Some electron pockets exceed the quantum limit at 14 T, hence the carrier density is drastically modulated.

Figure 4.14 shows the field dependence of carrier density with the field along the binary axis calculated with the constant charge difference. At the low field, the charge difference is about 27% of the electron carrier. On the other hand, both carriers increase after achieving the quantum limit. The ratio of impurity charge decreases because of the enhancement of total carrier density and it is only 6% at 14 T.

In summary, the angular dependence of PHE and AMR in bismuth thin film shows periodic characteristics with both π and shorter ($\pi/2$) period at low field and they turn to be a simple sine and cosine curve with period π at high field. We

pointed out that this qualitative change is a natural consequence when the carriers are compensated. It was also found that the field-dependent carrier increment at the quantum limit suppresses the degree of the charge imbalance in real bismuth thin films.

4.5 TMR far beyond the quantum limit

The qualitative shift in angular-dependent TMR, PHE, and AMR across the quantum limit was well explained by considering field dependence of carrier density. On the other hand, the third mystery remains in the quantitative difference between the theory and experiments far beyond the quantum limit ($B \gtrsim 10$ T) [40]. The experimental MR in this field range is relatively small than the theoretical expectation, and it shows a sudden drop at $60 T$ ($40 T$) in binary (bisectrix) direction. Figure 4.15a,b show that the theoretical value is estimated more than 100 times the observed value at 10 T both in the binary and bisectrix direction even with the field-dependent carrier density. Moreover, our model cannot explain the non-monotonic behavior at $60 T$ and $40 T$. This implies something missed in our model. In compensated semimetals, the TMR generally takes a larger value with higher mobility. Hence, one possible origin of the extraordinary MR is that the mobility is suppressed at high fields. We demonstrated TMR assuming several types of field dependence of the carrier mobility in bismuth (electron: $\hat{\mu}_i = \hat{\mu}_{i0}/(1 + \gamma_{ei}|B|^p)$, hole: $\hat{\nu}_i = \hat{\nu}_{i0}/(1 + \gamma_h|B|^p)$, $p = 1, 2, \dots$), where γ_{ei} and γ_h are fitting parameters. Furthermore, we employed the quadratic model of the lowest Landau level given in Eq. 4.8 and considered the carrier evacuation at an extremely high field. Figure 4.15b,c and e,f show the results of fitting in the case $p = 1, 2$ respectively. We can see that $p = 1$ well fits the experiments in both directions. Furthermore, the dip structure at 60 T ($40 T$) in the binary (bisectrix) direction, which is corresponding to the carrier evacuation, is well simulated. This implies that the scattering rate increases linearly with the magnetic field. Moreover, we found a relationship between the mass of the electron and the parameter γ_{ei} in electron ($\gamma_{ei} \propto 1/m_{ezi}$). This result means that the mobility of electron with smallest m_z , heaviest cyclotron mass in other words, is suppressed most drastically in three electron pockets.

4.6 Field-dependent mobility

The B^{-1} field dependence of mobility is previously reported in dilute metal SrTiO_3 [64]. In metals, this type of field dependence yields linear MR. According to the result of fitting, the field dependence of mobility in bismuth appears at $B < 10^{-1}$ T for electron and $B < 1$ T for the hole in both binary and bisectrix axis (Fig. 4.16). These ranges are lower than the quantum limit region. Theoretical studies based on quantum mechanics showed that the linear MR are expected in the quantum limit [50,51,128]. These theories are based on the scattering by an impurity described with a delta function. Kahn pointed that the scattering rate with this type of impurity becomes anisotropic in the quantum limit [128].

On the other hand, many real materials exhibiting linear MR have dilute carrier concentration [44,45,47], small Fermi energy in other words. This implies that the spatial dependence of impurity potential is not negligible due to imperfect Coulomb screening of charged impurities. Mahan demonstrated the scattering by Gaussian impurity potential [129]. Mahan also pointed that the scattering rate has field dependence at lower fields than the quantum limit, which results in field-dependent mobility. Moreover, the scattering rate becomes anisotropic and the difference between in-plane and out-of-plane scattering grows with the field increment. In the result of bismuth, the field dependence of mobility also has strong anisotropy, and the carrier concentration is quite small $\sim 10^{-17} \text{ cm}^{-3}$. The origin of the field dependence is still an open question, some anisotropic scattering by position-dependent potential in the magnetic field is a possible candidate.

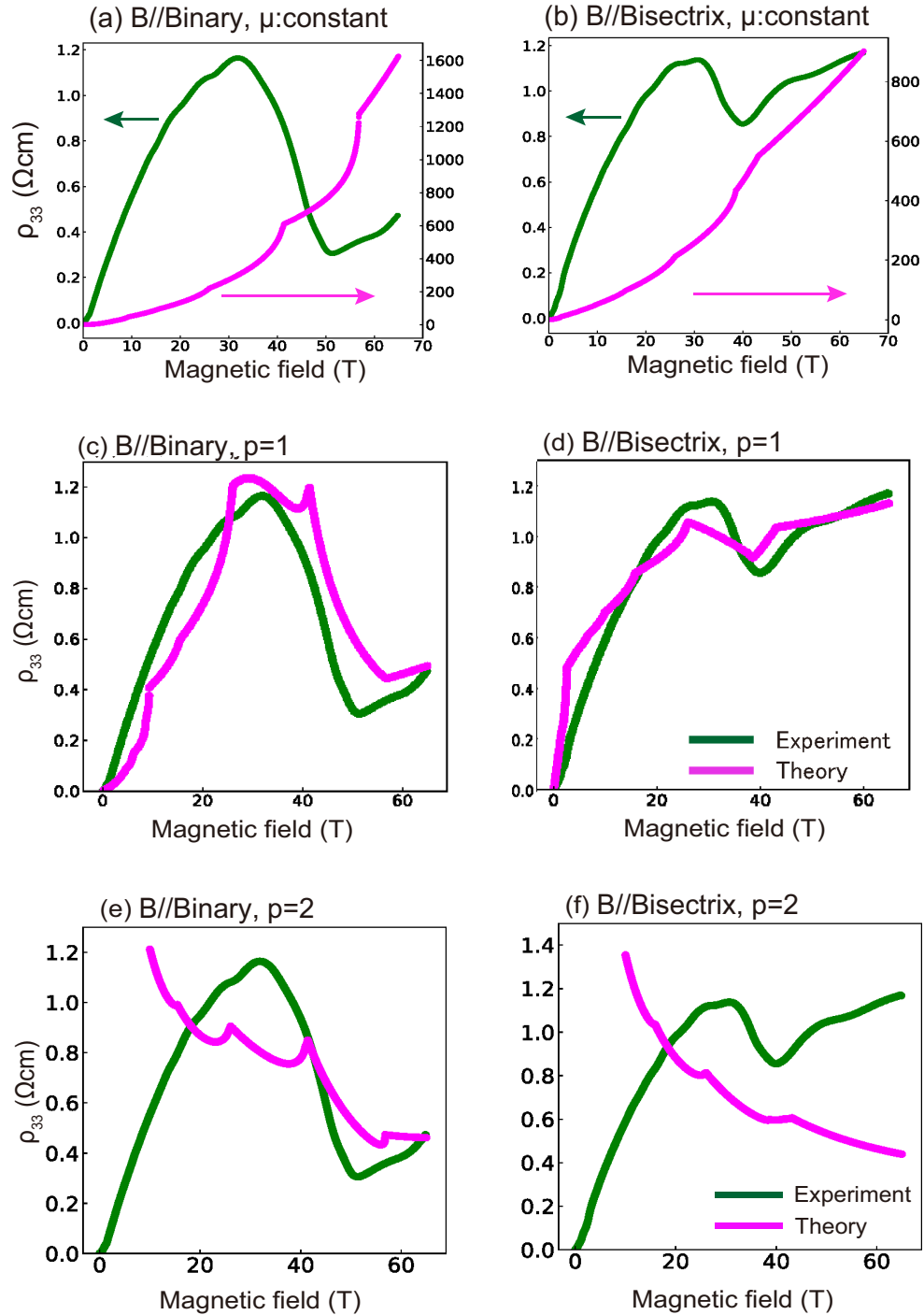


Figure 4.15: Purple line: simulated TMR in bismuth with (a,b) $p = 0$, (c,d) $p = 1$, and (e,f) $p = 2$. Left panels show the results in the Binary direction and right panels are the results in the Bisectrix direction. Green lines shows the experimental data.

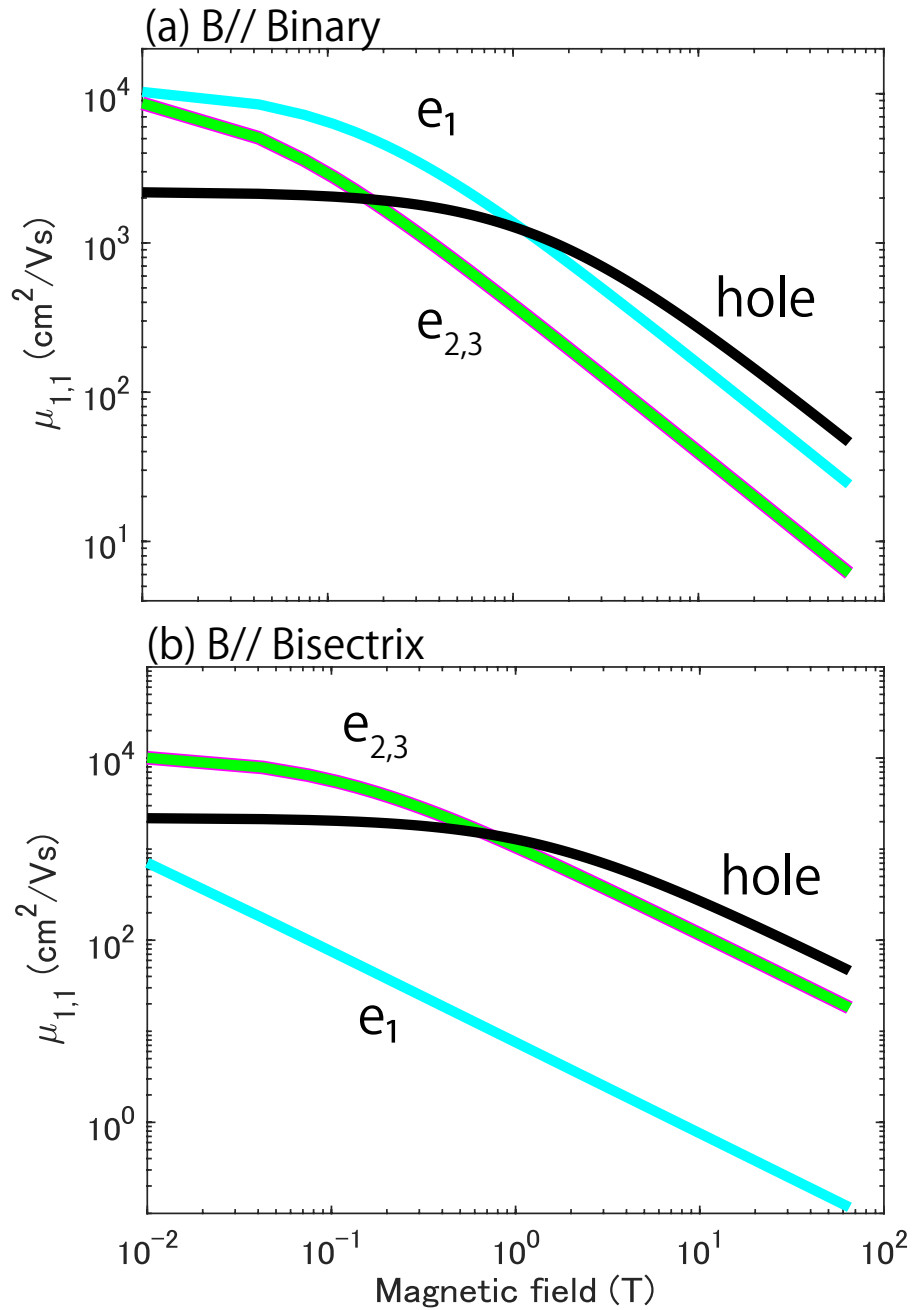


Figure 4.16: Field dependence of mobility in Bismuth carrier with field along (a) Binary and (b) Bisectrix axis.

Chapter 5

MR in Weyl electron systems

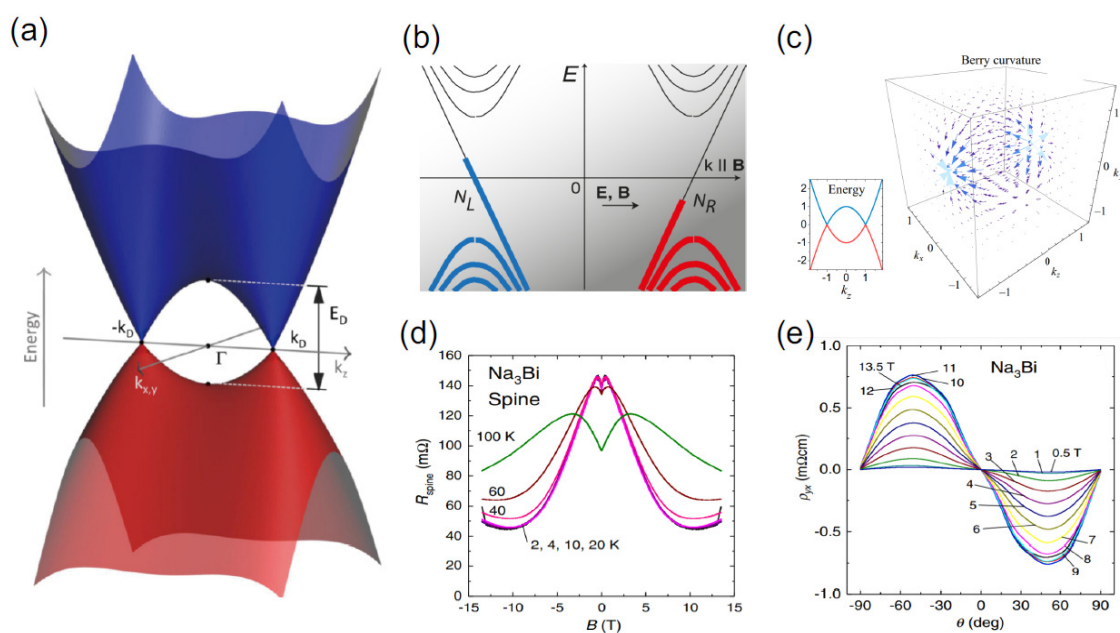


Figure 5.1: (a) Typical band structure in Weyl electron systems with degenerated nodes (Weyl semimetals): an example of Γ point in Cd_3As_2 [130]. The schematic images of (b) Chiral anomaly [28] and (c) Berry curvature [131] in Weyl semimetals. Observed (d) negative LMR and (e) PHE in Na_3Bi [28].

Weyl electron systems in solids are characterized by the special band structure. They have degenerated nodes (Fig. 5.1a) or nodal lines [132] in their Brillouin zone, which yields non-trivial Berry curvature (Fig. 5.1c) [16, 131]. Electric current and magnetic field can couple through this curvature resulting in the non-trivial magneto-transport phenomena such as negative longitudinal MR (LMR) and PHE with the period π (Fig. 5.1d,e) [18–22]. The core mechanism of them is the excitation of the chiral carriers by the magnetic field (Fig. 5.1b) [17]. This is called chiral anomaly. Experiments followed these predictions recently and observation of the anomaly in materials has been one of the central issues in Weyl electron physics [26–35]. Magneto-transport is regarded to be a promising method to identify the anomaly.

However, PHE alone cannot prove the existence of the anomaly as we showed in the former chapter. Some experiments suggested PHE from a trivial origin [37] and necessity of negative LMR for proving the chiral anomaly [36–39]. Conventional semiclassical theory without Berry curvature cannot give an explanation for the negative MR so far. On the other hand, the fine structure of the Fermi surface has been rarely considered. Fermi surfaces cannot be generally approximated by the conventional multi-carrier model because the electron velocity and the effective mass differ from point to point on the surfaces. The consequences of considering the local structure are still to be explored. While the MR calculation method based on the first principle has been presented and the fine orbital structure in the magnetic field gets started to be discussed these days [58, 67, 68], the local effective mass has not been discussed intensively.

The semiclassical theory extended to the arbitrary dispersion (Eq. 2.3) yields a new point of view in the magnetoresistance by taking the local effective mass into account. Especially, this suggests a new origin of negative magnetoresistance. In this chapter, we demonstrate the magnetoresistance of the Weyl electron system and show that the negative magnetoresistance can be observed due to the off-diagonal components of the local effective mass tensor on the Fermi surface. We also found that the PHE from orbital origin exhibits specific temperature dependence. A dip structure in the temperature dependence of PHE amplitude is corresponding to the Fermi energy measured from the Weyl point.

5.1 Fermi surface in Weyl electron systems

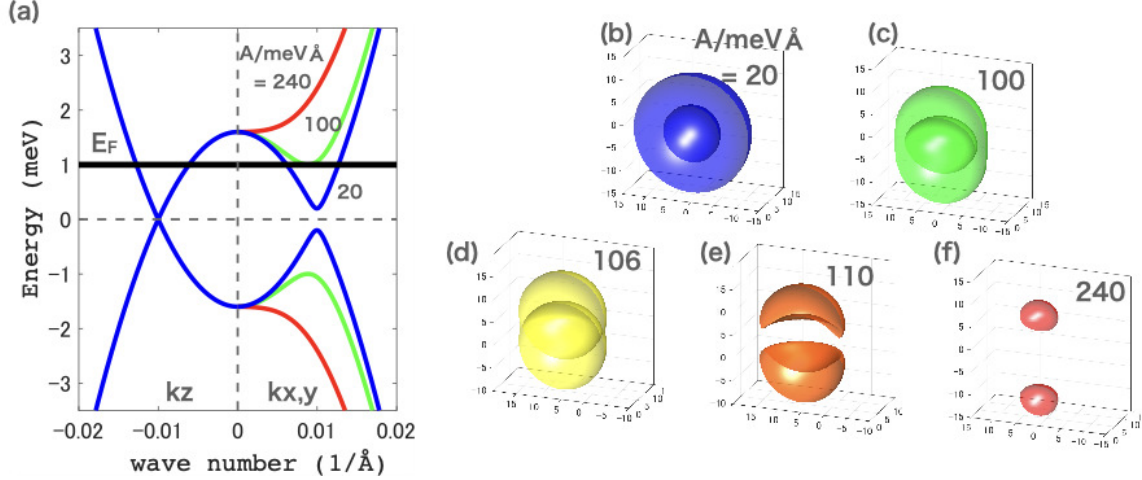


Figure 5.2: (a) Energy dispersion of the Weyl electron model and Fermi surfaces (b-d) before and (e,f) after the Lifshitz transition. $M = 16 \text{ eV}\text{\AA}^2$, $k_w = 0.01 \text{ \AA}^{-1}$

We employ a minimal model for Weyl electron with the symmetry is broken in z direction [107, 131]. The Hamiltonian is given as

$$\hat{H} = A(k_x\sigma_x + k_y\sigma_y) + M(k_w^2 - k^2)\sigma_z. \quad (5.1)$$

σ_i is the Pauli matrices. This model is corresponding to the Γ point of Cd_3As_2 [87] and given by the $k \cdot p$ method (Kane model) in strongly interacted s and p orbital bands with single spin (*Sec.* 3.3.1). The energy eigenvalues of this Hamiltonian are

$$E = \pm \sqrt{M(k^2 - k_w^2)^2 + A(k_x^2 + k_y^2)}. \quad (5.2)$$

There is a pair of degenerated points in $\mathbf{k} = (0, 0, \pm k_w)$ called *Weyl points*. The parameter A corresponds to the intensity of band interaction, and this value determines the anisotropy in this system. When we fix the Fermi energy deviated from the Weyl point, the Fermi surfaces appear, and its shape varies according to the value of this parameter (Fig. 5.2). The Fermi surfaces consist of an isotropic electron surface

covering an isotropic hole surface with enough small A . Increasing this parameter, the electron surface shrinks along the equator. When the Lifshitz transition occurs in the x, y direction, the surfaces are broken into two islands. With further large A , the pair of surfaces is almost ellipsoidal.

5.2 Magnetoresistance

Magnetoresistance in the Weyl electron system is calculated with the semiclassical method in Eq. 2.3. We set $M = 16 \text{ eV}\text{\AA}^2$, $k_w = 0.01 \text{ \AA}^{-1}$, $\tau = 1 \text{ ps}$, and $T = 0.2 \text{ K}$ in the following calculation. We fixed the magnetic field along the x axis. The transverse and longitudinal magnetoresistance are calculated as the diagonal components of resistivity tensor ρ_{yy} , ρ_{xx} respectively. The field-dependence in TMR and LMR with various A are shown in Fig. 5.3. When A is small enough, TMR and relatively small LMR are estimated and their signs are both positive. On the other hand, we can see that both MR turn to negative with large A . Although the MR behavior with small A is expected by the conventional multi-carrier model, it is difficult to explain the negative MR in the twin ellipsoidal Fermi surfaces with large A .

We note that the negative MR shown here definitely originates from semiclassical orbitals on the Fermi surfaces because our calculation did not include any terms from Berry curvature. Moreover, our result presents a negative TMR, which has never been suggested in Berry-curvature-based physics. We can say that the semiclassical theory can present negative MR regardless of longitudinal or transverse ones.

5.2.1 The origin of negative MR

Next, we search the origin of the negative MR. When we set the magnetic field along the x axis, the longitudinal and transverse components of the magnetoresistivity tensor are written as follows.

$$\rho_{\text{LMR}} = \frac{1}{\sigma_{xx}} \quad (5.3)$$

$$\rho_{\text{TMR}} = \frac{\sigma_{zz}}{\sigma_{yy}\sigma_{zz} - \sigma_{yz}\sigma_{zy}} \quad (5.4)$$

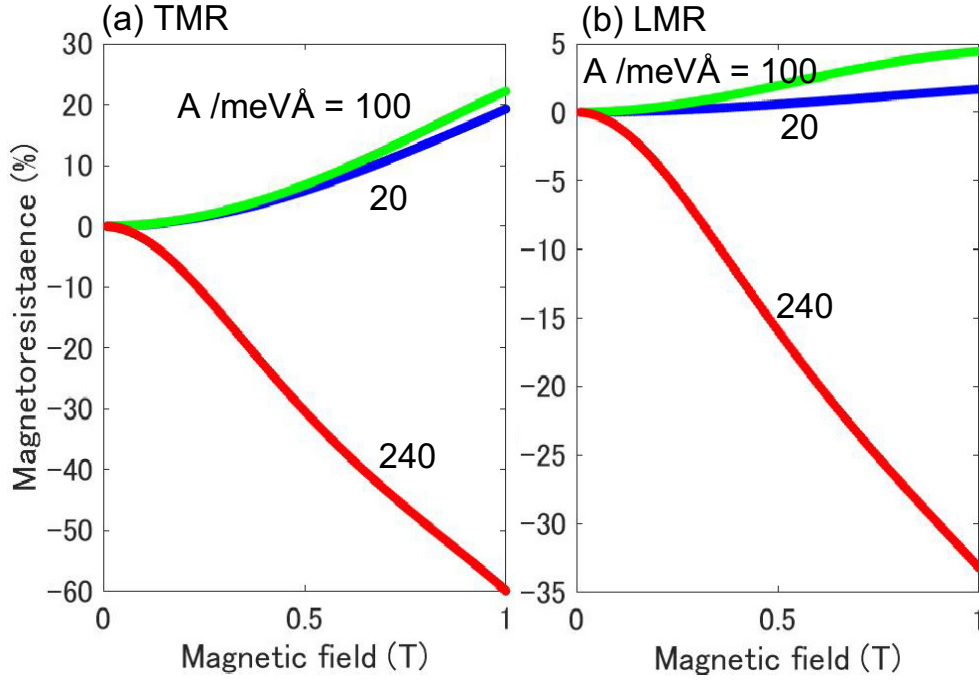


Figure 5.3: (a) TMR and (b) LMR in Weyl electron calculated from the dispersion in Eq. 5.2.

We ignored terms that vanish through the integration due to the symmetry. Each component of conductivity tensor σ_{ij} calculated by Eq. 2.3 can be expanded up to the second-order of the field as shown below [133].

$$\sigma_{xx} = \sigma_{x0} - e^4 \tau^3 \langle ((\alpha_{xz} \alpha_{yy} - \alpha_{xy} \alpha_{yz}) v_z + (\alpha_{xy} \alpha_{zz} - \alpha_{xz} \alpha_{zy}) v_y) v_x \rangle B^2 + O(B^4) \quad (5.5)$$

$$\sigma_{yy} = \sigma_{y0} - e^4 \tau^3 \langle (\alpha_{yy} \alpha_{zz} - \alpha_{yz}^2) v_y^2 \rangle B^2 + O(B^4) \quad (5.6)$$

$$\sigma_{zz} = \sigma_{z0} - e^4 \tau^3 \langle (\alpha_{yy} \alpha_{zz} - \alpha_{yz}^2) v_z^2 \rangle B^2 + O(B^4) \quad (5.7)$$

$$\sigma_{yz} = -e^3 \tau^2 \langle \alpha_{yz} v_z v_y - \alpha_{zz} v_y \rangle B + O(B^3) \quad (5.8)$$

$$\sigma_{i0} = e^2 \tau \langle v_i^2 \rangle$$

The operation $\langle \dots \rangle$ is the integration in the vicinity of Fermi surface shown in Eq. 2.3, and σ_{zy} is given by inverting the sign of σ_{yz} according to the Onsager's relations.

Furthermore, we can expand the resistivities in Eq. 5.3 and Eq. 5.4 up to second-order after substituting the extended conductivities. The results are

$$\rho_{\text{LMR}} = \rho_{x0} + \rho^{(2)} B^2 + O(B^4), \quad (5.9)$$

$$\rho_{\text{TMR}} = \rho_{y0} + (\rho_{\text{Gauss}} + \rho_{\text{Hall}}) B^2 + O(B^4), \quad (5.10)$$

$$\rho^{(2)} = \rho_{x0}^2 e^4 \tau^3 \langle (\alpha_{xz} \alpha_{yy} - \alpha_{xy} \alpha_{yz}) v_z + (\alpha_{xy} \alpha_{zz} - \alpha_{xz} \alpha_{zy}) v_y \rangle v_x, \quad (5.11)$$

$$\rho_{\text{Gauss}} = \rho_{y0}^2 e^4 \tau^3 \langle (\alpha_{yy} \alpha_{zz} - \alpha_{yz}^2) v_y^2 \rangle, \quad (5.12)$$

$$\rho_{\text{Hall}} = -\rho_{y0}^2 \rho_{z0} e^6 \tau^4 \langle \alpha_{yz} v_z v_y - \alpha_{zz} v_y^2 \rangle^2, \quad (5.13)$$

$$\rho_{i0} = \frac{1}{\sigma_{i0}}.$$

The coefficients $\rho^{(2)}$, ρ_{Gauss} , ρ_{Hall} determine the sign of magnetoresistance in weak fields. $\alpha_{yy} \alpha_{zz} - \alpha_{yz}^2$ is known as *Gaussian curvature* on manifolds (Fermi surface) and $\langle \alpha_{yz} v_z v_y - \alpha_{zz} v_y^2 \rangle$ is proportional to the Hall conductivity σ_{yz} [134]. We examine the relation between A and these coefficients. The results are shown in Fig. 5.4a-d. (a) The LMR coefficient $\rho^{(2)}$ drastically changes after the Lifshitz transition and the sign is inverted at a specific A . All the terms in $\rho^{(2)}$ include the off-diagonal components of an inverse mass tensor. We found that the terms with a pair of diagonal and off-diagonal components $\alpha_{ii} \alpha_{jk}$ are numerically dominant with large A and determine the sign of the coefficient (Fig. 5.4b). In the two TMR coefficients: ρ_{Gauss} and ρ_{Hall} , the contribution from the Gaussian curvature is positive in all the range of A and dominant before the Lifshitz transition. On the other hand, the Hall conductivity negatively contributes to the coefficient and drastically increases after the transition. The main term switches to the Hall conductivity after the transition resulting in the sign inversion with large A (Fig. 5.4c,d).

5.2.2 Off-diagonal effective mass

According to the results in Fig. 5.4, the sign inversions in LMR and TMR happen at near points ($A \sim 140 \text{ meV}\text{\AA}$). One can find that the LMR coefficient in Eq. 5.11 have two types of term: $\alpha_{ii} \alpha_{jk} v_j v_k$ and $\alpha_{ij} \alpha_{jk} v_i v_k$ ($i \neq j, j \neq k$). We mapped these values in the plane of k -space in Fig. 5.5a-f. The $\alpha_{ii} \alpha_{jk} v_j v_k$ value has singular characteristics at the Weyl points. When A is large, this value becomes large and

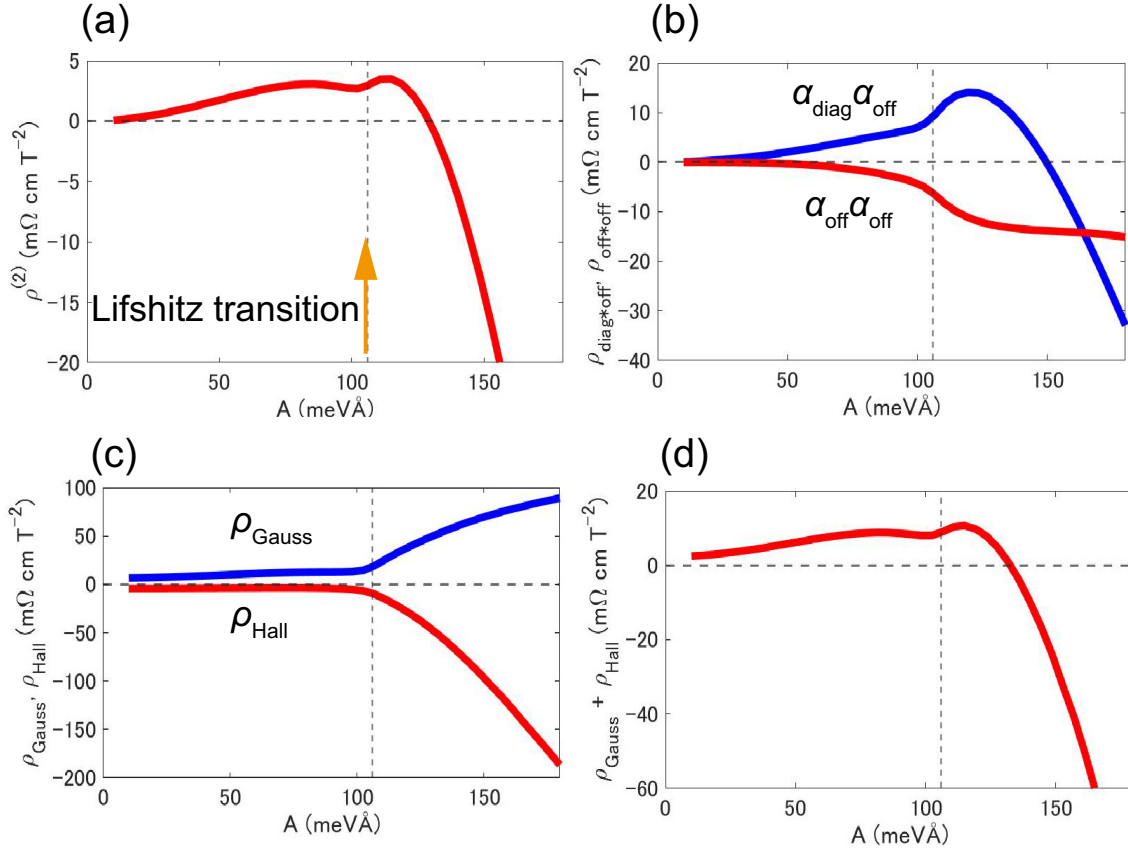


Figure 5.4: A -dependence of the second coefficients (a) $\rho^{(2)}$ (b) $\alpha_{ii}\alpha_{jk}$ and $\alpha_{ij}\alpha_{kl}$ (c) ρ_{Gauss} and ρ_{Hall} (d) $\rho_{\text{Gauss}} + \rho_{\text{Hall}}$

negative around the singularity, and the Fermi surface gets closer to the points. Hence, the negative off-diagonal mass mainly contributes to the electron conduction at low temperature resulting in the sign inversion in the LMR. On the other hand, the $\alpha_{ij}\alpha_{jk}v_iv_k$ component has a smaller value all around the space and the negative region is well localized near the Weyl point even when A is large. This is the reason the $\alpha_{ii}\alpha_{jk}v_jv_k$ component determines the sign of LMR. We also mapped $\alpha_{jk}v_jv_k/|v_j||v_k|$ and α_{ii} in Fig. 5.6a-f. The off-diagonal term is singular and negative (Fig. 5.6c) while the diagonal term is positive (Fig. 5.6f) with large A . Hence, we can attribute the negative LMR to the negative off-diagonal component in inverse mass tensor.

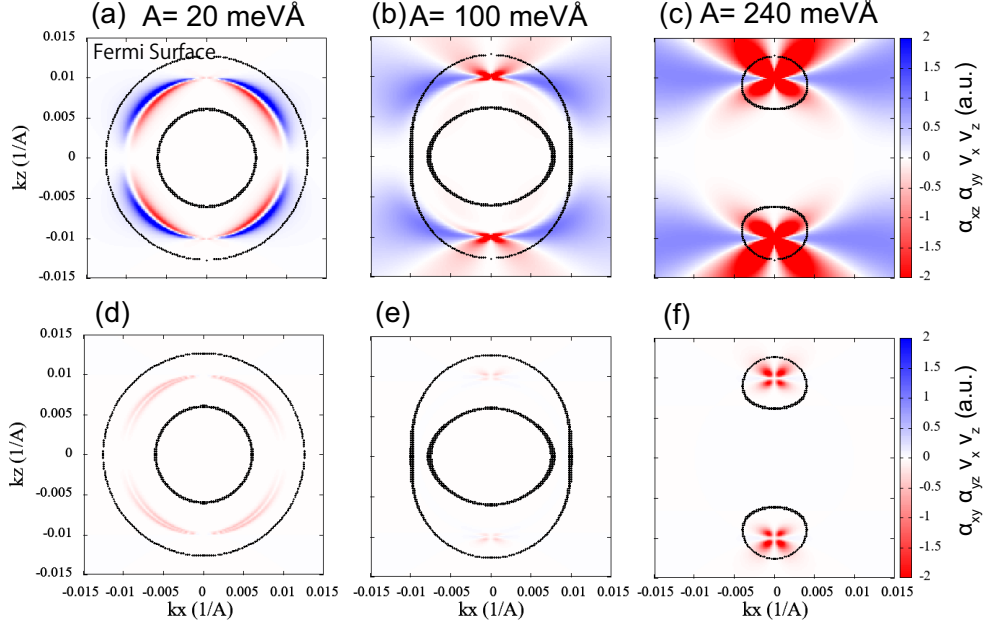


Figure 5.5: (a-c) Maps of $\alpha_{xz}\alpha_{yy}v_xv_z$ in $k_y = 0 \text{ \AA}^{-1}$ plane and (d-f) maps of $\alpha_{xy}\alpha_{yz}v_xv_z$ in $k_y = 0.001 \text{ \AA}^{-1}$ plane.

The negative off-diagonal component and positive diagonal component maximally enhances the Hall conductivity, which negatively contributes to the TMR (Eq. 5.13) and determines the sign. On the other hand, the term from the Gaussian curvature (Eq. 5.12) is positive because the curvature is dominantly positive in the vicinity of the Fermi surface with any values of A (Fig. 5.7).

In summary, the negative MR can arise from the negative singularity of off-diagonal effective mass in the Brillouin zone in the semiclassical viewpoint. When the singularity is close to the Fermi surface, the anomalous behavior is enhanced and observable at low temperatures. We want to note that the sign of LMR and TMR is determined independently in principle. The model of Weyl semimetal we used this time indicates negative and singular values of off-diagonal inverse mass and positive diagonal mass, which yields the negative LMR and negative TMR simultaneously.

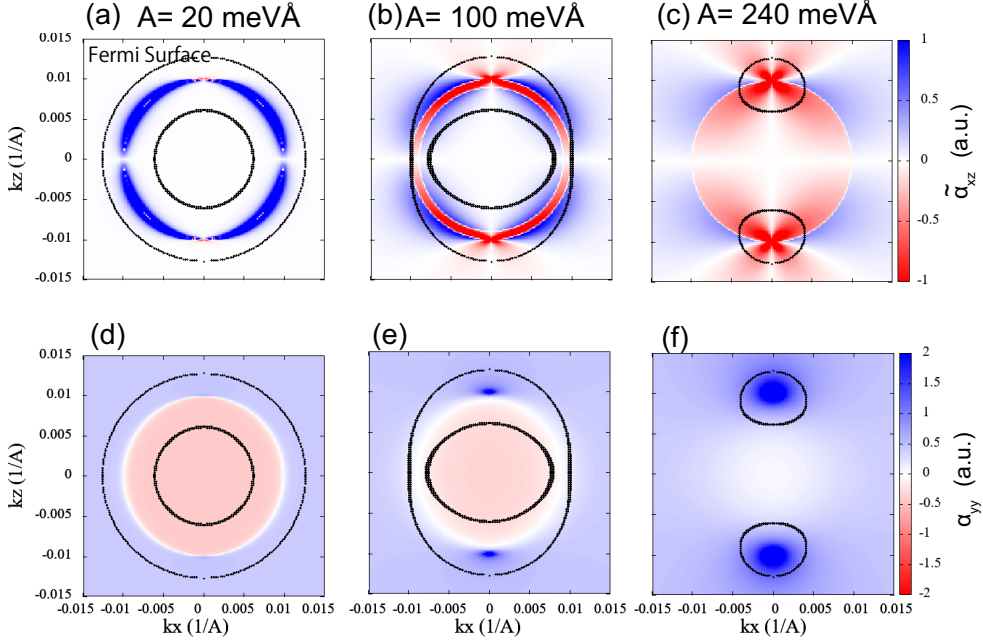


Figure 5.6: Maps of off-diagonal (upper panel) and diagonal (lower panel) element of inverse effective mass tensor in $k_y = 0 \text{ \AA}^{-1}$ plane. $\tilde{\alpha}_{xz} = \alpha_{xz}v_xv_z/|v_x||v_z|$

5.3 Planar Hall effect

We demonstrate the planar Hall effect (PHE) in the Weyl electron system. The parameters and the condition of calculation are the same as the MR calculations. The magnetic field was rotated in x - y plane $(B_x, B_y, B_z) = (B \cos \theta, B \sin \theta, 0)$ and PHE was calculated by $\rho_{xy} = [\hat{\sigma}^{-1}]_{xy}$. The results with several A parameters are shown in Fig. 5.8. The functional form is a sine curve with the period π . The sign of PHE with small A is consistent with the expectation of conventional multi-carrier models (Sec. 4.4.1). When the parameter is increased, the sign is inverted (Fig. 5.8, $A = 240 \text{ meV\AA}$). This inversion cannot be explained by a simple model which approximate the Fermi surface with multiple sphere or ellipsoids (Appendix A). We further calculated A -dependence of the $\Delta\rho_{\text{diff}} = \rho_{xy}|_{\theta=3\pi/4} - \rho_{xy}|_{\theta=\pi/4}$ (Fig. 5.9a). The monotonic increment of the amplitude before the Lifshitz transition and drastic drop after the point. We can also see that the amplitude monotonically increases

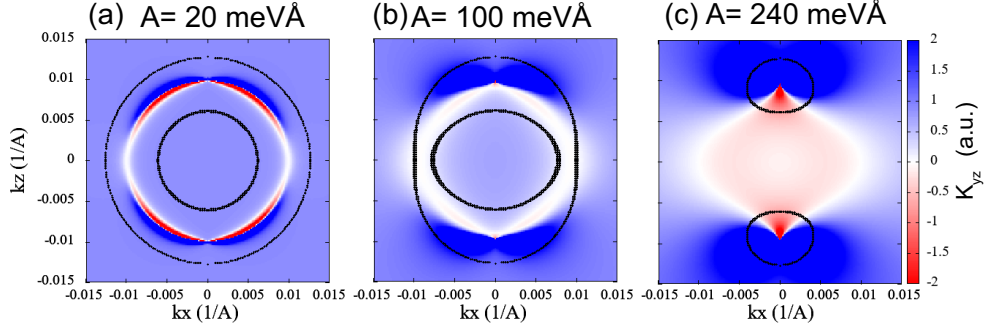


Figure 5.7: Maps of the Gaussian curvature: $K_{yz} = \alpha_{yy}\alpha_{zz} - \alpha_{yz}^2$ in $k_y = 0 \text{ \AA}^{-1}$ plane.

with increasing the field and the field value is rarely relevant to the sign of $\Delta\rho_{\text{diff}}$. $\Delta\rho_{\text{diff}}$ is given by the difference of TMR and LMR due to the isotropy in the x - y plane (*Appendix B*). Hence, the sign inversion is corresponding to the sign inversion in the LMR and TMR. The drastic drop after the Lifshitz transition is due to the large difference between TMR and LMR (Fig. 5.9b), and the sign of PHE is changed depending on the order of TMR and LMR. Note that the sign of PHE is not always corresponding to the sign of MR [63].

5.3.1 Temperature dependence of PHE

Finally, we demonstrate the temperature dependence of MR and PHE amplitude. While the Fermi energy deviates from the Weyl point ($E = 0$), it is expected that the thermal carrier can reflect the singular characteristics at the Weyl point. It possibly appears in the temperature dependence of MR or PHE. The parameter set is the same as the former MR calculation and the transport lifetime of electron τ is assumed to be constant. The A parameter was varied from 60 meVÅ to 140 meVÅ.

The temperature dependence of PHE amplitude is shown in Fig. 5.10a. The amplitude was calculated by the difference of TMR and LMR as mentioned before. It indicates anomalies in two specific temperatures: a dip or sign inversion around $k_B T = E_F/2$ and a peak around $k_B T = E_F$. The positions of these structures are irrelevant to the parameter A . The dip structure is especially correlated to the

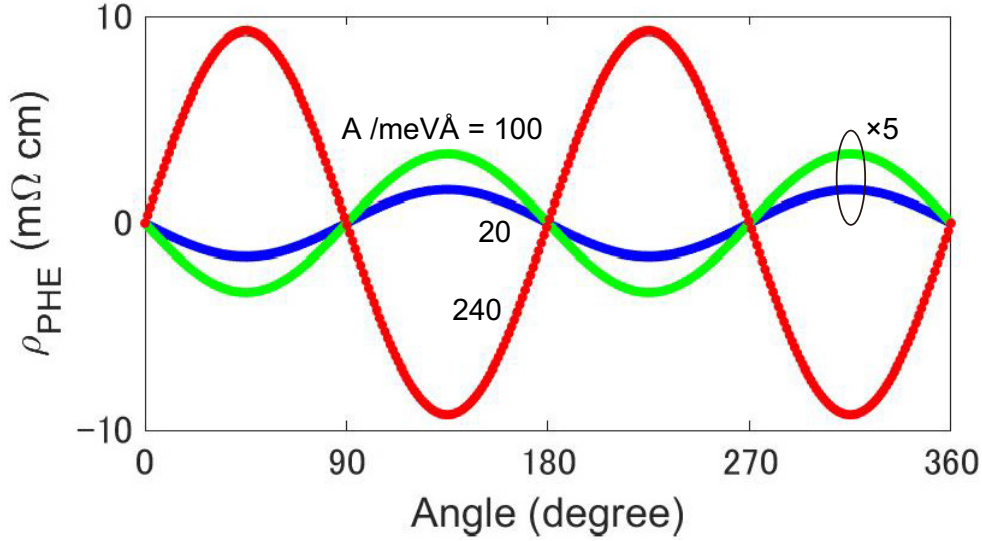


Figure 5.8: Angular dependence of PHE in Weyl electron with different A parameters.

energy of the Weyl points. Considering the case $A = 100 \text{ meV\AA}$, the off-diagonal value of $\hat{\alpha}$ is relatively small on the Fermi surfaces while the singularity is located at the Weyl points (Fig. 5.6b). When $k_B T = E_F/2$, the tail of the Fermi distribution function reaches the Weyl points as shown in Fig. 5.11. At this temperature, the carriers in the vicinity of the Weyl points contribute negatively to the TMR and LMR. This is the mechanism that the dips in temperature dependence appear. On the other hand, when A is such large that the effect of singular effective mass is remarkable on the Fermi surface, the sign changes at low temperature. In this case, the dip structure does not appear because the main contribution is from the vicinity of Fermi energy, and carriers from upper energy have a positive contribution to MR at high temperatures. The results imply that the dip or peak position gives information about how the Fermi energy is distant from the singularities of the effective mass. Except for the quantum effect including the Kondo effect [135] or electron localization [136], the electron lifetime monotonically decreases as temperature grows. Hence, we can expect the non-monotonic dependence even when the real materials with temperature-dependent lifetime.

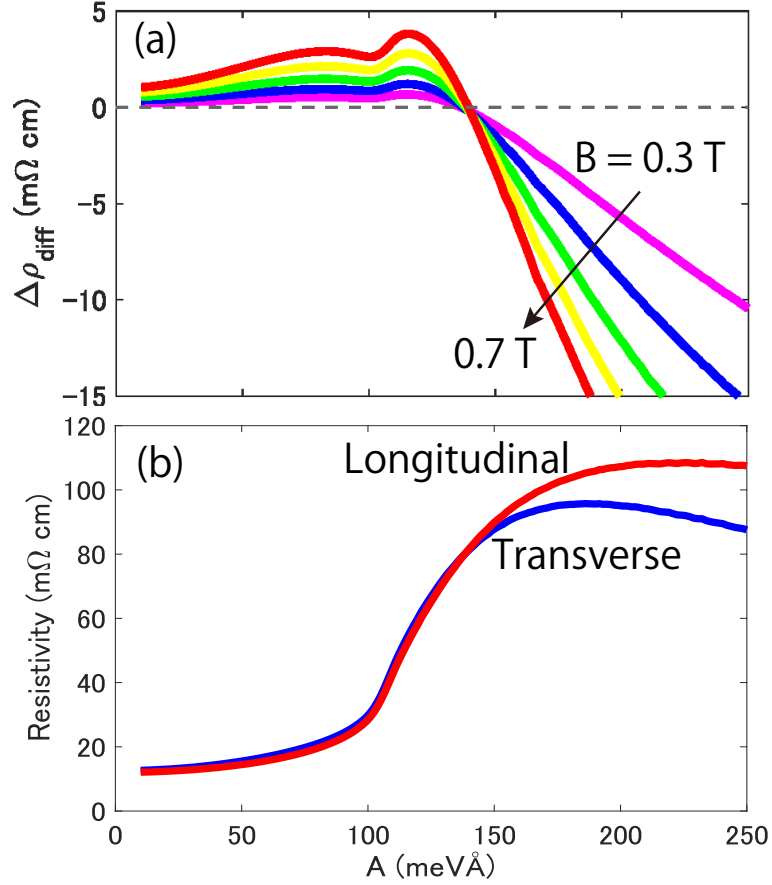


Figure 5.9: A -dependence of (a) $\Delta\rho_{\text{diff}}$ and (b) TMR, LMR. (a) also shows the field dependence.

The results in LMR and TMR are shown in Fig. 5.10b,c. Due to the large background, the effect of singular effective mass is not clear. There is a peak structure in the curve with small A , which is not a characteristic originating from the Weyl points because it appears when the system is equivalent to a normal semimetal. In the vicinity of $E = 0$ with small A , the electron and hole carrier coexist, and the carrier number varies with temperature. In semimetals, charge compensation in carriers yields large MR. Hence, the peak structure would appear when the numbers of each carrier are closest to the valance. With large A , the dependence is monotonic

decay and we cannot find any anomaly in it.

All the cases of PHE, TMR, and LMR converge at high temperatures because the electron and hole carriers in much higher and lower energy contribute to conduction. The effect of Weyl points is hidden in these carriers and the system becomes identical to an ordinal semimetal.

In conclusion, we can present an application of PHE. As we saw, PHE amplitude reflects the singularity of effective mass more sensitively than MR and gives information about the energy of the points measured from the Fermi energy. By subtracting LMR from TMR, we can find the position of singularity through the non-monotonic temperature dependence.

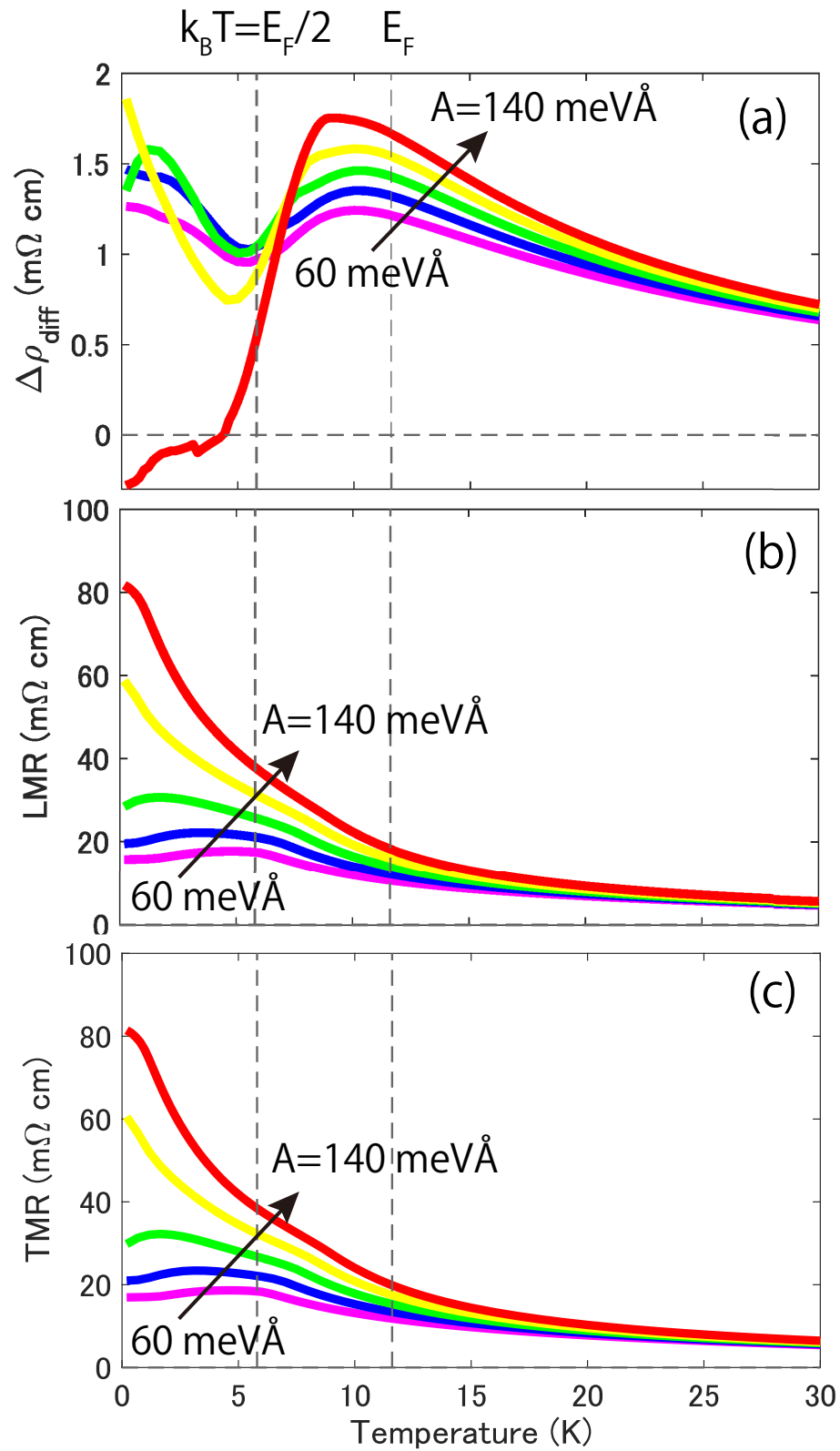


Figure 5.10: Temperature dependence of (a) $\Delta\rho_{\text{diff}}$, (b) LMR, and (c) TMR.

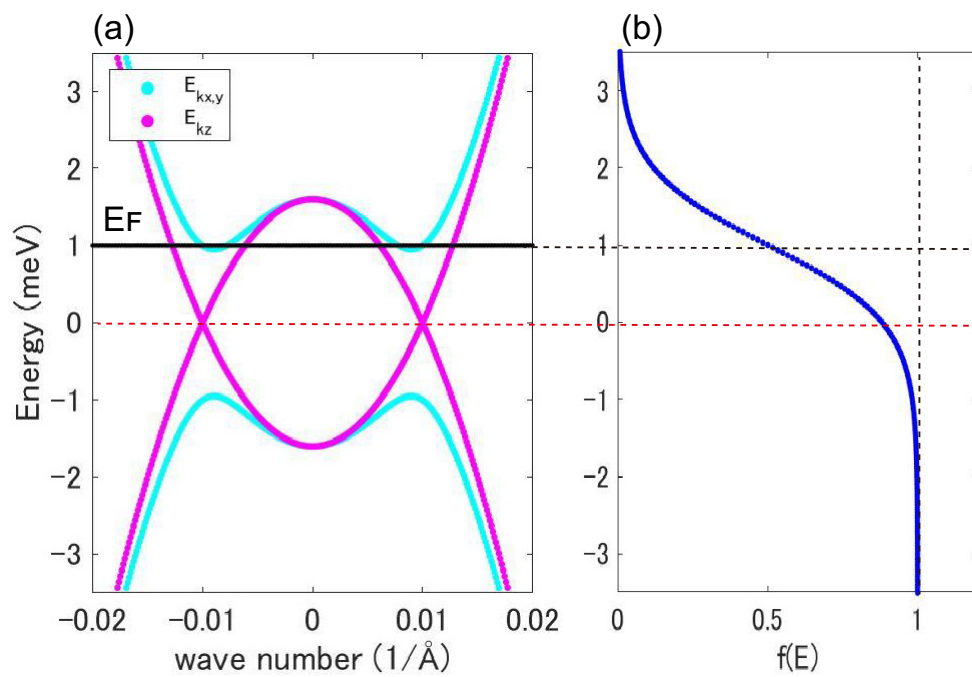


Figure 5.11: The energy dispersion and distribution function at $T = E_F/2$.

Chapter 6

Summary

We investigated the magneto-transport phenomena in Dirac and Weyl electron systems based on the semiclassical theory. In semimetals with Dirac electron, we found a monotonic increment of carrier concentration in the quantum limit. In the anisotropic case, this increment generally progresses in the direction perpendicular to the direction of the lowest mobility, which results in the suppression of anisotropy in transverse magnetoresistance. We have successfully explained the angular dependence of TMR in bismuth at high fields by combining the field-dependent carrier density and semiclassical transport theory. We have further fit the TMR at high fields exceeding 40 T by considering the carrier evacuation in electron pockets and linear field-dependence of scattering rate. We found that this time of field-dependent mobility is often observed in the materials which exhibit the linear MR. We also found that the field-dependence of mobility has strong anisotropy. While the origin of this field-dependence is still an open question, we guess that there would be a hint in the scattering process of other linear-MR materials.

Next, we calculated the MR and PHE in the Weyl electron system. We found a new mechanism of sign change in MR. The essence is the off-diagonal terms in the inverse effective mass tensor. The Weyl points, which are the divergence and convergence of Berry curvature, are also the singularities of effective mass. The Fermi surface near the Weyl points possesses a large and negative off-diagonal mass. By the Jones-Zener expansion of conductivity, we found the negative off-diagonal

inverse-effective mass is the direct origin of negative LMR. We also found that it enhances the Hall conductivity resulting in negative TMR.

We also discussed the PHE in multiple carrier, Dirac, and Weyl electron systems in the semiclassical framework. PHE naturally arises from the multiple carrier conduction and the amplitude saturates at high fields in metals and uncompensated semimetals. Furthermore, the saturated value is negatively correlated with the mobility. PHE observed in bismuth, which is a typical Dirac electron system, was successfully explained by considering the field-dependent carrier concentration. We found that the increased carrier density in Dirac electron suppresses the violation from charge compensation and causes the qualitative shift in angular dependence in real cases. We also found that the effect of mass-singularity in the Weyl electron clearly appears in the temperature dependence of PHE amplitude. The non-monotonic behaviors including dip and peak structures in the temperature dependence was pointed to correspond to the Fermi temperature. The PHE amplitude may be useful to identify the energy of the Weyl points measured from the Fermi energy.

Appendix A

PHE with spherical and ellipsoidal Fermi surfaces

A.1 PHE in isotropic two-carrier metals

To evaluate the PHE in multiple carrier systems, we calculated the total conductivity tensor $\hat{\sigma}$ by summing up all the conductivity tensors $\hat{\sigma}^{(i)}$ of each carrier (Eq. 2.19). Each conductivity tensor in an isotropic carrier is given in the following form:

$$\begin{aligned}\hat{\sigma}^{(i)} &= (\mu_i^{-1}\hat{1} \pm \hat{B})^{-1} \\ &= \frac{en\mu_i}{(\mu_i B)^2 + 1} \begin{bmatrix} (\mu_i B_x)^2 + 1 & \mu_i^2 B_x B_y & \mp \mu_i B_y \\ \mu_i^2 B_x B_y & (\mu_i B_y)^2 + 1 & \pm \mu_i B_x \\ \pm \mu_i B_y & \mp \mu_i B_x & 1 \end{bmatrix}, \quad (\text{A.1}) \\ \mu_i &= e\tau_i/m_i^*.\end{aligned}$$

The sign \pm is corresponding to the sign of carrier charge. m^* and τ represent the mass and lifetime of carriers respectively. The magnetic field is fixed in the x - y plane. The magnetoresistivity tensor is calculated by summing up all the conductivity tensors and taking inversion. In the isotropic 2-electron system with different mobilities (μ_1 ,

μ_2) and the same density n , TMR and LMR are given as follows:

$$\begin{aligned}\rho_{\text{TMR}} &= \frac{1}{en} \frac{(\mu_1 + \mu_2)(\mu_1\mu_2 B^2 + 1)}{4(\mu_1\mu_2 B)^2 + (\mu_1 + \mu_2)^2} \\ \rho_{\text{LMR}} &= \frac{1}{en(\mu_1 + \mu_2)}.\end{aligned}$$

The PHE amplitude is given by these difference ($\Delta\rho_{\text{diff}} = \rho_{\text{TMR}} - \rho_{\text{LMR}}$) and it saturates at high fields to be $\frac{1}{en} \frac{(1-r)^2}{4\mu_2(1+r)}$ ($r = \mu_2/\mu_1$).

A.2 Multiple ellipsoidal Fermi surfaces

We consider the cases with anisotropic multiple carriers. The simplest case: two anisotropic ellipsoidal Fermi surfaces whose axes are fixed to x, y, z direction, can be realized by replacing the isotropic mobility tensor $\mu_i \hat{1}$ in the Eq. A.1 with anisotropic ones: $\hat{\mu} = \text{diag}\{\mu_1, \mu_2, \mu_3\}$, $\hat{\nu} = \text{diag}\{\nu_1, \nu_2, \nu_3\}$. The amplitude of PHE with the field rotating in the x - y plane is

$$\Delta\rho_{\text{diff}} = \frac{1}{en} \frac{(\mu_1 - \nu_1)(\mu_2 - \nu_2)\mu_3\nu_3 B^2}{4\mu_3\nu_3((\mu_1 - \nu_1)\mu_2\nu_2 \cos^2 \theta + (\mu_2 - \nu_2)\mu_1\nu_1 \sin^2 \theta)B^2 + (\mu_1 - \nu_1)(\mu_2 - \nu_2)(\mu_3 + \nu_3)}.$$

θ is the angle between the field and the x axis. This result indicates that the sign of PHE is determined by the in-plane (x, y) components of the mobility tensors. The sign is the same as isotropic metals and semimetals when all the components of one mobility tensor are greater than those of another carrier (Fig. A.1a,d). On the other hand, the sign is inverted in a moderately high field when the anisotropy of carriers is enough high and the directions of highest mobility in two carriers are distant by 90 degrees in the x, y plane as shown in Fig. A.1b,e. In the Weyl electron model with large A , the Fermi surfaces are seemingly twin ellipsoids (Fig. A.1c). Assuming a pair of parallel ellipsoids, which corresponds to the condition $(\mu_1, \mu_2, \mu_3) = (\nu_1, \nu_2, \nu_3)$, the angular dependence of PHE does not emerge ($\Delta\rho_{\text{diff}} = 0$). However, the finite value of PHE is estimated in the Weyl electron by fully considering the energy dispersion and local effective mass. This discrepancy implies that the ellipsoidal (parabolic) model

is not always a good approximation even when the Fermi surfaces are apparently ellipsoids.

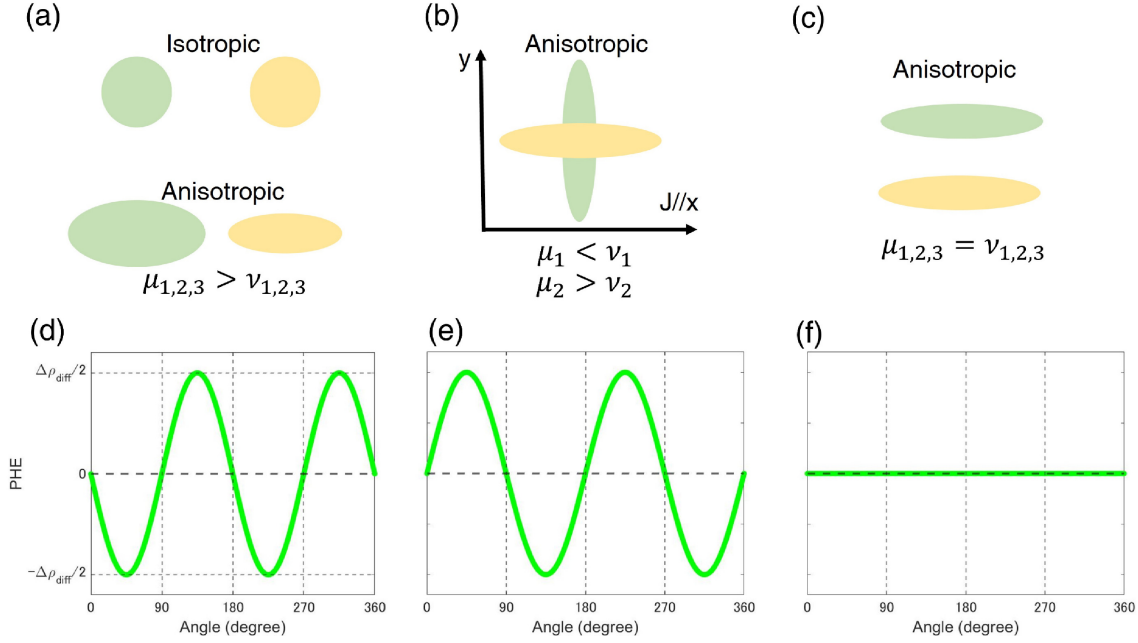


Figure A.1: Schematic images of (a) isotropic and anisotropic multi-surfaces, one of whose mobility is greater than the other, (b) anisotropic surfaces whose directions of highest mobility is distant by 90 degree in the Hall bar, and (c) equivalent two ellipsoids. (d-f) Angular dependence of PHE in (a-c) cases.

A.3 n -valley systems

In the case of isotropic n -carrier system, the conductivity tensor with rotating field is given by summing n -conductivity tensors as $\hat{\sigma} = \sum_{i=1}^n (\mu_i \hat{\mathbf{1}} - \hat{B})^{-1}$. The resistivity

tensor is given by the inversion. The result is shown below.

$$\hat{\rho} = \begin{bmatrix} \frac{(-S_1 S_3 + S_2^2)(\cos(\theta))^2 + S_1(S_1 + S_3)}{(S_1^2 + S_2^2)(S_1 + S_3)} & \frac{(-S_1 S_3 + S_2^2) \cos(\theta) \sin(\theta)}{(S_1^2 + S_2^2)(S_1 + S_3)} & -\frac{S_2 \sin(\theta)}{S_1^2 + S_2^2} \\ \frac{(-S_1 S_3 + S_2^2) \cos(\theta) \sin(\theta)}{(S_1^2 + S_2^2)(S_1 + S_3)} & \frac{(S_1 S_3 - S_2^2)(\cos(\theta))^2 + S_1^2 + S_2^2}{(S_1^2 + S_2^2)(S_1 + S_3)} & \frac{S_2 \cos(\theta)}{S_1^2 + S_2^2} \\ \frac{S_2 \sin(\theta)}{S_1^2 + S_2^2} & -\frac{S_2 \cos(\theta)}{S_1^2 + S_2^2} & \frac{S_1}{S_1^2 + S_2^2} \end{bmatrix},$$

and PHE and AMR are given as follows:

$$\rho_{\text{PHE}} = \frac{1}{en} \frac{(-S_1 S_3 + S_2^2) \cos \theta \sin \theta}{(S_1^2 + S_2^2)(S_1 + S_3)}, \quad (\text{A.2})$$

$$\rho_{\text{AMR}} = \frac{1}{en} \frac{(-S_1 S_3 + S_2^2) \cos^2 \theta + S_1(S_1 + S_3)}{(S_1^2 + S_2^2)(S_1 + S_3)}, \quad (\text{A.3})$$

$$S_1 = \sum_{i=1}^n \frac{\mu_i}{(\mu_i B)^2 + 1},$$

$$S_2 = \sum_{i=1}^n \frac{\mu_i^2 B}{(\mu_i B)^2 + 1},$$

$$S_3 = \sum_{i=1}^n \frac{\mu_i^3 B^2}{(\mu_i B)^2 + 1}.$$

This result shows the $\sin \theta \cos \theta$ characteristic in PHE and $\cos^2 \theta$ in AMR hold in the isotropic multi-carrier system regardless of the number of carriers. Moreover, these characteristics remain unless the mobility in all the carriers are equal. This statement is proved as follows:

$$\begin{aligned} S_1 \cdot S_3 - S_2^2 &= \left(\sum_{i=1}^n \frac{\mu_i}{(\mu_i B)^2 + 1} \right) \cdot \left(\sum_{i=1}^n \frac{\mu_i^3 B^2}{(\mu_i B)^2 + 1} \right) - \left(\sum_{i=1}^n \frac{\mu_i^2 B}{(\mu_i B)^2 + 1} \right)^2 \\ &= \sum_{i \neq j}^n \frac{\mu_i \mu_j^3 B^2}{((\mu_i B)^2 + 1)((\mu_j B)^2 + 1)} - 2 \sum_{i > j}^n \frac{\mu_i^2 \mu_j^2 B^2}{((\mu_i B)^2 + 1)((\mu_j B)^2 + 1)} \\ &= \sum_{i \neq j}^n \frac{\mu_i \mu_j (\mu_i - \mu_j)^2 B^2}{((\mu_i B)^2 + 1)((\mu_j B)^2 + 1)}. \end{aligned}$$

$\therefore S_1 \cdot S_3 - S_2^2 = 0 \Leftrightarrow$ More than one electrons have different mobility.

In isotropic $2n$ -valley semimetals with n -hole and n -electron system, PHE and AMR are given by the same way, and the results are

$$\rho_{\text{PHE}} = -\frac{1}{en} \frac{((A_3 + B_3)(A_1 + B_1) - (A_2 - B_2)^2) \cos \theta \sin \theta}{(A_1 + A_3 + B_1 + B_3) ((A_1 + B_1)^2 + (A_2 - B_2)^2)}, \quad (\text{A.4})$$

$$\begin{aligned} \rho_{\text{AMR}} &= \frac{1}{en} \frac{-(A_3 + B_3)(A_1 + B_1) + (A_2 - B_2)^2}{((A_1 + B_1)^2 + (A_2 - B_2)^2) (A_1 + A_3 + B_1 + B_3)} \cos^2 \theta \\ &+ \frac{1}{en} \frac{A_1 + B_1}{(A_1 + B_1)^2 + (A_2 - B_2)^2}, \end{aligned} \quad (\text{A.5})$$

where

$$\begin{aligned} A_1 &= \sum_{i=1}^n \frac{\mu_{ei}}{(\mu_{ei}B)^2 + 1}, & B_1 &= \sum_{i=1}^n \frac{\mu_{hi}}{(\mu_{hi}B)^2 + 1}, \\ A_2 &= \sum_{i=1}^n \frac{\mu_{ei}^2 B}{(\mu_{ei}B)^2 + 1}, & B_2 &= \sum_{i=1}^n \frac{\mu_{hi}^2 B}{(\mu_{hi}B)^2 + 1}, \\ A_3 &= \sum_{i=1}^n \frac{\mu_{ei}^3 B^2}{(\mu_{ei}B)^2 + 1}, & B_3 &= \sum_{i=1}^n \frac{\mu_{hi}^3 B^2}{(\mu_{hi}B)^2 + 1}. \end{aligned}$$

The amplitude does not vanish even when all the values of carrier mobility are equal.

Appendix B

PHE in a system isotropic in x - y plane

With the help of the Seitz equation [53, 137], we can see that the amplitude of PHE and AMR are equivalent when the system is isotropic in the plane of rotating magnetic field. The $I-V$ relation in a weak magnetic field is written in the following form:

$$\mathbf{E} = \rho_0 \mathbf{j} + \rho_0^{-1} \left[\alpha \mathbf{j} \times \mathbf{B} + \beta B^2 \mathbf{j} + \gamma (\mathbf{B} \cdot \mathbf{j}) \mathbf{B} + \delta \hat{T} \mathbf{j} \right], \quad (\text{B.1})$$

where α, β, γ are the model parameters. The tensor \hat{T} describes the anisotropy of crystals. This time, we fixed the field in the x, y plane, where the Fermi surfaces are isotropic. This configuration can be written in the two conditions: $\mathbf{B} = (B \cos \phi, B \sin \phi, 0)$ and $\hat{T} = \text{diag}\{0, 0, B_z^2\}$. The straightforward calculation leads to the angular dependence of PHE ($\rho_{xy} = E_x/j_y$) and AMR ($\rho_{xx} = E_x/j_x$) as shown below.

$$\rho_{\text{PHE}} = \frac{\gamma B^2}{\rho_0} \sin \phi \cos \phi \quad (\text{B.2})$$

$$\rho_{\text{AMR}} = \rho_0 + \frac{\beta B^2}{\rho_0} + \frac{\gamma B^2}{\rho_0} \cos^2 \theta \quad (\text{B.3})$$

If we rewrite $\rho_{\parallel} \equiv \rho_0 + \frac{\beta B^2}{\rho_0} + \frac{\gamma B^2}{\rho_0}$, $\rho_{\perp} \equiv \rho_0 + \frac{\beta B^2}{\rho_0}$, we obtain

$$\rho_{\text{PHE}} = -(\rho_{\perp} - \rho_{\parallel}) \sin \phi \cos \phi, \quad (\text{B.4})$$

$$\rho_{\text{AMR}} = \rho_{\perp} - (\rho_{\perp} - \rho_{\parallel}) \cos^2 \theta. \quad (\text{B.5})$$

Hence, we can say that the amplitudes of both PHE and AMR are equivalent to the difference of transverse and longitudinal magnetoresistance when the system is isotropic in the plane of the rotating field.

Acknowledgements

I would like to acknowledge all the people who contributed to this thesis and who supported me throughout my Ph.D. course.

First, I would like to express my sincere gratitude to Prof. Yuki Fuseya for continuous supervising and valuable discussion. It was a fortune that I was greatly welcomed to the laboratory in spite of a sudden visit and participation. My life in this laboratory was fulfilled because the days were plenty of ideas and discussions.

I would like to express my special appreciation to Prof. Takahiro Muranaka, Prof. Yasushi Ohfuti, Prof. Kazuyuki Matsubayashi, and Prof. Masashi Tokunaga in the University of Tokyo for taking time for the judge of this thesis out of the busy schedule.

My research works are also supported by collaborators from other laboratories. I would like to thank Prof. Masashi Tokunaga, Asst. Prof. Yuto Kihoshita in the University of Tokyo, Prof. Yasutaka Imanaka, and Senior Researcher Kanji Takehana in National Institute for Materials Science, for providing experimental data and taking time to discuss the magneto-optical spectra in bismuth.

I would like to thank Prof. Kamran Behnia in Centre national de la recherche Scientifique, Prof. Benoît Fauqué in Jeunes équipes de l'Institut de physique du Collège de France, and Prof. Zengwei Zhu in Huazhong University of Science and Technology for providing experimental data and giving me valuable comments about the preprint of our letters.

I would like to thank Prof. Ryotaro Arita, Dr. Hitoshi Mori in RIKEN, Prof. Shintaro Ishiwata, Assis. Prof. Hidefumi Takahashi, and Mr. Alex Hiro Mayo in Osaka University for providing data and giving me a chance to discuss the strange MR in newly synthesized material.

I would also like to express my gratitude to my former supervisor, Prof. Masashi Shiraishi, in Kyoto University. I am grateful for giving me a chance to know interesting theoretical research in the University of Electro-Communications. I had disturbed him and his laboratory due to my selfish behavior in past years. I would like to apologize for it and thank for his generosity.

I would also like to thank all the colleagues in the laboratory. Dr. Hiroshi Hayasaka, Dr. Yuki Izaki, Mr. Shogo Kawamura, Mr. Yuya Asaka and Mr. Yudai Awashima gave me impressive discussions. I deeply appreciate Mr. Awashima for his technical support. I spent a year with Mr. Naoto Kano, Mr. Tatsuki Kikuchi, and Mr. Yuki Mitani to learn quantum field theory from a textbook by *A. A. Abrikosov, L. P. Gorkov, I. E. Dzyaloshinski*. I also spent a good time with the members of the mountain hiking club: Mr. Yudai Awashima and Mr. Takeshi Kawasaki.

I would like to express my deep appreciation to the University of Electro-Communications for successive financial support in the emergency due to COVID19.

Finally and most importantly, I would like to thank my parents for their support and encouragement for my education and research.

Bibliography

- [1] P. Kapitza, E. Rutherford. Proc. Math. Phys. Eng. Sci., **119**, 358–443, (1928).
- [2] L. Shubnikov, W. J. de Haas. Comm. Phys. Lab. Leiden, **207d**, (1930).
- [3] K. Kajita *et al.* Solid State Commun., **70**, 1189–1193, (1989).
- [4] K. Yamaji. J. Phys. Soc. Jpn., **58**, 1520–1523, (1989).
- [5] R. Yagi *et al.* J. Phys. Soc. Jpn., **59**, 3069–3072, (1990).
- [6] D.-X. Qu *et al.* Science, **329**, 821–824, (2010).
- [7] T. Liang *et al.* Nat. Mater., **14**, 280–284, (2015).
- [8] A. A. Taskin *et al.* Nat. Commun., **8**, 1340, (2017).
- [9] N. Doiron-Leyraud *et al.* Nature, **447**, 565–568, (2007).
- [10] A. Audouard *et al.* Phys. Rev. Lett., **103**, 157003, (2009).
- [11] A. Schuhl, F. N. Van Dau, J. R. Childress. Appl. Phys. Lett., **66**, 2751–2753, (1995).
- [12] H. X. Tang *et al.* Phys. Rev. Lett., **90**, 107201, (2003).
- [13] A. Abrikosov. Dover Publications, (2017).
- [14] M. N. Ali *et al.* Nature, **514**, 205–208, (2014).
- [15] Y. Fuseya, M. Ogata, H. Fukuyama. J. Phys. Soc. Jpn., **84**, 012001, (2015).

-
- [16] N. P. Armitage, E. J. Mele, A. Vishwanath. *Rev. Mod. Phys.*, **90**, 015001, (2018).
- [17] H. Nielsen, M. Ninomiya. *Physics Letters B*, **130**, 389 – 396, (1983).
- [18] D. T. Son, B. Z. Spivak. *Phys. Rev. B*, **88**, 104412, (2013).
- [19] A. A. Burkov. Chiral anomaly and diffusive magnetotransport in weyl metals. *Phys. Rev. Lett.*, **113**, 247203, (2014).
- [20] A. A. Burkov. *Phys. Rev. B*, **91**, 245157, (2015).
- [21] S. Nandy *et al.* *Phys. Rev. Lett.*, **119**, 176804, (2017).
- [22] A. A. Burkov. *Phys. Rev. B*, **96**, 041110, (2017).
- [23] X. Dai, Z. Z. Du, H.-Z. Lu. *Phys. Rev. Lett.*, **119**, 166601, (2017).
- [24] M. V. Berry. *Proc. R. Soc. Lond., Ser. A, Math. phys. sci*, **392**, 45–57, (1984).
- [25] T. Ando, T. Nakanishi, R. Saito. *J. Phys. Soc. Jpn.*, **67**, 2857–2862, (1998).
- [26] X. Huang *et al.* *Phys. Rev. X*, **5**, 031023, (2015).
- [27] Q. Li *et al.* *Nat. Phys.*, **12**, 550–554, (2016).
- [28] S. Liang *et al.* *Phys. Rev. X*, **8**, 1–13, (2018).
- [29] A. Vashist, R. K. Gopal, Y. Singh. *Sci. Rep.*, **11**, 8756, (2021).
- [30] N. Kumar *et al.* *Phys. Rev. B*, **98**, 041103, (2018).
- [31] M. Wu *et al.* *Phys. Rev. B*, **98**, 161110, (2018).
- [32] H. Li *et al.* *Phys. Rev. B*, **97**, 201110, (2018).
- [33] P. Li *et al.* *Phys. Rev. B*, **98**, 121108, (2018).
- [34] P. Li *et al.* *Phys. Rev. B*, **100**, 1–7, (2019).

-
- [35] S.-Y. Yang, K. Chang, S. S. P. Parkin. *Phys. Rev. Research*, **2**, 12–16, (2020).
- [36] Z. Li *et al.* *J. Appl. Phys.*, **127**, (2020).
- [37] D. D. Liang *et al.* *AIP Advances*, **9**, 0–6, (2019).
- [38] Q. Liu *et al.* *Phys. Rev. B*, **99**, 1–7, (2019).
- [39] J. Meng *et al.* *J. Phys.: Condens. Matter*, **32**, (2020).
- [40] Z. Zhu *et al.* *Nat. Commun.*, **8**, 15297, (2017).
- [41] Q. Chen *et al.* *Phys. Rev. B*, **104**, 115104, (2021).
- [42] D. Hirai *et al.* *J. Phys. Soc. Jpn.*, **90**, 094708, (2021).
- [43] P. Li *et al.* *Phys. Rev. B*, **98**, 121108, (2018).
- [44] A. Collaudin *et al.* *Phys. Rev. X*, **5**, 021022, (2015).
- [45] Z. Zhu *et al.* *J. Phys.: Condens. Matter*, **30**, 313001, (2018).
- [46] J. Xu *et al.* *Nat. Commun.*, **10**, 2875, (2019).
- [47] R. S. Allgaier, W. W. Scanlon. *Phys. Rev.*, **111**, 1029–1037, (1958).
- [48] J. O. Strom-Olsen, A. B. Pippard. *Proc. Roy. Soc., A*, **302**, 83–98, (1967).
- [49] B. Lüthi. *Phys. Rev. Lett.*, **2**, 503–504, (1959).
- [50] A. A. Abrikosov. *Sov. Phys. JETP*, **29**, 746–753, (1969).
- [51] A. A. Abrikosov. *Phys. Rev. B*, **58**, 2788–2794, (1998).
- [52] M. M. Parish, P. B. Littlewood. *Nature*, **426**, 162–165, (2003).
- [53] A. Pippard. *Cambridge Studies in Low Temperature Physics*. Cambridge University Press, (1989).
- [54] Z. Zhu *et al.* *Phys. Rev. B*, **84**, 115137, (2011).

-
- [55] Y. Zhao *et al.* Phys. Rev. X, **5**, 031037, (2015).
- [56] M. H. Cohen, E. I. Blount. Phil. Mag., **5**, 115, (1960).
- [57] P. A. Wolff. J. Phys. Chem. Solids, **25**, 1057, (1964).
- [58] S. Zhang *et al.* Phys. Rev. B, **99**, 035142, (2019).
- [59] M. Grundmann. Graduate Texts in Physics. Springer Berlin Heidelberg, (2010).
- [60] K. Akiba *et al.* Phys. Rev. B, **98**, 115144, (2018).
- [61] A. Pippard. Cambridge Studies in Low Temperature Physics. Cambridge University Press, (1989).
- [62] Y. Mitani, Y. Fuseya. J. Phys.: Condens. Matter, **32**, 345802, (2020).
- [63] Y. Awashima, Y. Fuseya. J. Phys.: Condens. Matter, **31**, 29LT01, (2019).
- [64] C. Collignon *et al.* Phys. Rev. Materials, **5**, 065002, (2021).
- [65] R. G. Chambers, N. F. Mott. Proc. R. Soc. Lond., Ser. A, Math. phys. sci., **238**, 344–357, (1957).
- [66] W. Shockley. Phys. Rev., **79**, 191–192, (1950).
- [67] M. Novak *et al.* Phys. Rev. B, **100**, 085137, (2019).
- [68] Y. Zhou *et al.* Phys. Rev. B, **102**, 115145, (2020).
- [69] H. J. Mackey, J. R. Sybert. Phys. Rev., **180**, 678–681, (1969).
- [70] A. Beer. Solid State Physics Series. Academic Press, (1963).
- [71] E. H. Sondheimer, A. H. Wilson. Proc. R. Soc. Lond., Ser. A, Math. phys. sci., **190**, 435–455, (1947).
- [72] R. Kubo. J. Phys. Soc. Jpn., **12**, 570–586, (1957).

-
- [73] M. Owada, Y. Awashima, Y. Fuseya. *J. Phys.: Condens. Matter*, **30**, 445601, (2018).
- [74] P. A. M. Dirac, R. H. Fowler. *Proc. Math. Phys. Eng. Sci.*, **117**, 610–624, (1928).
- [75] H. Fukuyama, R. Kubo. *J. Phys. Soc. Jpn.*, **28**, 570–581, (1970).
- [76] Y. Fuseya, M. Ogata, H. Fukuyama. *Phys. Rev. Lett.*, **102**, 066601, (2009).
- [77] Y. Fuseya, M. Ogata, H. Fukuyama. *J. Phys. Soc. Jpn.*, **81**, 093704, (2012).
- [78] G. P. Mikitik, Y. V. Sharlai. *Phys. Rev. Lett.*, **82**, 2147–2150, (1999).
- [79] A. A. Burkov, M. D. Hook, L. Balents. *Phys. Rev. B*, **84**, 235126, (2011).
- [80] W. Shockley. *Phys. Rev.*, **78**, 173–174, (1950).
- [81] G. Dresselhaus, A. F. Kip, C. Kittel. *Phys. Rev.*, **98**, 368–384, (1955).
- [82] J. M. Luttinger, W. Kohn. *Phys. Rev.*, **97**, 869–883, (1955).
- [83] E. Kane. *J. Phys. Chem. Solids*, **1**, 82–99, (1956).
- [84] U. Rössler. *Solid State Commun.*, **49**, 943–947, (1984).
- [85] H. Zhang *et al.* *Nat. Phys.*, **5**, 438–442, (2009).
- [86] C.-X. Liu *et al.* *Phys. Rev. B*, **82**, 045122, (2010).
- [87] Z. Wang *et al.* *Phys. Rev. B*, **88**, 125427, (2013).
- [88] Y. Izaki, Y. Fuseya. *Phys. Rev. Lett.*, **123**, 156403, (2019).
- [89] M. Willatzen, L. C. L. Y. Voon. Springer Berlin Heidelberg, (2009).
- [90] Y. Yafet, pp. 1–98. Academic Press, (1963).
- [91] H. Kosaka *et al.* *Electronics Letters*, **37**, 464, (2001).

-
- [92] L. M. Roth. Phys. Rev., **118**, 1534–1540, (1960).
- [93] P. Löwdin. J. Chem. Phys., **19**, 1396–1401, (1951).
- [94] G. E. Smith, G. A. Baraff, J. M. Rowell. Phys. Rev., **135**, A1118, (1964).
- [95] V. S. Édel'man. Adv. Phys., **25**, 555, (1976).
- [96] K. Behnia, M.-A. Méasson, Y. Kopelevich. Phys. Rev. Lett., **98**, 166602, (2007).
- [97] Z. Zhu *et al.* Proc. Natl. Acad. Sci. U.S.A., **109**, 14813–14818, (2012).
- [98] Y. Fuseya *et al.* Phys. Rev. Lett., **115**, 216401, (2015).
- [99] C. L. Kane, E. J. Mele. Phys. Rev. Lett., **95**, 146802, (2005).
- [100] L. Onsager. Lond. Edinb. Dublin philos. mag. j. sci., **43**, 1006–1008, (1952).
- [101] J. Zak. Phys. Rev. Lett., **62**, 2747–2750, (1989).
- [102] K. S. Novoselov *et al.* Nature, **438**, 197–200, (2005).
- [103] A. A. Taskin, Y. Ando. Phys. Rev. B, **84**, 035301, (2011).
- [104] K. Shrestha *et al.* Phys. Rev. B, **90**, 241111, (2014).
- [105] S. I. Vedeneev. Physics-Uspekhi, **60**, 385–401, (2017).
- [106] L. M. Roth. Phys. Rev., **145**, 434–448, (1966).
- [107] C. M. Wang, H.-Z. Lu, S.-Q. Shen. Phys. Rev. Lett., **117**, 077201, (2016).
- [108] R. Okugawa, S. Murakami. Phys. Rev. B, **89**, 235315, (2014).
- [109] C. Lew Yan Voon, M. Willatzen. Springer, Berlin, Germany, (2009).
- [110] M. Faraday. Exp. Res. Ser. XX, **27**, (1845).
- [111] P. Currie. Ann. Chim. Phys., **5**, (1895).

-
- [112] A. V. Etingshausen, W. Nernst. *Annalen der Physik*, **265**, 343–347, (1886).
- [113] W. J. de Haas, P. M. van Alphen. *Comm. Phys. Lab. Leiden*, **212d**, (1930).
- [114] Z. Zhu *et al.* *Nat. Phys.*, **8**, 89–94, (2012).
- [115] R. Hartman. *Phys. Rev.*, **181**, 1070–1086, (1969).
- [116] M. P. Vecchi, J. R. Pereira, M. S. Dresselhaus. *Phys. Rev. B*, **14**, 298, (1976).
- [117] Y. Liu, R. E. Allen. *Phys. Rev. B*, **52**, 1566–1577, (1995).
- [118] G. A. Baraff. *Phys. Rev.*, **137**, A842, (1965).
- [119] A. Iwasa *et al.* *Sci. Rep.*, **9**, 1672, (2019).
- [120] C. Goldberg, R. E. Davis. *Phys. Rev.*, **94**, 1121–1125, (1954).
- [121] M. Shibuya. *Phys. Rev.*, **95**, 1385–1393, (1954).
- [122] K. Shogenji, S. Uchiyama. *J. Phys. Soc. Jpn.*, **12**, 1164–1164, (1957).
- [123] L. Grabner. *Phys. Rev.*, **117**, 689–697, (1960).
- [124] Y. Bason *et al.* *Phys. Rev. B*, **79**, 092406, (2009).
- [125] X. Huang *et al.* *Phys. Rev. X*, **5**, 031023, (2015).
- [126] D. L. Partin *et al.* *Phys. Rev. B*, **38**, 3818–3824, (1988).
- [127] M. Lu *et al.* *Phys. Rev. B*, **53**, 1609–1615, (1996).
- [128] A. H. Kahn. *Phys. Rev.*, **119**, 1189–1192, (1960).
- [129] G. D. Mahan. *J. Phys. F: Met. Phys.*, **13**, L257–L263, (1983).
- [130] I. Crassee *et al.* *Phys. Rev. Materials*, **2**, 120302, (2018).
- [131] H.-Z. Lu, S.-B. Zhang, S.-Q. Shen. *Phys. Rev. B*, **92**, 045203, (2015).
- [132] A. A. Burkov, L. Balents. *Phys. Rev. Lett.*, **107**, 127205, (2011).

- [133] T. D. Fuchser, H. J. Mackey, J. R. Sybert. *Phys. Rev. B*, **2**, 3863–3869, (1970).
- [134] H. Fukuyama. *Prog. Theor. Phys.*, **42**, 1284–1303, (1969).
- [135] J. Kondo. *Prog. Theor. Phys.*, **32**, 37–49, (1964).
- [136] S. Hikami, A. I. Larkin, Y. Nagaoka. *Prog. Theor. Phys.*, **63**, 707–710, (1980).
- [137] F. Seitz. *Phys. Rev.*, **79**, 372–375, (1950).

List of publication

Academic paper:

1. Akiyoshi Yamada and Yuki Fuseya. Angular dependence of magnetoresistance and planar Hall effect in semimetals in strong magnetic fields. *Physical Review B* 103, 12, pages 1-6 (2021). DOI:<https://doi.org/10.1103/PhysRevB.103.125148>